IMPROVING THE ELECTRO-CHEMO-MECHANICAL PROPERTIES OF $LI_XMN_2O_4$ CATHODE MATERIAL USING MULTISCALE MODELING

Improving the electro-chemo-mechanical properties of $Li_xMn_2O_4$ cathode material using Multiscale modeling

By Ramavtar Tyagi, MSc, B.Tech

A Thesis Submitted to the School of Graduate Studies in Partial Fulfilment of the Requirements for the Degree Doctor of Philosophy

McMaster University

PhD Thesis (2022)

Hamilton, Ontario (Mechanical Engineering)

TITLE: Improving the electro-chemo-mechanical properties of $Li_xMn_2O_4$ cathode material using Multiscale modeling

AUTHOR: Ramavtar Tyagi (McMaster University)

SUPERVISOR: Dr. Seshasai Srinivasan

NUMBER OF PAGES: xiv, 193

Abstract

Electrochemical Energy Storage Systems are a viable and popular solution to fulfill energy storage requirements for energy generated through sustainable energy resources. With the increasing demand for Electrical Vehicles (EVs), Lithium-ion batteries (LIB) are being widely and getting popular compared to other battery technologies due to their energy storage capacity. However, LIBs suffer from disadvantages such as battery life and the degradation of electrode material with time, that can be improved by understanding these mechanisms using experimental and computational techniques. Further, it has been experimentally observed and numerically determined that lithium-ion intercalation induced stress and thermal loading can cause capacity fading and local fractures in the electrode materials. These fractures are one of the major degradation mechanisms in Lithium-ion batteries.

With $Li_xMn_2O_4$ as a cathode material, stress values differ widely especially for intermediate State Of Charge (SOC), and very few attempts have been made to understand the stress distribution as a function of SOC at molecular level. Therefore, the estimates of mechanical properties such as Young's modulus, diffusion coefficient etc. differ, especially for partially charged states. Further, the effect of temperature, particularly elevated temperatures, have not been taken into the consideration. Studying these parameters at the atomic scale can provide insight information and help in improving these materials lifetime. Hence, molecular/atomic level mathematical modelling has been used to understand capacity fade due to Lithium-ion intercalation/de-intercalation induced stress. Large-scale Atomic/Molecular Massively Parallel Simulator (LAMMPS) [1], that

is widely used for atomic simulations, has been used for the simulation studies of this dissertation.

Thus, the objective of this study is to understand the fracture mechanisms in the Lithium Manganese Oxide ($LiMn_2O_4$) electrode at the molecular level by studying mechanical properties of the material at different SOC values using the principles of molecular dynamics (MD). As part of the model validation, the lattice parameter and volume changes of $Li_xMn_2O_4$ as a function of SOC ($0 < x < 1$) has been studied and validated with respect to the experimental data. This validated model has been used for a parametric study involving the SOC value, strain-rate (charge and discharge rate), and temperature. Based on the validated MD setup, doping and co-doping studies have been undertaken to design and develop new and novel cathode materials with enhanced properties. In the absence of experimental data for the new engineered structures, validation with Quantum Mechanics generated lattice structures has been done. The results suggest that lattice constant values obtained from both MD and QM simulations are in good agreement ($\sim 99\%$) with experimental values. Further, Single Particle Model (SPM) based macro scale Computational Fluid Dynamics findings show that co-doping has improved the material properties especially for Yttrium and Sulfur doped structures which can improve the cycle life anywhere between 600-7000 cycles. Further in order to reduce the required computational time to obtain minimum potential energy ionic configuration out of millions of scenario, Artificial Neural Network (ANN) technique is being used. It improved the processing time by more than 88%.

Acknowledgements

First, I would like to thank my supervisor Dr. Seshasai Srinivasan at McMaster, who provided me this opportunity to work on this research topic and for supporting me throughout. He is the best guide anyone can have, I have always felt that I was under the right guidance throughout my research. I would also like to thank my supervisory committee members Prof. Mohamed Abdelaziz Elbestawi and Dr. Amin Reza Rajabzadeh for their feedback. My thanks also to the Natural Sciences and Engineering Research Council of Canada (NSERC) Canada for funding this project. I would like to thank the Department of Mechanical Engineering and W Booth School of Engineering Practices and Technology for providing all the resources. I would like to thank Amirmasound Lanjan and Simran Sandhu for having fruitul conversations. I am forever grateful for the support and encouragement from my family and friends, with special thanks to my wife Apurva for her love, support, and staying up late on numerous occasions to give me company as I worked through the research challenges.

Contents

List of Figures

List of Tables

Chapter 1

Introduction

Energy is an important requirement for mankind. In recent years, there has been a lot of interest in developing new clean and renewable energy systems primarily due to concerns about human environmental footprint, such as Green House Gases (e.g. carbon dioxide etc.) and concerns with security and rapid global development. Significant development has been made in renewable energy technologies like solar, wind etc. However, the major disadvantages of these technologies is their inconsistency in energy generation. Therefore, it is necessary to develop state of the art energy storage devices that will help store the energy generated form these technologies. This brings in enormous amount of research interests in material developments for energy storage. Electrochemical energy storage devices such as Lithium-ion batteries, red-ox flow batteries, fuel cells, and electrochemical capacitors have been identified as the leading Electrical Energy Storage Systems (EESS) technologies as a result of their scalability and versatility. Fig. 1.1 [1, 2] shows the power and energy density features of electrochemical energy storage devices. This thesis will focus on

lithium-ion batteries that potentially have large energy densities which make them suitable for large scale energy storage applications like electrical grids and electric vehicles.

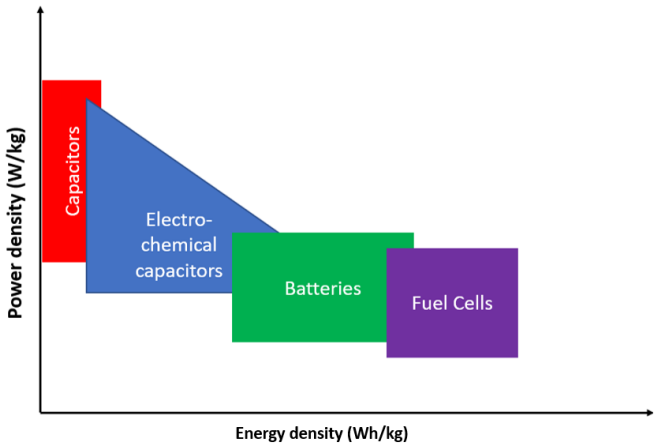

Figure 1.1: Energy and power densities of various EESS [1, 2]

1.1 Lithium-ion Batteries

Due to their higher theoretical and practical energy density, lithium-ion batteries are attractive power sources for portable consumer electronic applications that include Hybrid Electric Vehicles (HEVs) and Electric Vehicles (EVs). The basic working principles of LIB are shown in Fig. 1.2.

Lithium-ion battery is rechargeable and has four primary components namely a cathode (lithium metal oxide or positive electrode), a anode (graphite/silicon or negative electrode), a separator (porous polymer) and an organic electrolyte. The separator separates the positive and negative electrodes while allowing ions to pass through. The anode, cathode and the separator are submerged in the electrolyte solution. For today's commercialized LIB system, both cathode

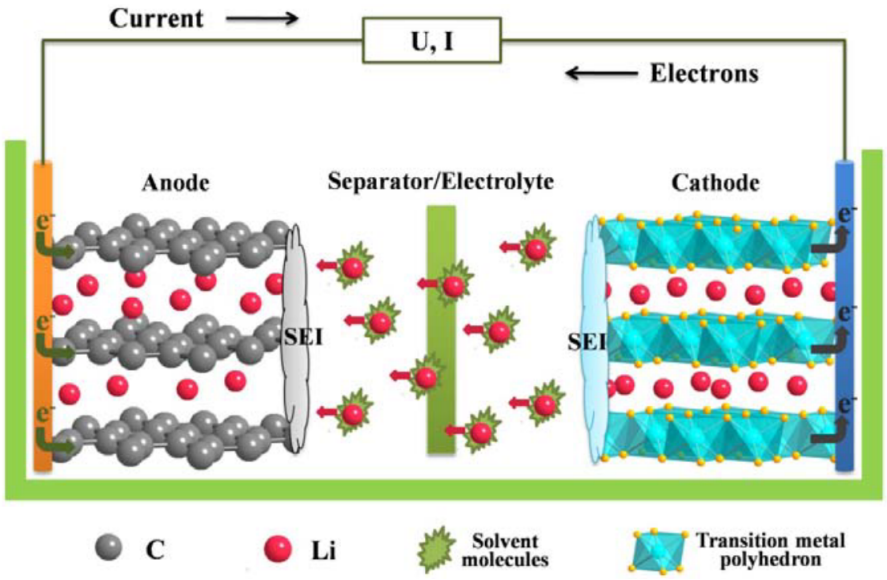

Figure 1.2: LIB working principle while charging [3]

and anode materials are intercalation materials. The transition metal oxides in cathode consist of a largely unchangeable host with specific sites for Li ions to be intercalated in.

Initially, all Li^+ ions are in the cathode and the battery system is assembled in a discharged state. While charging, Li^+ ions are extracted from the cathode host, solvate into and move through the non-aqueous electrolyte, and intercalate into the anode host. Meanwhile, electrons also move from cathode to anode through the outside current collectors, forming an electric circuit. The chemical potential of Lithium is much higher in the anode than in the cathode and thus the electrical energy is *stored* in the form of electrochemical energy. This process is reversed when the battery is discharging wherein the electrochemical energy is *released* in the form of electric energy. The cathode region and anode region are kept apart by the *separator*, a micro-porous membrane that allows the electrolyte to permeate and prevents shorting between the two electrodes. In principle,

the electrolyte should be ionically conducting and electronically insulating. However, the actual properties of the electrolyte are much more complicated.

During the first cycle, a so-called solid-electrolyte-interphase (SEI) layer will be formed on the surface of electrodes due to the decomposition of organic electrolyte at extreme voltage range (typically <1.2V and >4.6V). In the current LIB technology, the cell voltage and capacities are mainly determined by the cathode material that is also the limiting factor for the rate of Li transportation. The developments of cathode materials therefore become extremely crucial and receive much attention in recent decade.

Since 1980, when the $LiCoO_2$ was first demonstrated as a possible cathode material for rechargeable lithium battery [4], the transition metal intercalation oxides have caught the imagination of researchers as the LIB cathodes [5, 6, 7, 8, 9, 10]. Categorized by structure, the conventional cathode materials include layered compounds $LiMO_2$ (M = Co, Ni, Mn etc.), spinel compounds LiM_2O_4 (M=Mn etc.), and olivine compounds $LiMPO_4$ (M = Fe, Mn, Ni, Co etc.). A large bulk of the research is performed on these materials and their derivatives. New structure intercalation materials such as silicates, borates and tavorites are also gaining traction in recent years. During the materials optimization and development, following design criteria are often considered:

- Energy density
- Rate capability
- Cycling performance

- Safety
- Cost

The energy density is determined by the material's reversible capacity and operating voltage, that are mostly determined by the material's intrinsic chemistry such as the effective red-ox couples and maximum lithium concentration in active materials. For rate capability and cycling performance, electronic and ionic mobilities are the key determining factors. Additionally, particle morphologies are also important due to the anisotropic nature of the structures that could play a crucial role in some cases.

While some materials such as $LiFeBO_3$ and $LiFeSO_4F$ are already approaching the limit of their theoretical energy densities, for other materials, including conventional layered and spinel compounds, significant gaps are still present between their theoretical and practical energy densities. These materials with promising theoretical properties are potential candidates for next generation LIB cathode material. However, their charge and discharge rate capacity and cycling performance still needs improvement. The intercalation and de-intercalation process is the major mechanism which is responsible for the capacity loss of these materials. It involves the insertion of Li+ into interstitial sites in the crystal without changing the basic crystal structure. However, there are several other issues with lithium-ion batteries such as lithium plating, dendrite growth, Solid Electrolyte Interphase (SEI) layer growth etc.

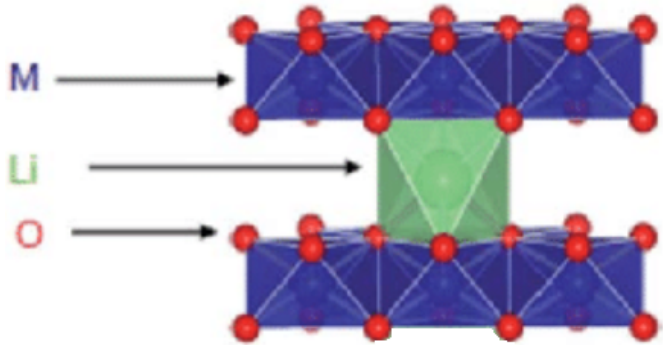

Figure 1.3: Layered $LiMO_2$ crystal structure (M: transition metal ions; Li: Li ions)

1.2 Cathode Materials for Lithium-ion Batteries

Generally, cathode materials are divided into three categories, layered compounds ($LiMO_2$), spinel compounds (LiM_2O_4), and olivine compounds ($LiMPO_4$), where M can be metal ions. $LiMO_2$, is the mostly used compounds, and an ideal structure of layered compound $LiMO_2$ is demonstrated in Fig. 1.3. The oxygen anions (omitted for clarity in the figures) form a close-packed fcc lattice with cations located in the 6-coordinated octahedral crystal site. The MO_2 slabs and Li layers are stacked alternatively. Though the conventional layered oxide $LiCoO_2$ has been commercialized as the LIB cathode nearly twenty years ago, it can only deliver about 140mAh/g capacity which is half of its theoretical capacity. This limitation can be attributed to the intrinsic structural instability of the material when more than half of the Li ions are extracted. On the other hand, the presence of toxic and expensive Co ions in $LiCoO_2$ not only presents an environmental issue but also raises the cost of the LIB. To overcome these, the Co ions in $LiCoO_2$ can be substituted by other transition metal ions such as Ni and Mn. With such substitutions for Co, the cathode material can become inexpensive and also be environmentally friendly.

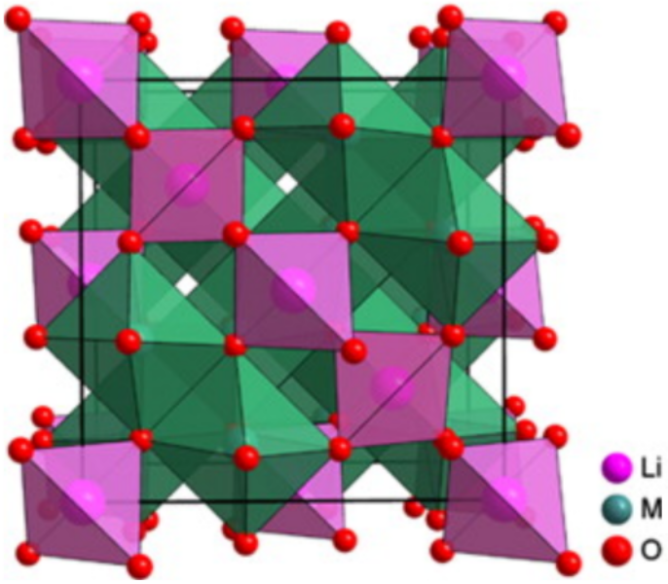

Figure 1.4: Spinel LiM_2O_4 crystal structure (M: transition metal ions; Li: Li ions)

The structure of LiM_2O_4 spinel is shown in Fig. 1.4. The oxygen framework of LiM_2O_4 is the same as that of $LiMO_2$ layered structure. M cations still occupy the octahedral site but 1/4 of them are located in the Li layer, leaving 1/4 of the sites in transition metal layer vacant. Li ions occupy the tetrahedral sites in the Li layer that share faces with the empty octahedral sites in the transition metal layer. The structure is based on a three-dimensional MO_2 host and the vacancies in transition metal layer ensure the three-dimensional Li diffusion pathways. The $LiMn_2O_4$ spinel was proposed as the cathode of the Lithium-ion battery by Thackeray et al. in 1983[11, 12, 13]. However, it was found that the material has severe capacity fading problems. Substituting Mn with other metal ions has been used as a key approach to improve cycling performance of spinel materials. Multiple dopants including inactive ions such as Mg, Al etc. [14, 15], first row transition metal ions such as Ti, Cr, Fe, Co, Ni, Cu, etc. [16, 17, 18] and

rare earth metal ions such as Nd, La, etc. [19, 20] have been investigated and $LiNi_{0.5}Mn_{1.5}O_4$ shows the best overall electrochemical performances among the above. The voltage of these materials can be raised to more than 4.7V, helping improve its energy density.

1.3 Issues with Lithium-ion Batteries

Stress-induced material damage, underutilization, capacity fade, and the potential for thermal runaway [21], are significant issues with existing Lithium-ion battery technology. Present issues with lithium-ion batteries can be broadly classified at three different levels i.e. market level, system level, and single cell sandwich. At the market level, factors such as cost, life and safety are key considerations for the end consumer. At the system level, issues such as cell underutilization, capacity fade (ageing), lower energy density and thermal runaways are most critical. These issues can be examined and understood well at the cell sandwich level, by studying physical or chemical phenomena occurring at the electrodes, electrolyte, separator, and their interfaces more critically. These shortcomings are generally attributed to major issues associated with Solid-Electrolyte Interface (SEI)-layer growth on electrodes, mechanical degradation and loss of active materials.

Since observing these phenomena experimentally at cell might be difficult or not feasible, application of modeling, simulation, and systems engineering techniques is a viable option to address these issues to enhance system level performance and improve product quality. Fundamental modeling approaches coupled with systems engineering techniques can provide a set of powerful tools

for better design, creation, and operation of lithium-ion battery systems. The development of new materials (e.g. molecular constituents and material nano- and macro-scale structures), electrolytes, binders, and electrode architecture are likely to contribute towards improving the performance of batteries.

In general, performance of the battery is dependent on the type of electrodes, electrolytes, and electrode-electrolyte interfaces, being used. Additionally, safety is also related to the stability of the electrode materials and its interface with electrolyte. Hence, there have been extensive investigations [22, 23] into the battery electrodes and electrolyte materials to improve its safety and performance. For example, to avoid using expensive Cobalt material in the cathode material ($LiCoO_2$), notable advances in recent years are the use of $LiFePO_4$ or $Li_xMn_2O_4$ as a cathode which improves both capacity retention during charge and discharge cycles and the batteries have a high discharge performance.

1.3.1 Capacity fade in the lithium-ion batteries

The capacity of lithium-ion battery decreases overtime with cycle repetitions. This is one of major drawbacks in lithium-ion battery systems which ultimately increase the total costs and payback period of such systems. There are several factors which can lead to capacity fade in the Lithium-ion batteries. These include lithium deposition due to overcharge, dissolution of active material, electrolyte decomposition, sharp phase boundaries in phase changing active materials, passive SEI layer formation over electrode surfaces etc. [24].

Besides these, another important cause of capacity fade is mechanical degradation of active material as it causes breakup of particles, delamination etc. which

lead to loss in the capacity. Stress development in the particles due to lithium intercalation and de-intercalation cause fracture and delamination in the active material. Specificaly, during lithium insertion, the outer shell expands, creates a strain differential between the lithium rich outer layers and the lithium deficient inner layers of the particle, which increases the stress within the particle.

It has also been reported that a prolonged accumulation of stress may even lead to electrode cracking [25] Apart from insertion and extraction of lithium-ion, structural failures also arise due to heat generation and concentration gradient developed during charge-discharge cycles at different operating conditions. These findings demand the need to simultaneously monitor the effect of predominant parameters on the performance of lithium-ion batteries.

It is essential to know the fundamental mechanisms of the capacity fading, because an in-depth understanding is helpful to improve the cell life. However, the cell failure mechanisms are not fully understood yet, especially for special electrode materials, as the diagnosis of cell failure is very challenging. Since Lithium-ion batteries are complicated systems, a mathematical model would be a great help for understanding the complex phenomena.

Capacity fading of the cathode material due to internal stress generation during cell cycling is within the scope of this research [26, 27, 28, 29]. Zhang et al. [26, 27] have also developed a mathematical model for calculating intercalation-induced stress, and subsequently appended a heat model to it. Among several factors affecting outcome of stress in lithium-ion battery, diffusion of lithium-ions in electrode particles plays a vital role. Except the above literature, there

is very little work done on lithium-ion diffusivity induced intercalation stress modelling especially at elevated temperatures. Additionally, stress which is dependent on both temperature and concentration would be interesting to analyze. These are studied in detail in this thesis.

For a given chemistry, better fundamental understanding along with systems engineering approach can be used to optimize the electrodes, life cycle, operational strategies, and device performance by maximizing the system efficiency and reducing the potential problems. There can be several routes to understand and solve of these problems such as experimental or numerical model developments.

Fundamental model development coupled with other systems engineering approaches can be used to study the following issues in batteries:

- Battery capacity fading.
- Understanding degradation mechanisms.
- Effect of varying operating conditions and material properties on the lifetime of a battery.
- Effect of the battery design parameters and operating conditions on the performance of the batteries.
- Model predictive control that incorporates real-time estimation of State-of-Health (SOH) and SOC.

Difficulties in performing the experimental studies and issues with accuracy to understand the fundamentals at smaller scale is a big motivation behind several numerical modeling of lithium-ion batteries.

1.4 Modeling of Lithium-ion Batteries

Developing a model is the core part of the systems engineering approach for developing real time control strategies and achieving optimal design of batteries. Generally, developing a detailed and high precision multi scale or multi-physics model is computationally very expensive. Therefore, model development efforts start with a simple model and then additional functionalities to model the multitude of phenomena at various time and length scale are added gradually until the model predictions are sufficiently accurate to achieve the objectives. Another important task after the development of model is its experimental validation to ensure that the model predicts the experimental data fairly accurately.

However, for a lithium-ion battery, most variables such as lithium-ion diffusion coefficient, Young's modulus and activation energy in the system are not directly measurable during charge-discharge cycles. Hence they are not available for comparison to verify the accuracy of the assumptions made in the derivation of the model. Also, model parameters that cannot be directly measured experimentally typically have to be obtained by comparing the experimental data with the model predictions. Mathematical models for lithium-ion batteries vary widely in terms of computational efficiency, complexity, and accuracy of the solutions.

Fig. 1.5 [21] shows a comparison of the Lithium-ion battery models reported in literature with respect to their prediction abilities and computational cost. It is obvious that inclusion of additional physics in an existing battery model improves its predictions but also increases the model's complexity and computational costs which are not useful for real time control and optimization purposes. Hence, it is normal to find a suite of battery models that vary in their complexity and computational costs to suit a variety of needs in different applications. Generally, lithium-ion battery models can be roughly classified into four categories: empirical models, electrochemical models, multi-physics models and molecular or atomic models.

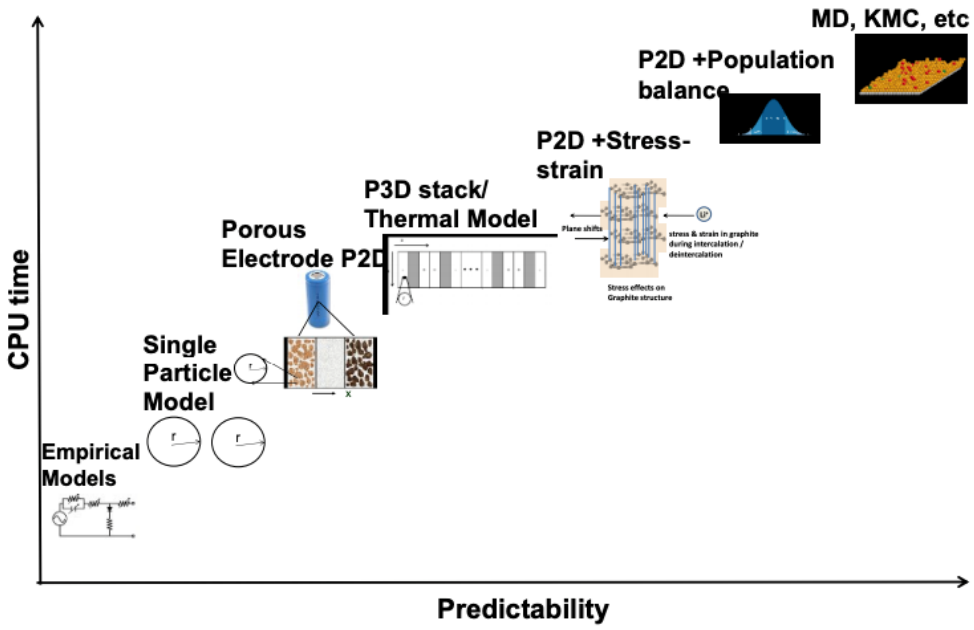

Figure 1.5: Lithium-ion battery models for different scales and the corresponding computational time [30, 21]

Empirical models: Since these models use observed experimental data to predict future behavior of lithium-ion batteries, from a computational point

of view, these models are most efficient. Empirical models consist of functions like, polynomials, exponentials, power law, logarithmic, and trigonometric functions, and they completely ignore physical and chemical principles. Such battery models are not very useful for new battery designs. Moreover, since these models are developed by fitting experimental data for specific operating conditions, very low accuracy is expected when empirical models are used for a different set of operating conditions [29].

Electrochemical engineering models: Models that fall under this category include the continuum scale models which couple chemical and electrochemical kinetics with transport phenomena to predict battery behavior. These models are comparatively more accurate than empirical models. The single particle model (SPM), developed by Zhang et al. [31], approximates the anode and cathode of the cell sandwich each as a single particle with the same surface area as the electrode. In this model, diffusion and intercalation are considered within the particle which means that it solves for mass and charge balance in solid phase. Concentration and potential effects in the solution phase between the particles are neglected. From a computational cost perspective, this model is on the lower side but it is valid for limited situations such as low rates and thin electrodes due to the assumptions.

The next level of complexity in this category of Lithium-ion battery models is the Ohmic porous-electrode model [32, 33, 34]. It incorporates solid and electrolyte phase potentials and current but neglects the spatial variations in concentration. Either linear or exponential kinetics are chosen to represent

electrochemical reactions in this model. Furthermore, mass and charge transport parameters like diffusivities, conductivities etc. are varied as functions of porosity of electrodes.

The pseudo two dimensional or P2D model [35] is by far the most widely used model in battery literature. It has proven to be very accurate for a wide range of operating conditions and has been experimentally validated for high as well as low rates of charge and discharge. The P2D model developed by [35], is based on concentrated solution theory involving transport phenomena as well as thermodynamics, capturing the internal behavior of a lithium-ion cell sandwich consisting of positive and negative porous electrodes, a separator, and current collectors. It solves for both the electrolyte and solid-state mass and charge balances within the porous electrodes, and the electrolyte concentration and electrolyte potential within the separator.

Multi-physics models: Multiscale and multi-physics models are necessary to understand the complicated physics behind lithium-ion battery operation especially for applications demanding high power and energy. Adding thermal models to include temperature effects into the P2D model adds complexity but increases the accuracy level. To overcome this additional computational load, many researchers solve only for a global energy balance by decoupling thermal model from the electrochemical model [36, 37, 38, 39, 40]. However, a major limitation of this technique is the inability to monitor local parameters like current densities and state of charge which affect thermal gradients inside the cell. Global energy balance is only valid for uniform reaction distribution within the cell. Therefore, these models cannot be employed to understand the effects

on cell performance since it neglects the local temperature effects.

Some researchers have presented 2D thermal electrochemical coupled models for lithium-ion cells to understand the effects of local heat generation [41, 42]. Recently, researchers have begun developing 3D thermo-electrochemical models for better understanding of the dynamic operation and control of lithium-ion batteries for large-scale applications. However, these models are computationally expensive even with several approximations which results in various shortcomings; Some models cannot observe the thermal effect of electrochemical parameters [39, 43], while other large scale Computational models need empirical input from experiments or other simulations [44, 45]. A Multi-Scale and Multi-Dimensional (MSMD) model [46] and a model derived from a grid of 1D electrochemical/thermal models [47] have also been implemented for 3D thermal simulation of batteries. Lithium intercalation or de-intercalation into the electrode particles during charge and discharge of a battery causes expansion and contraction of the active material and this develops stresses which can fracture the particles, eventually leading to a reduction in capacity of the battery due to loss of active material. Moreover, the pressure gradients inside the particles impact the concentration profiles, that will have an additional influence on the functioning of a battery.

Therefore, multi-physics models are needed to be developed which capture the pressure induced diffusion and stress generation in active material particles in lithium-ion batteries. In general, porous materials rarely have uniform particle size and shape. During cycling, active material particles de-laminate from the substrate or agglomerate to form larger sized particles. Therefore, to integrate

the effect of particle size distribution on battery performance, researchers have reported the development of continuum models in literature [48]. To capture the effect of morphology within battery active material, mesoscale models [49] have been developed that can simulate materials degradation due to spatially-varying and time-varying changes in the particle size and shape distribution.

Molecular or Atomistic models: These models are required to understand phenomena occurring at the lattice or molecular scale during lithium-ion battery operation. The Kinetic Monte Carlo method is a stochastic technique that has been employed to study diffusion of lithium-ion between lattice sites within an electrode particle including the effect of crystal structures on mobility of ions etc. [50, 51]. The growth of passive solid electrolyte interface (SEI) layer on the surface of anode particles, one of the major causes for capacity fade of batteries, has been studied extensively with these methods [52].

Molecular dynamics (MD) techniques have been used to gain insight into the SEI layer growth mechanisms, especially at the start of lithiation (like the first tens of picoseconds) [53]. MD methods have been extensively used for simulation of effective diffusivities [54]. Density functional theory (DFT) simulations are also very useful for a detailed study and understanding of several phenomena occurring during battery operations, namely, structural changes in particles during repetitive cycles [55], stability of organic electrolytes is very crucial for SEI layer growth, etc. [56]. Chen and Verbrugge [57, 58, 59, 60] have also studied the diffusion induced stress variation with respect to lithium-ion concentration, electrode material and electrode geometry using MD techniques. However, there is no clear link establishing the effect of heat generation on capacity fade due

to lithium-ion intercalation stress. The understanding of ionic mechanisms, determination of diffusivity, and the variations in heat generation due to lithium-ion intercalation is very important for an efficient battery design.

Ab-initio calculations or Quantum Mechanics (QM) based calculations have been used to find diffusivity of lithium-ion in LiMn2O4 (cathode material) [61]. Additionally, Classical Molecular Dynamics (CMD) have also been used to study the lithium-ion diffusivity in LiMn2O4 [62, 63, 64]. However, molecular dynamics based simulations which covers stress induced thermal influence on electrode material, especially on doped structures, still has a long way to go.

1.5 Research Objectives

The objective of this dissertation is to develop a molecular/atomic level mathematical model to understand capacity fade due to Lithium-ion intercalation/de-intercalation induced stress. To do this, we will be employing an open source based mathematical model (LAMMPS) [65] to study $Li_xMn_2O_4$ cathode material behavior during lithiation and de-lithiation process and find ways to improve it. The final objective of this thesis is to use these computational tools to design and propose novel engineered micro-structures with significantly enhanced electro-mechanical properties, making them applicable for the design of next-generation LIBs.

The rest of the thesis is organized as follows: In Chapter 2, the simulation set up involving the Molecular Dynamics modelling of $LixMn_2O_4$ using LAMMPS

and the validation of this computational tool with experimental data from various literature is presented. Chapter 3 introduces the exploratory investigation in which novel cathode chemistries are explored using this computational tool. This is done by investigating a carefully chosen set of doping and co-doping elements along with Multi-scale modeling of undoped, doped and co-doped LMO spinel material. In order to verify the structures obtained from MD simulations, additional QM simulations are performed and explained in detail. Chapter 4, extending the search space to more number of co-doping elements along with Sulfur and Fluorine anions doping. Which span millions of possible crystal configurations, a combination of Neural Network and Multi-Scale modeling is applied to an exhaustive set of doped and co-doped structures to identify optimal cathode chemistries. A detailed conclusion from the results of this thesis and the potential future work is presented in Chapter 5.

Chapter 2

Molecular Dynamics Modelling of $Li_xMn_2O_4$

PRELUDE: This chapter is been re-produced from the following manuscript with the permission of AIP Publishing:
R. Tyagi and S. Srinivasan, "Molecular dynamics modeling of lithium ion intercalation induced change in the mechanical properties of Li_xMn_2O4", J. Chem. Phys, 2020, 153, 164712.

Contributing Author: Ramavtar Tyagi

Abstract: The objective of this study is to understand the fracture mechanisms in the Lithium Manganese Oxide ($LiMn_2O_4$) electrode at the molecular level by studying mechanical properties of the material at different values of the State of Charge (SOC) using the principles of molecular dynamics (MD). A $2 \times 2 \times 2$ cubic structure of $LiMn_2O_4$ unit cell containing 8 lithium ions, 8

trivalent manganese ions, 8 tetravalent manganese ions, and 32 oxygen ions, is studied using LAMMPS. As part of the model validation, the lattice parameter and volume changes of $Li_xMn_2O_4$ as a function of SOC ($0 < x < 1$) has been studied and validated with respect to the experimental data. This validated model has been used for a parametric study involving the SOC value, strain-rate (charge and discharge rate), and temperature. The MD simulations suggest that lattice constant varies from 8.042Åto 8.235Å during a full discharging cycle, in agreement with the experimental data. The material at higher SOC shows more ductile behavior compared to low SOC values. Further, yield and ultimate stresses are less at lower SOC values except when SOC values are within 0.125 and 0.375, verifying the phase transformation theory in this range. Strain-rate does not affect the fully intercalated material significantly but seems to influence the material properties of the partially charged electrode. Finally, a study of the effect of temperature suggests that diffusion coefficient values for both high and low-temperature zones follow an Arrhenius profile, and the results are successfully explained using the vacancy diffusion mechanism.

2.1 Background

A significant amount of current research is focused on $LiMn_2O_4$ as a cathode material for lithium ion batteries [1, 2, 3, 4, 5]. $LiMn_2O_4$ is being preferred over other cathode material such as lithium cobalt oxide ($LiCoO_2$) and lithium nickel oxide ($LiNiO_2$) because of its low cost, high operating voltage, higher energy density and low toxicity as a cathode material [6, 7].

However, this is a challenging material to work with because it shows a large

volume change during lithium ion intercalation and de-intercalation processes. Specifically, these processes induce stresses which can initiate fracture inside the material [8, 9, 10], a key degradation mechanism in the lithium ion batteries [11, 12, 13, 14]. It must be noted that stress is strongly dependent on the Lithium content in the electrode [15]. Extensive macro level mathematical and computational work has been done to study the mechanical properties of Mn_2O_4 as a host material on lithiation, mostly focusing on Young's modulus that varies quite a bit (10-200GPa) across the literature for $LiMn_2O_4$ [11, 10, 16, 14]. Molecular and atomistic simulations can provide better understanding of the variations in such mechanical properties due to lithium ion intercalation and de-intercalation process.

The movement of lithium ions within the cathode material is dictated by the diffusion coefficient of the electrode material. The value of diffusion coefficient will vary with SOC values, as the availability of the vacant sites change. Therefore, studying the transition of lithium ions at the molecular level will improve our understanding of the material's response during charging and discharging processes. Additionally, it is important to note that as the temperature inside the cell increases, energy level will also increase, facilitating a faster diffusion of the ions. Thus, there is an increase in the overall diffusion coefficient for these ions. Currently, research work which focuses on temperature influence on lithium ion diffusivity at various SOC values for $Li_xMn_2O_4$ is limited in the literature and there is a significant variation in the diffusivity values [16, 10, 11, 14]. Further, it is very difficult to perform precise experiments at the molecular level. This is evident from the wide range of diffusion coefficients values at room

temperature (10^{-8} to 10^{-15} cm^2/s) that have been reported in the literature, using the different experimental methods [17, 18, 19]. This is because the transport and other properties depend strongly on the preparatory procedures, which influence the micro structure, defects, and atomic structure of the $LiMn_2O_4$.

To address this shortfall, in addition to the impact of SOC on diffusion coefficient, influence of the elevated temperature on the structure of $Li_xMn_2O_4$ will be studied in this article. Further, charge and discharge rate (strain-rates) is also investigated as part of the parametric study in the strain-rate section. The rest of the article is organized as follows. In the section 2.2 we describe the details of the molecular dynamics simulations, including the analysis of the effect of the cutoff length. In this section we also outline the theoretical framework for the analysis of the mechanical properties and the diffusion coefficient. In the section 2.3, we present the validation of the computational tool and the outcome of the parametric analysis. Finally, we present the main conclusions from our findings for this chapter.

2.2 Computational Tools

Molecular dynamics (MD) simulations have been used to calculate the mechanical properties of the $Li_xMn_2O_4$. MD simulations have been preferred over other type of numerical modeling of chemical physics problems because they can capture the dynamic behavior of the ions, and can help us understand the underlying physics at a molecular scale. The ensuing paragraphs describe the simulation tool in detail[20, 21, 22].

2.2.1 Molecular Dynamics Simulations

Interactions between various ions determine the potential which is responsible for atomic movement, that will eventually govern the mechanical and chemical properties. In this work, Gilbert-Ida-type pair potential function [23] has been used to calculate the inter-atomic pair potentials as:

$$E = \frac{Z_i Z_j e^2}{r_{ij}} + A_{ij} \exp\left(\frac{\sigma_{ij} - r_{ij}}{\rho_{ij}}\right) \qquad for \qquad r_{ij} < r_c, \tag{2.1}$$

where the first term represents the electrostatic interactions, and the second term represents the exchange repulsion interactions. Z_i and Z_j are the atomic charge of atoms i and j, respectively, and r_{ij} is distance between atoms/charges. Further, σ_{ij} is an interaction-dependent length parameter, ρ_{ij} is an ionic-pair dependent length parameter, r_c is the cut off length, and e is the elementary electric charge. Potential function parameters reported by Suzuki et al. [24], and as summarized in Table 2.1, are used to calculate the values of A_{ij}, σ_{ij} and ρ_{ij} for each pair interaction, where

$\rho_{ij} = b_i + b_j$, $A_{ij} = f_0 \times \rho_{ij}$, $\sigma_{ij} = a_i + a_j$ and f_0 is a constant.

Table 2.1: Parameters for the potential function.

Ion	Z_i	a_i(Å)	b_i(Å)
Li^+	+1.0	1.043	0.080
Mn^{3+}	+1.4	1.038	0.070
Mn^{4+}	+2.4	0.958	0.070
O^{2-}	−1.2	1.503	0.075

A unit cell of $LiMn_2O_4$, contains 56 ions (8 Li^+, 8 Mn^{3+}, 8 Mn^{4+} and 32 O^{2-}),

and these ions are in a cubical structure in the Fd3m space group. The atomic coordinates of these 56 particles were taken from a study performed by Sickafus et al. [25].

Cutoff length

From Equation 2.1, it is clear that inter-atomic pair potential depends upon the cutoff length, beyond which the interaction potential can be neglected. While increasing cutoff length will improve the accuracy of the solution, there is a significant increase in the computational cost.

To understand the trade off between accuracy and cost, and to choose an optimal cutoff length, three different cutoff lengths (6Å, 8Å and 10Å) have been considered. More precisely, MD simulation were made for two different SOC values, i.e., SOC=1 and SOC=0.5, using the three cutoff lengths for each SOC value. The results from these simulations are shown in Figure 2.1 and 2.2, respectively.

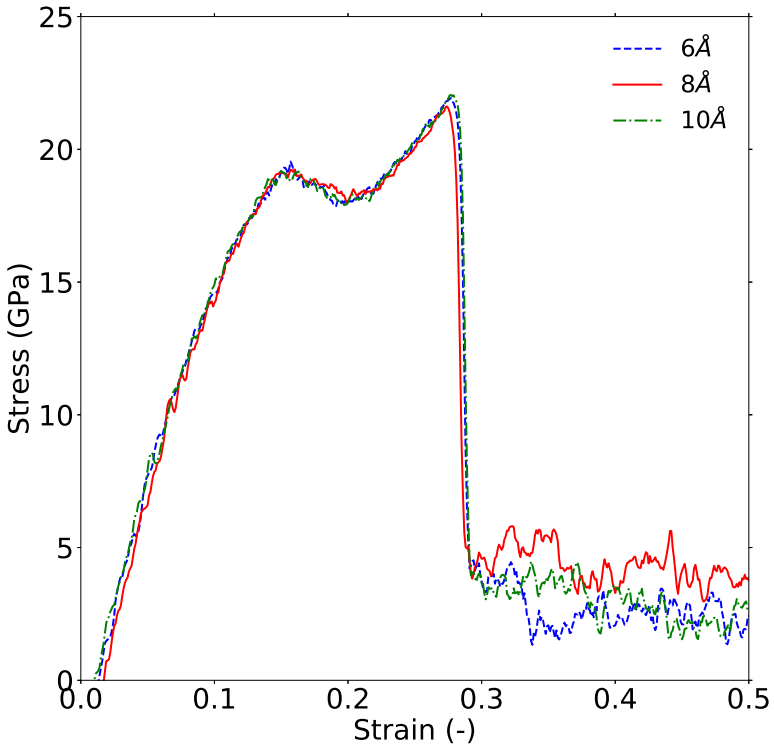

Figure 2.1: Stress-strain curve for different cutoff length at SOC=1.

As seen in Figure 2.1, the effect of either of these cutoff lengths on the variations in the stress-strain relationship is minimal. This is because when SOC = 1, the number of vacant sites is minimal, and so the diffusion activity is largely subdued. Hence, for this situation, a lower cutoff length would still produce a fairly accurate result.

Figure 2.2 shows the results of the MD simulations when SOC = 0.5. As seen in this figure, the stress-strain relationship predicted by the cutoff lengths of 6Å or 10Å are quite similar. However, the computational time for 10Å case is approximately 1.5 times longer than the 6Å case. When the cutoff length is 8Å, we notice some insignificant variations in the stress-strain relationship.

Hence, keeping in mind the boundary effects on the solution and computational cost, in this work, the cutoff length was chosen as 10Å for all the MD simulations. We believe that increasing the cutoff length any further is not likely to improve the accuracy of the calculations significantly.

It must be noted that this cutoff distance of 10Å is greater than the size of a unit cell which is 8.24Å. Therefore, a minimum of two-unit cells are required to perform MD simulations. However, increasing number of unit cells results in larger simulation box which will increase the computational load and thereby the cost.

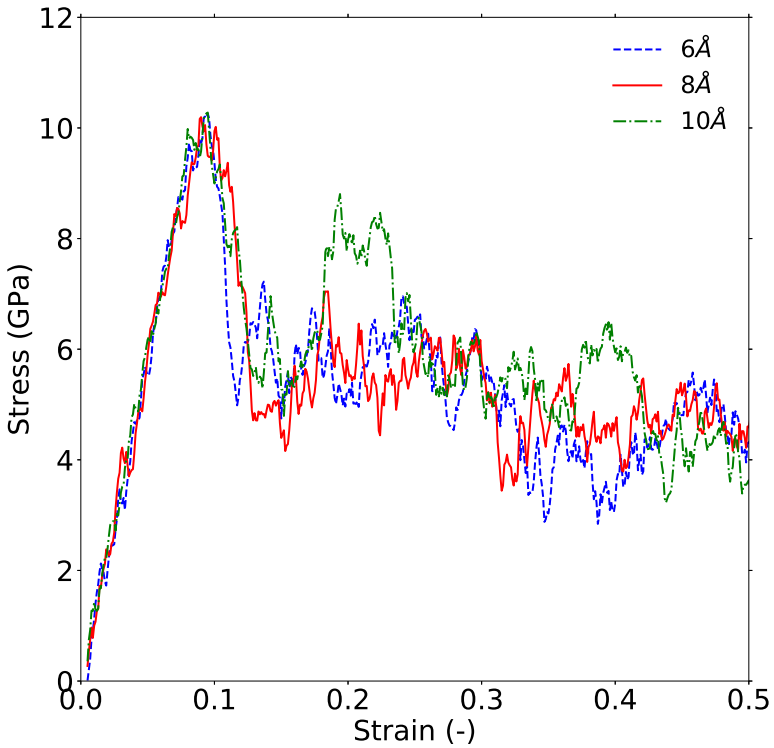

Figure 2.2: Stress-strain curve for different cutoff length at SOC=0.5.

Hence, in all the simulations of this work, we have used a $2 \times 2 \times 2$ simulation box in x, y and z-directions, respectively. The front view and the 3-dimensional

view of the $2 \times 2 \times 2$ simulation box are shown in Figure 2.3.

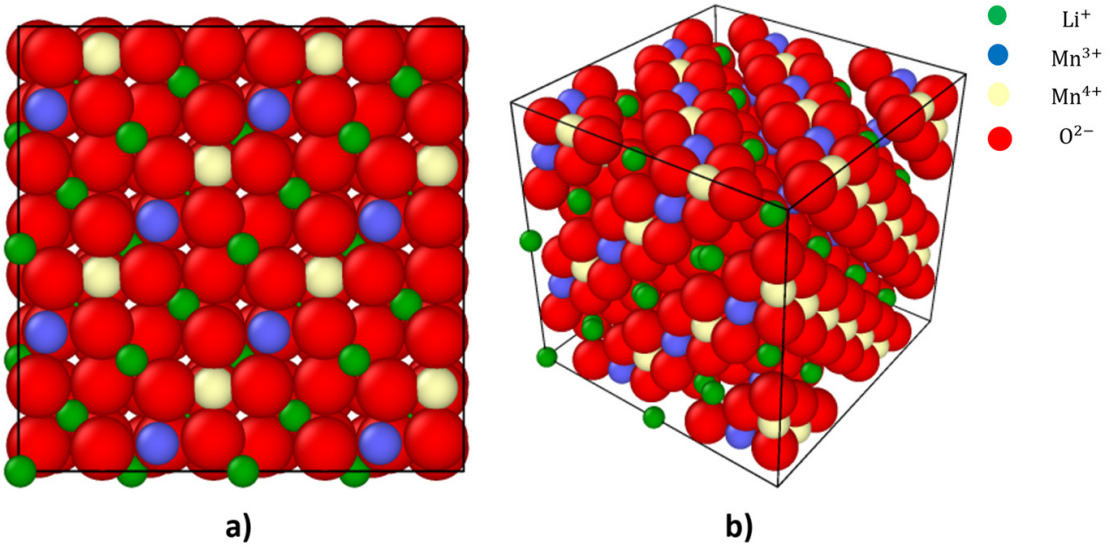

Figure 2.3: $LiMn_2O_4$ simulations box: (a) Front view, (b) 3D view.

All MD simulations are performed using LAMMPS (Large-scale Atomic / Molecular Massively Parallel Simulator) [26] open source based software which is a classical molecular dynamics code. To calculate the inter-atomic potential described in Equation 2.1, it is transformed into Buckingham potential available in LAMMPS[27, 28]. Ewald method is used for computing the long-range coulombic interactions[29]. The isothermal isobaric (NPT) ensemble is used during equilibrium and production processes, and canonical ensemble (NVT) is used for strain simulations. For NPT ensemble, the number of particles, pressure and temperature of the simulation box is kept constant. On the other hand, for NVT ensemble, the volume along with the number of particles and temperature are kept constant. Nose–Hoover thermostat has been used to regulate the system's temperature at specific temperatures[30].

Simulations are performed in two stages: first, optimized structures are found

by running initial configurations for one-time step, and four cases with the least potential energies are subsequently equilibrated along with the production simulations. An average of the data from these cases is presented as the final result. Further, based on the SOC values, there are nine possible scenarios, corresponding to the number of lithium ions in the system that can vary from 0 to 8. The corresponding SOC values vary from 0 to 1 with an increment by 0.125 for each additional lithium ion. As the number of lithium ions increase, an equivalent number of Mn^{4+} switch to Mn^{3+} sites to maintain system's neutrality.

All lithium ions are positioned on the 8a tetrahedral sites, manganese (Mn^{3+} and Mn^{4+}) are placed at 16d octahedral sites, and O^{2-} are located at the 32e sites. Due to the complexity of the $LiMn_2O_4$ structure, numerous initial configurations are possible as the ion occupies one of these positions. For example, in a fully discharged state, when lithium ions intercalate into $Li_xMn_2O_4$ (x = 1), the number of possible cases in which Li^+, Mn^{3+} and Mn^{4+} could be arranged in the vacant sites would be 12,870. Similarly, for other SOC values there will be numerous potential configurations, as summarized in the Table 3.1:

Table 2.2: Possible $Li_xMn_2O_4$ configuration for each SOC

SOC	No. of Li+ ions	Possible configurations
0.000	0	1
0.125	1	128
0.250	2	3360
0.375	3	31360
0.500	4	127400
0.625	5	244608
0.750	6	224224
0.875	7	91520
1.000	8	12870

As shown in Table 3.1, there is a total of 735,471 possible initial configurations that could be optimized. However, checking equilibrium energy for all these cases would not be computationally feasible. Therefore, as shown in Figure 2.3,

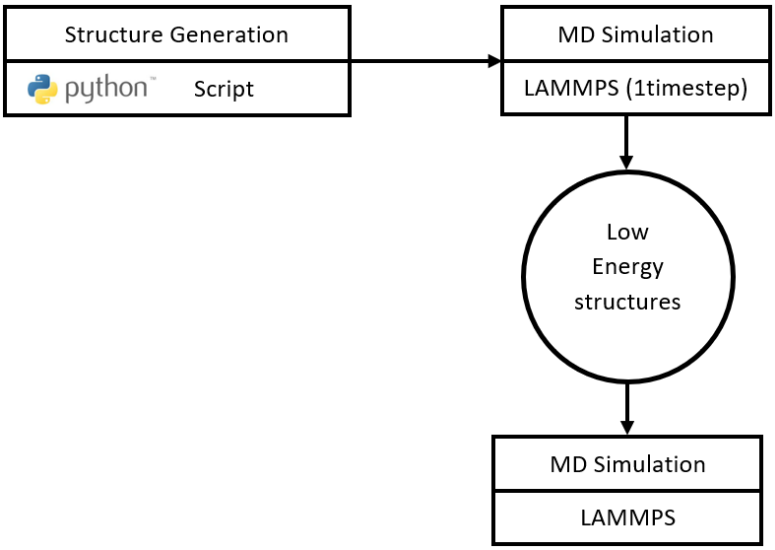

Figure 2.4: Python-LAMMPS connection for MD simulations

Python script is used to generate all possible structures and then one-step MD simulation is performed for all cases. Since a configuration with the lowest potential energy will have a higher probability of reaching an equilibration state quicker, four lowest potential energy cases from these simulations were picked for longer equilibration simulation. Finally, after equilibration of these four cases, the three cases with the lowest energy were selected for further production and analysis.

2.2.2 Mechanical Properties

Linear elastic relationship:

Stress is mainly calculated in the form of virial stress. Stress for a particular SOC structure has been calculated with LAMMPS[31] using the following equation:

$$\sigma(r) = \frac{1}{\Omega}\sum_{i}[-m_i \dot{u}_i \otimes \dot{u}_i + \frac{1}{2}\sum_{j\neq i} r_{ij} \otimes f_{ij}], \tag{2.2}$$

where Ω is the total volume, m_i is the mass of the atom i, $\dot{u}_i$ is the time derivative of u_i, which represents the displacement vector of atom i from reference position r_{ij}, and f_{ij} is the inter-atomic force applied on atom i by atom j. Young's modulus can be calculated from the stress results and analyzed with respect to SOC. Linear elastic stress-strain relationship during an axial test can be calculated using the following relation[32]:

$$\begin{pmatrix} \sigma_{11} \\ \sigma_{22} \\ \sigma_{33} \end{pmatrix} = \begin{pmatrix} C_{11} & C_{12} & C_{13} \\ C_{21} & C_{22} & C_{23} \\ C_{31} & C_{32} & C_{33} \end{pmatrix} \begin{pmatrix} \epsilon_{11} \\ \epsilon_{22} \\ \epsilon_{33} \end{pmatrix}, \tag{2.3}$$

where σ_{ij}, C_{ij} and ϵ_{ij} are the stress, elastic constant, and strain, respectively. The elastic bulk modulus K can be calculated as:

$$K = \frac{1}{3}\left(\frac{\sigma_{11} + \sigma_{22} + \sigma_{33}}{\epsilon_{11} + \epsilon_{22} + \epsilon_{33}}\right). \tag{2.4}$$

Finally, the effective Young's modulus can be evaluated using Equations 2.3 and 2.4 as:

$$E = \frac{9K(C_{11} - K)}{3K + C_{11}}. \tag{2.5}$$

Although strain is applied on the equilibrated system, stress will fluctuate depending on which equilibrium point is selected. Hence to obtain real converged solution convergence test was conducted by increasing number of equilibration points to 400.

Stress strain-rate:

Since chemical and mechanical properties of the cathode material like $LiMn_2O_4$ are strongly coupled, it is important to understand how C-rate (charge or discharge rate) influences the mechanical properties of the material. As mentioned earlier, mechanical stresses are induced with the expansion and contraction of the micro-structure during the charging and discharging processes. To measure this quantitatively, we can convert the charging rate into a strain rate using the Vegard relation as follows[33, 34]:

$$\epsilon_c = \beta_{ij} \Delta X, \tag{2.6}$$

where ΔX is the change in lithium concentration, and β_{ij} is the Vegard constant. Since the strain-rate will change with lithium ion concentration, the stress value calculated using Equation 2.2 will also change. From Equation 2.2, it is clear

that the ultimate and tensile stresses will be affected by the change in lithium concentration. Therefore, strain rate will have a direct impact on the material properties.

2.2.3 Lithium ion diffusion

With an increase in temperature, kinetic energy of the system and thereby the total energy of the system increases. Further, ionic movement will also increase, enhancing thermal diffusivity. As evident from Equation 4.6, chemical diffusion coefficient will also change with the State of the Charge, temperature and other parameters:

$$D(X) = D_0 X(1-X)\left(-\frac{zF}{RT}\frac{\partial V(X)}{\partial X} + \frac{2\Omega^2 E c_{max}}{9RT(1-\nu)}\right), \tag{2.7}$$

where D_0, X, F, V, Ω, c_{max}, E, ν are diffusivity coefficient, lithium concentration, Faraday constant, potential, partial molar volume of lithium, maximum lithium concentration, Young's modulus and Poisson's ratio, respectively.

To understand the influence of the temperature, multiple MD simulations were performed at various temperatures, and the corresponding diffusion constants were calculated using the Mean Square Displacement (MSD) of all the particles in the following formula:

$$MSD(t) = \overline{|r(t) - r(t_0)|^2}, \tag{2.8}$$

where r(t) and r(t_0) represents the atom coordinates at time t and t_0, respectively.

In the above equation, over-line shows the average over the same type of species. The diffusion coefficient of lithium ion can be determined from MSD values using the following Einstein equation:

$$D = \frac{1}{6} \lim_{t \to \infty} \frac{d}{dt} MSD. \tag{2.9}$$

2.3 Results and Discussion

2.3.1 Validation of the computational tool

To ensure the validity of the simulation results, the lattice parameter for the optimized $LiMn_2O_4$ structure at 300K is calculated. The lattice constant was calculated by measuring the size of the equilibrated system, and is shown in Figure 3.4 for various SOC values. As seen in this figure, there is a good agreement between the simulation results and the experimental data[35, 36].

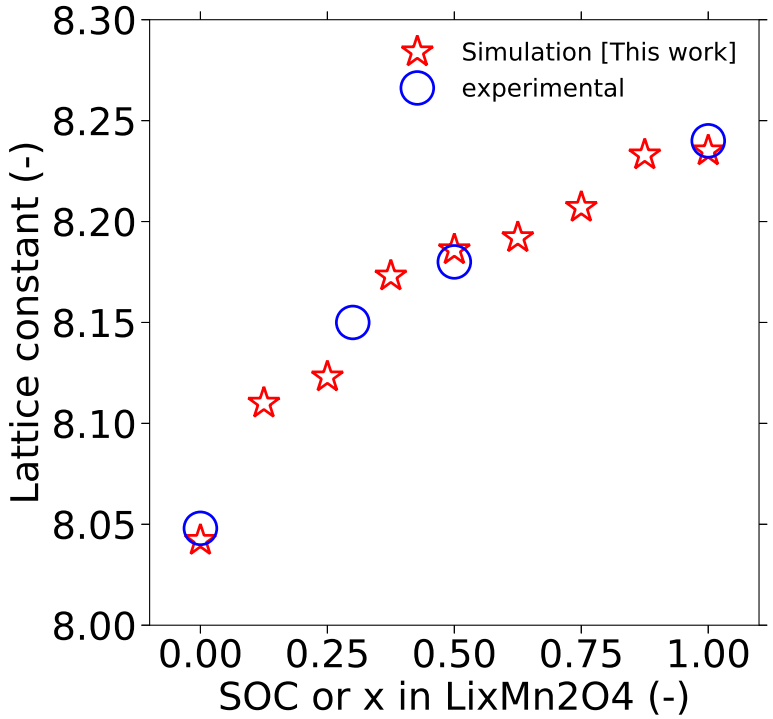

Figure 2.5: Lattice parameter with SOC.

More precisely, the lattice constant varies from 8.042Å (at x=0) to 8.235Å (at x=1) as we move from a fully charged state to a fully discharged state. The total change in the lattice length and volume during full charging cycle was 2.34% and 6.87%, respectively. It must be noted that this predicted volume change is in excellent agreement with the experimental value of 6.85% presented by Park et al.[16].

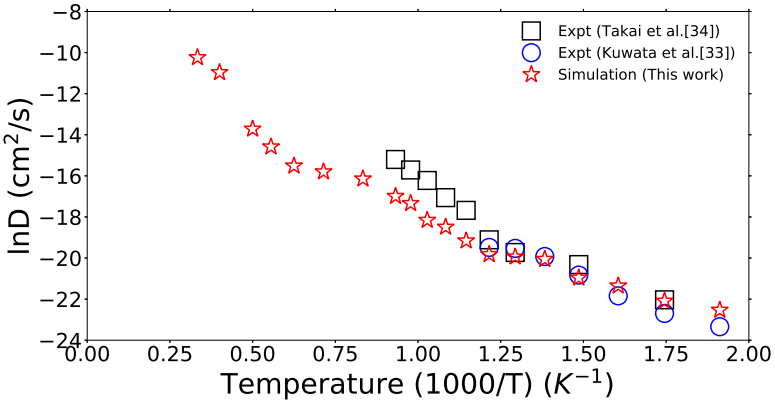

Figure 2.6: Lithium ion diffusion coefficient validation with experiments.

For additional validation of the simulation tool, lithium ion diffusion coefficient at various temperatures of $LiMn_2O_4$ has been compared with the experimental data from the literature, and is shown in Figure 2.6. As seen in this figure, the calculated diffusion coefficients, at various temperatures, are in good agreement with the experimental data of Takai et al.[19] and Kuwata et al.[18]. Specifically, the agreement is very good for a temperature in the range of 573K-1000K.

At temperatures below 573K the diffusion process slows down significantly, and so the simulation duration was increased from 2ns to 5ns. Kuwata et al.[18] extrapolated their experimental data and predicted a diffusion coefficient ($\sim 10^{-15}$ cm^2/s) at 298K that is several orders of magnitude lower than the chemical diffusion coefficient ($\sim 10^{-12}$ cm^2/s). On the other hand, the simulations from this work, using the principles of molecular dynamics, predict the diffusion coefficient as approximately 7.4×10^{-11} cm^2/s, and this value is well within the range of chemical diffusion coefficient at 300K[37].

The MD tool that is successfully validated with the experimental data has

been used to conduct a parametric study. Specifically, three parameters have been investigated in this work, namely, the state of charge, strain rate, and the temperature. From Equation 2.1 it is clear that the output potential that is dependent on pair interactions is governed by the lithium content in the cathode material. As the number of lithium ions increase, the SOC value changes, impacting the material property. Therefore, SOC is an important parameter to study. Since in almost all intercalation materials like $LiMn_2O_4$, intercalation induced fracture mechanism is active especially at high charge or discharge rates, it is necessary to study influence of the strain-rate on mechanical properties of the material[38].

Finally, as the temperature increases, ions will start moving quicker, increasing the kinetic energy of the system and thereby the total stress and diffusivity of the Lithium ions[39]. Therefore, temperature has been chosen as the third parameter to be investigated in this study, especially for different SOC states. Cutoff length range is another input parameter which can influence the potential value and thereby impact the calculations, making it an important parameter to investigate. We have investigated this to ensure that an optimal cutoff length is used in our MD simulations, as presented in Computational Tools section.

State of Charge (SOC)

Pair interactions are a major cause for the changes in the stress development in the cathode material. During insertion and extraction (electrochemical cycling) of the lithium ions, the number of Li^+, Mn^{3+} and Mn^{4+} in the material changes,

affecting the interactions between these ions. These variations in the pair interaction in turn affect the mechanical properties of the cathode material[40]. Put differently, the elastic properties of the $Li_xMn_2O_4$ cathode material vary with the state of charge. To study this, uni-axial deformation in x-direction has been performed by applying 0.5% of strain at C/2 discharge rate.

Figure 2.7 shows the stress-strain curve for different SOC values. As seen in this figure, there is a strong relationship between SOC and the stress-strain behavior of the material. Initially, the relationship is almost linear, indicating an elastic behavior.

In case of $LiMn_2O_4$, the stress curve exhibits non-linearity after a strain of approximately 0.1, reaching the maximum stress of approximately 22 GPa at a strain of around 0.275. After attaining this peak, the stress values decreased sharply, indicating an initiation of fracture. A comparison of the stress-strain curves at different SOC values shows that as the amount of Li decreases, the peak stress values decline. This is because of the change in the lattice structure for different SOC values.

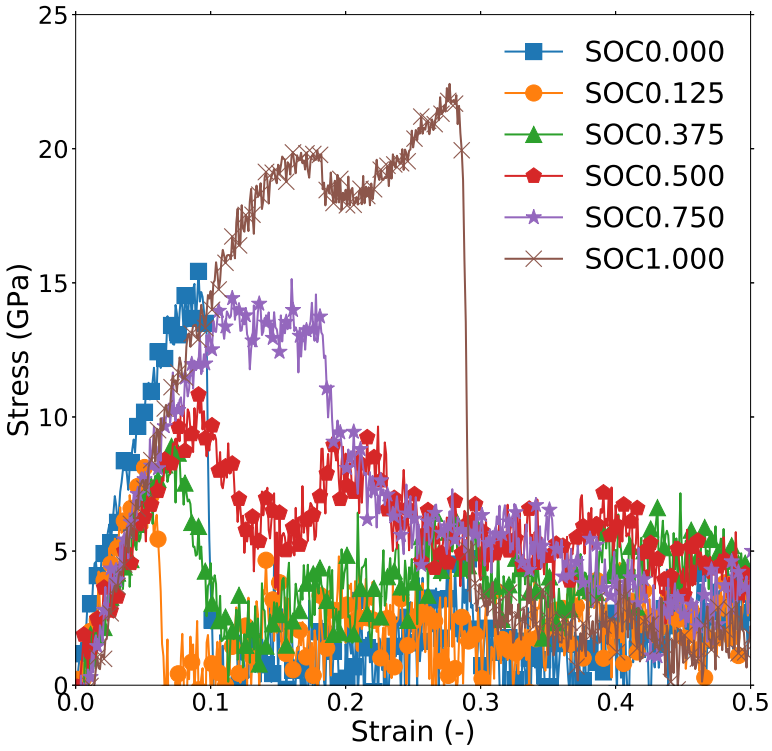

Figure 2.7: Stress-strain curve for each SOC value at 0.01/ps strain rate.

Unlike $LiMn_2O_4$, in $Li_{0.375}Mn_2O_4$, $Li_{0.5}Mn_2O_4$ and $Li_{0.75}Mn_2O_4$, after reaching the peak values, the stress does not drop immediately. Instead, we observe a large fluctuation. During the first decrease of the curve, amorphization due to atomic slip spread out from the hole in the horizontal direction. During the second decrease of the curve, void nucleation and growth were observed inside of the amorphous region. These plastic behaviors are more pronounced at lower concentration of Li.

From Figure 2.7 it is not difficult to conclude that the yield and ultimate stress values will vary with SOC values, yield stress being the point after which plastic deformation starts, and ultimate stress being the maximum stress value in the stress-strain curve. It can also be seen that in the early stages of charging (higher SOC values), the material shows a more ductile behavior whereas towards the end of the charging stage (lower SOC) it becomes more brittle, with the plastic behavior disappearing almost entirely. For SOC values in the range of 0 to 0.375, the initial stress values rise quite rapidly. This can be attributed to the presence of more than one phase in this range of SOC values, as has been reported in the literature [11].

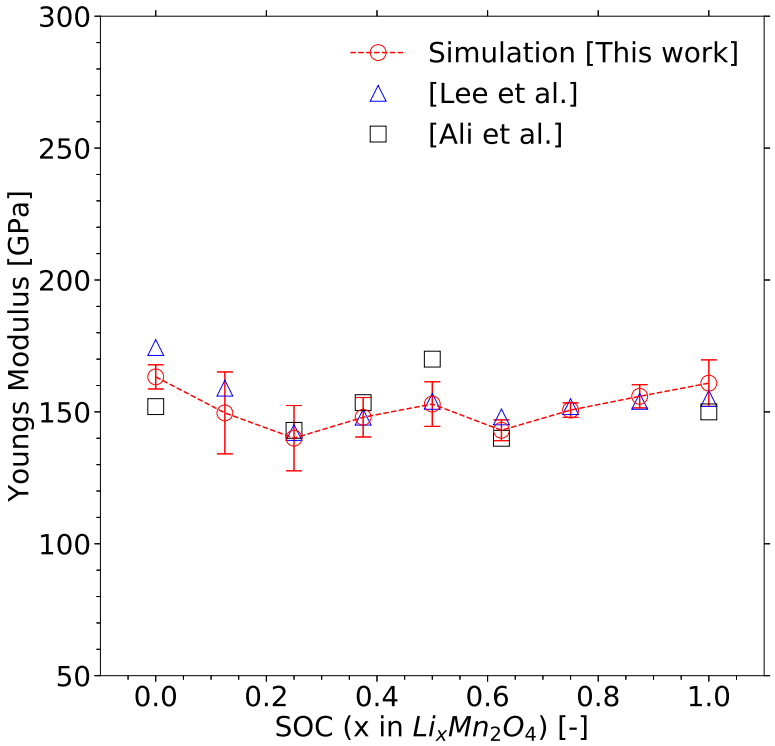

Figure 2.8: Young's modulus for various state of charges.

As a further validation of our results, in this work, the Young's modulus at various SOC values has been calculated using Equation 2.5, and following the averaging approach suggested by Lee et al.[40]. As can be seen in Figure 2.8, there is a good agreement with the data reported in the literature[40, 41]. Young's modulus value decreases from $x = 0$ to $x = 0.250$, varying from 163 GPa to 140 GPa. Further, it increases from $x = 0.375$ to $x = 1$, varying from 147 GPa to 160GPa.

The variation in the Young's modulus can be explained as follows: The mechanical properties of $LiMn_2O_4$ could be affected by three terms: the kinetic energy contribution, the long-range Coulombic interactions and the pair interactions. The kinetic energy contribution and long-range Coulombic interactions do

not change during the electrochemical charge cycle, and therefore do not have any effect on the mechanical properties. Pair interactions are the only responsible phenomenon for the changes in the mechanical properties during electrochemical cycling. There are 10 types of pair-interactions in the $LiMn_2O_4$ system: Li^+–Li^+, Li^+–Mn^{3+}, Li^+–Mn^{4+}, Li^+–O^{2-}, Mn^{3+}–Mn^{3+}, Mn^{3+}–Mn^{4+}, Mn^{3+}–O^{2-}, Mn^{4+}–Mn^{4+}, Mn^{4+}–O^{2-} and O^{2-}–O^{2-}. During charging and discharging process, numbers of these ions and their interactions change, affecting the mechanical properties, including the Young's modulus. This is is consistent with the propositions of Lee et al.[40].

Strain rate

In studying the mechanical properties of the $Li_xMn_2O_4$, it is important to understand the development of stress inside the material at different charging or discharging rates (C-rate). To this end, in this work, MD simulations for three different strain rates (0.001/ps, 0.01/ps and 0.1/ps) at two different SOC values (1 and 0.5) have been performed. These strain rates correspond to C-rates of 0.5C, 5C and 50C, respectively. The stress-strain curves for these simulations are shown in Figure 2.9 for SOC = 1, and Figure 2.10 for SOC = 0.5.

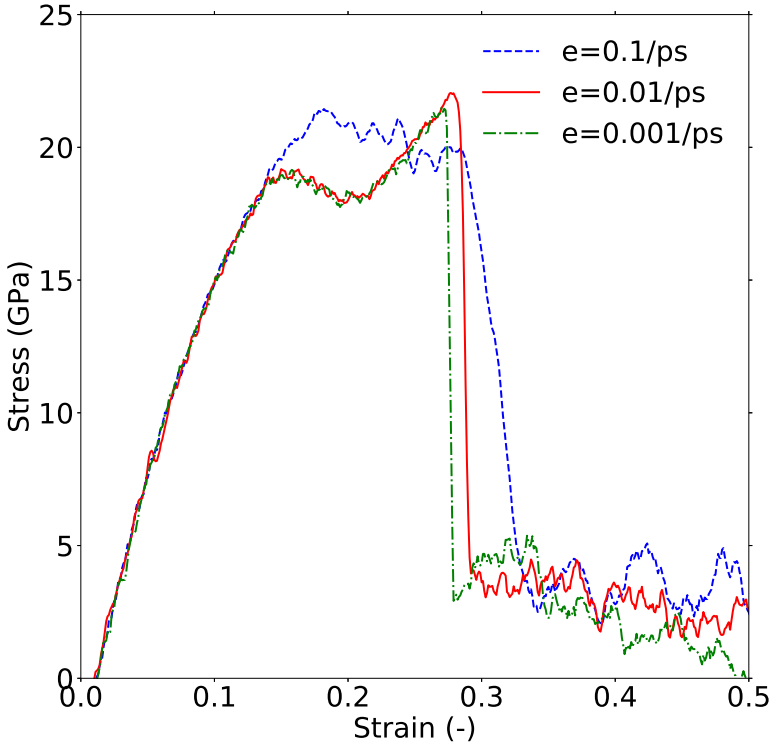

Figure 2.9: Stress-strain curve for different strain rates at SOC = 1.

As seen in Figure 2.9, the strain-rate seems have a negligible effect on the elastic properties of the material, at least for $LiMn_2O_4$ (SOC=1). It has also been observed in the Woodford et al.[42] work.

On the other hand, the trend is different when SOC = 0.5 (c.f. Figure 2.10). In this partially charged case, the yield stress and the ultimate stress increase by 70% as we go from a strain rate of 0.1/ps to 0.001/ps. This is a clear indicator that the elastic properties like Young's modulus changes with the strain rate. This change in the elastic properties can be attributed to the pair interaction response to different strain-rates, that determines the mechanical properties.

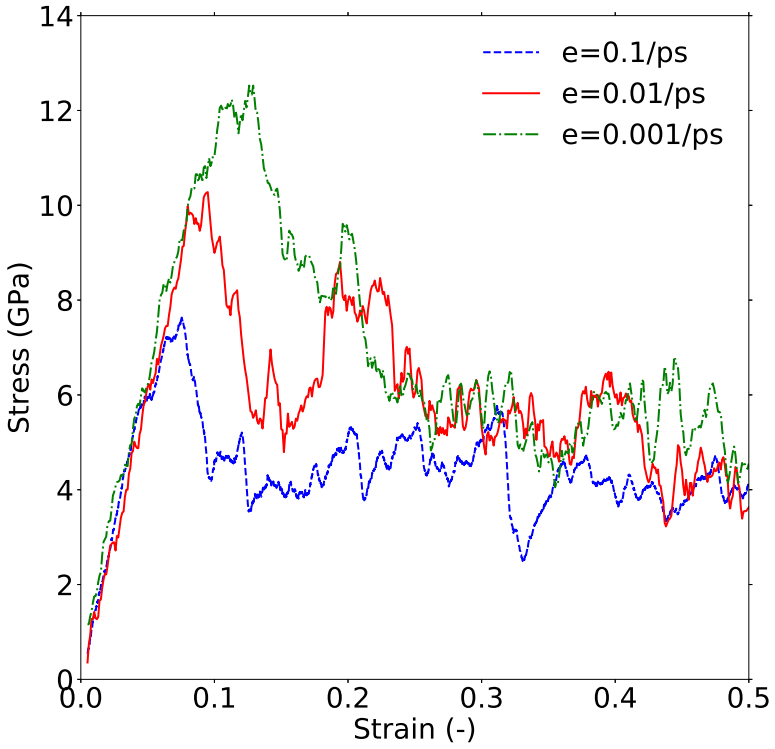

Figure 2.10: Stress-strain curve for different strain rates at SOC=0.5.

Temperature

Diffusion property has a significant influence on the performance of Li-ion batteries. However, most of the investigations in the literature have been restricted to the measurement of the lithium ion diffusion coefficient experimentally due to the very light nature of the element, and lack of a widely accepted radioisotope for lithium ion [43]. Additionally, there is a lack of experimental and theoretical consensus on the effect of stoichiometry on the diffusion properties during the charging and discharging processes when there are considerable variations in the lithium vacancy concentration. In this subsection, we investigate the diffusion of lithium in spinel $Li_xMn_2O_4$ phases through MD simulations. MD simulations are carried out over a temperature range of 300K-3000K. Each simulation is for a duration of 20ps during equilibration, and another 2ns for the analysis of the ionic displacement.

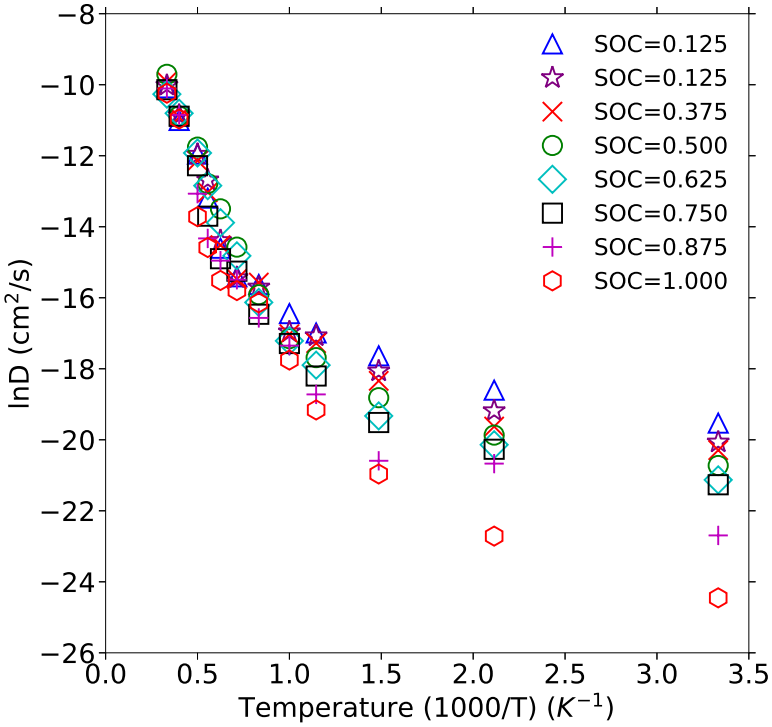

Figure 2.11: Diffusion with temperature for each SOC values.

Figure 2.11 shows the variation in the diffusion coefficient as a function of temperature, capturing the magnitude of the Li-ion diffusion inside the cathode material with variation in temperature. The trend in this figure is consistent with the findings in the literature[44].

As seen in this figure, in the high temperature zone (T>823K), the diffusion coefficients are quite close across all SOC values. However, in the low temperature zone (473K<T<823K), at lower SOC values the diffusion coefficient is much higher than the diffusion coefficients at the SOC value closer to stoichiometry. This can be explained by the fact that at lower SOC values, the number of vacant sites are higher, reducing the energy barrier for the ions to diffuce. In general, the diffusion coefficient for a fully discharged and charged state at 300K will vary from 7×10^{-11} cm^2/s to 3×10^{-9} cm^2/s.

In this work, we consider following theories to explain the trends in the above plot.

Arrhenius behavior: The temperature dependence of lithium ion diffusion coefficient can be modeled by the following Arrhenius equation:

$$D_{Li} = Aexp\left(-\frac{E_a}{K_B T}\right), \tag{2.10}$$

where A, E_a and k_B are pre-exponential factor, activation energy and Boltzmann constant, respectively. It can be seen from Equation 3.14 that the diffusivity of the ions can increase with an increase in temperature or when the activation energy is lower.

Assuming constant values for the pre-exponential factor and the activation energy in Equation 3.14, we will obtain a linear relationship between lnD and 1000/T. In doing so, following the proposition of Kuwata et al.[18], if we split the temperature region into a high temperature zone (T> 823K) and a low temperature zone (473K<T<823K), we can observe two distinct slopes corresponding to the different activation energies in Figure 11. This could be an indicator that the MD simulations are able to capture the vacancy diffusion mechanism in the near stoichiometric material[45].

According to vacancy diffusion mechanism, for an ion to diffuse without an available vacant site, total required activation energy will be the sum of vacancy formation and migration energy. This total activation energy can be written as:

$$E_a = E_a^{VF} + E_a^{VM}, \tag{2.11}$$

where, E_a^{VF} and E_a^{VM} are activation energies for vacancy formation and migration, respectively. Total activation energy can be calculated using Equation 2.11. In the stoichiometric $LiMn_2O_4$, all the Lithium (8a) sites are occupied, and therefore, a small number of Li vacancies govern the lithium ion diffusion.

As per the vacancy diffusion theory, it can be divided into two regions, high temperature intrinsic and low temperature extrinsic. Kuwata et al.[18] have prescribed the enthalpy of vacancy formation and migration energy for ionic diffusion as 0.6eV and 0.5eV, respectively. At high temperature intrinsic region, total activation for vacancy formation and migration can be obtained so that Lithium ion can easily diffuse. However, in the low temperature extrinsic region, to calculate diffusion coefficient, a vacancy has been created by extracting a lithium ion from the system. Hence, only migration energy would be required to start the diffusion. Therefore, the total activation energy in the Arrhenius equation will be reduced to only migration energy along with a new pre-exponential factor.

As seen in the Figure 2.12, based on our data, the vacancy formation and migration energy is approximately 0.59eV and 0.42eV respectively. In other words, the results from the MD simulations of this work follow a similar trend with experimental results. However, the required migration energy is somewhat under-predicted and this could be due to the fact that we have used optimum structure configuration where ions might have different migration paths.

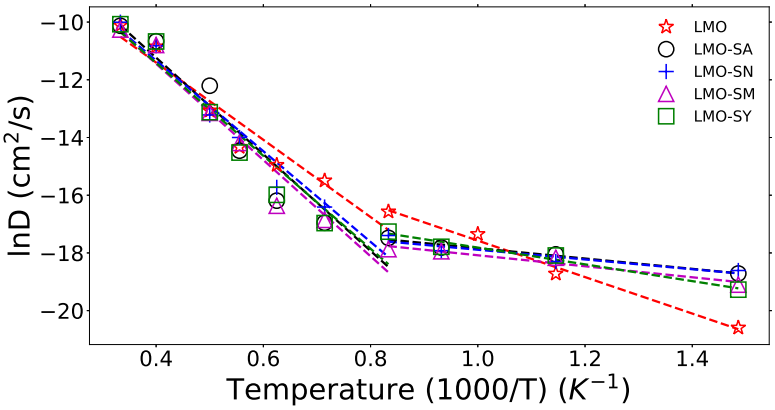

FIGURE 2.12: Arrhenius trend for the variation of diffusion coefficient with temperature at SOC=1.

Enhanced-Arrhenius behavior: While the above Arrhenius behavior explains the trends in in the molecular dynamics data to a large extent, from Figure 2.11, it is clear that the data is not completely linear. At higher temperatures, especially near the transition zone, activation energy along with pre-exponential factor can change with temperature. Hence it would not be ideal to assume that activation energy is independent of temperature[46].

The disagreements of the diffusion coefficients with Arrhenius trend through the entire range of temperature considered in this work could be attributed to the variations in the activation energy and pre-exponential factor with temperature. To accommodate this variation, we assume a linear variation of activation energy as well as the pre-exponential factor in the range [0.3eV, 1.7eV] and [1×10^{-7} cm^2/s, 0.025 cm^2/s], respectively. The extreme values in these ranges are similar to the values proposed by Kuwata et al.[18]. Specifically, we propose the following linear equations for A and E_a:

$$A = A_0 + \Delta A \frac{T - T_0}{T_{high} - T_{low}}, \tag{2.12}$$

$$E_a = E_{a0} + \Delta E_a \frac{T - T_0}{T_{high} - T_{low}}. \tag{2.13}$$

In the above equations, T_{high} and T_{low} are highest and lowest temperature point of the particular fitted curve line. A_0, E_{a0} and T_0 are reference pre-exponential factor, activation energy and temperature respectively. Table 2.3 shows the values of constants for both fitted curve lines:

Table 2.3: Values of the parameters in Equations 2.12 and 2.13.

Curve zone	A_0 (cm^2/s)	E_{a0} (eV)	T_0 (K)	T_{high} (K)	T_{low} (K)	Δ A (cm^2/s)	ΔE_a (eV)
High Temperature	0.005	1.01	823	3000	823	0.02	0.69
Low Temperature	1e-6	0.42	823	823	323	9e-6	0.12

Volmer-Fulcher-Tammann hypothesis: In another study by Bauer et al.[47], while investigating the molecular dynamics near the transition temperature, the authors found that there are deviations from the Arrhenius law.

We believe that the trends found by them, although for a different application, are probably relevant in this work for higher temperature zones. More precisely, we can observe that the trends in Figure 2.11 seem to follow the Volmer-Fulcher-Tammann (VFT) hypothesis[48]. In this theory, the diffusion coefficient below and above a certain transition temperature can be represented as[49]:

$$D_{Li} = Aexp\left(-\frac{B}{(T - T_{VFT})}\right), \tag{2.14}$$

where A, B and T_{VFT} are fitting parameters denoted as pre-factor, VFT-activation energy and VFT-temperature, respectively. According to VFT hypothesis, the non-Arrhenius behavior of diffusivity is observed in the under-cooled state[50, 51, 52, 53]. During supercooling, a rapid increase of the high energetic favorable local clusters can cause less mobility of the ions[54].

As seen in Figure 2.13, the fitted curve is in good agreement with the simulation generated data points except temperature between 1200K-2000K.

Thus, the hypothesis suggests that pre-factor and VFT-activation energy are dependent on the temperature, similar to our observations in the enhanced-Arrhenius formulation. Additionally, the VFT-temperature (T_{VFT}) is also needed to calculate the diffusion coefficient. However, at this time, due to the lack of experimental data for this material at the molecular level, it would be difficult to validate this theory. Hence, understanding that the experimental validation is critical, a detailed study on the non-Arrhenius behavior of the diffusivity has not been performed in this work. However, our results clearly shows that it would be an interesting research to follow up in the future.

2.4 Conclusion

In order to understand the intercalation induced effect on mechanical properties of $Li_xMn_2O_4$ cathode material for Lithium ion batteries, a series of Molecular Dynamics simulations were performed. The computational tool was validated with respect to the experimental data by calculating the lattice parameter for the optimized $LiMn_2O_4$. It was found that during full discharging cycle, the lattice

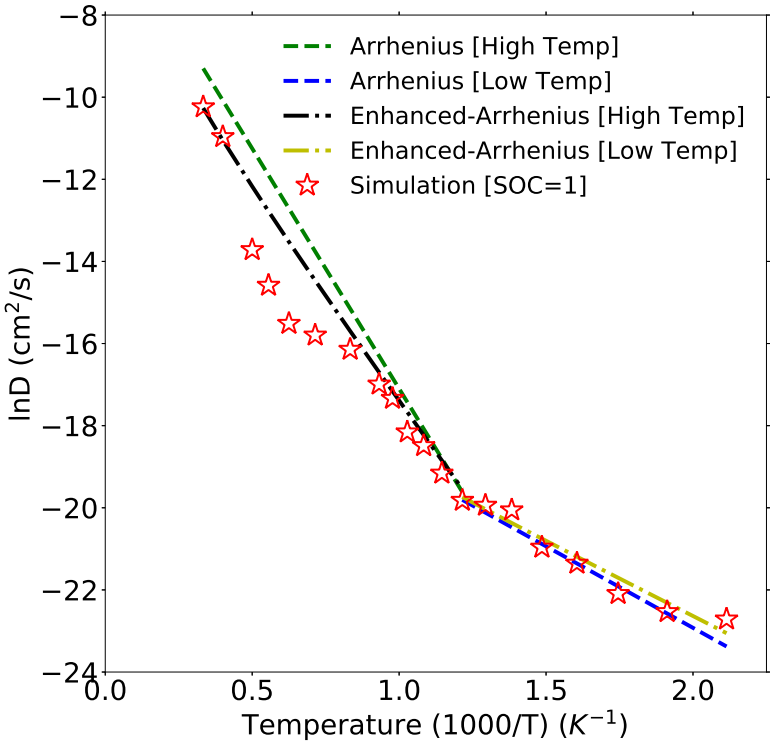

FIGURE 2.13: Arrhenius and enhanced-Arrhenius trends for the variation of the diffusion coefficient with temperature at SOC = 1.

constant varies from 8.042Å to 8.235Å which is in very good agreement with the experimental data. Total lattice and volume change during charging cycle were 2.34% and 6.87%, respectively, which is also in very good agreement with the experimental data.

The validated computational tool was used to conduct a parametric study on the effect of state of charge, strain rate, and temperature, on the performance of the battery. Results are validated with the experimental data available from the literature. It has been noticed that an increase in SOC values (Lithium content) cause higher ultimate stress that is due to less number of defects in the crystal structure. Further, Young's modulus for different SOC values, are consistent with literature. Stress-strain curve does not differ much for fully discharged state ($LiMn_2O_4$). However, higher strain strain-rate tends to initiate fracture mechanism earlier in the intermediate charging states. In general, the strain-rate simulations illustrate higher yield stress and ultimate stress for slower strain-rate, especially for intermediate SOC values. A study of the diffusion process found that at room temperature, diffusion coefficient increases by nearly 2 orders of magnitude from a fully charged state to a fully discharged state. Further, temperature dependency analysis suggests that diffusion coefficient follows the Arrhenius diffusion equation. The results are consistent with the theory on vacancy diffusion mechanism. Consistent with the propositions in the literature, accounting for a change in the activation energy in the two temperature zones enhances the accuracy of the model in capturing the diffusion processes more accurately. This also suggests that the diffusion coefficient at lower temperatures like 473K and 300K is higher than expected from just migration activation

energy extrapolation but is closure to the actual diffusion coefficient. To describe the trends in the diffusion coefficient more accurately, we also propose the enhanced-Arrhenius formalism in which a temperature dependent activation energy and pre-constant result in a better fit with the molecular dynamics data. We believe that this temperature dependence could also potentially be explained by the VFT theory.

References

[1] X. Hui, L. Zhentao, and Jianping X. "Nanostructured LiMn2O4 and their composites as high-performance cathodes for lithium-ion batteries". In: *Progress in Natural Science: Materials International* 22.572-584 (2012).

[2] E. Iguchi et al. "Electrical transport properties in LiMn2O4, Li0.95Mn2O4, and LiMn1.95B0.05O4 (B=Al or Ga) around room temperature". In: *Journal of Applied Physics* 91.2149 (2002).

[3] S. Y. Luchkin et al. "Li transport in fresh and aged LiMn2O4 cathodes via electrochemical strain microscopy". In: *Journal of Applied Physics* 118.072016 (2015).

[4] R. Sharma, N. Sharma, and M. Sharma. "LiMn2O4 spinel structure as cathode material for Li-ion batteries". In: *AIP Conference Proceedings* 2142.040024 (2019).

[5] H. Y. Amanieu et al. "Mechanical properties of commercial LixMn2O4 cathode under different State of Charge". In: *Acta Materialia* 89 (2015), pp. 153–162.

[6] J.M. Tarascon and M. Armand. "Issues and challenges facing rechargeable lithium batteries". In: *Nature* (2001).

[7] J. Cabana et al. "Enhanced high rate performance of LiMn2O4 spinel nanoparticles synthesized by a hard-template route". In: *J. Power Sources* (2007).

[8] C. Julien et al. *Lithium Batteries: Science and Technology*. Springer International Publishing, 2016.

[9] J.and Thomas K.E. Newman, H. Hafezi, and Wheeler D.R. "Modelling of Lithium-ion batteries". In: *J. Power Sources* 119 (2003), pp. 838–843.

[10] J. Christensen and J. Newman. "A Mathematical Model of Stress Generation and Fracture in Lithium Manganese Oxide". In: *J. Electrochem. Soc.* 153 (2006), A1019.

[11] W. H. Woodford, Y.-M. Chiang, and W. C. Carter. ""Electrochemical Shock" of Intercalation Electrodes: A Fracture Mechanics Analysis". In: *J. Electrochem. Soc.* (2010), A1052.

[12] Y. Hu, X. Zhao, and Z. Suo. ""Averting cracks caused by Insertion reaction In lithium-ion batteries". In: *J. Mater. Res., 2010* (2010).

[13] X. Zhang, W. Shyy, and A. M. Sastry. "Numerical Simulation of Intercalation-Induced Stress in Li-Ion Battery Electrode Particles". In: *J. Electrochem. Soc.* 154 (2007), A910.

[14] X. Zhang, A. M. Sastry, and W. Shyy. "Intercalation-Induced Stress and Heat Generation within Single Lithium-Ion Battery Cathode Particles". In: *J. Electrochem. Soc.* 155 (2008), A542.

[15] J. Christensen. "Modeling Diffusion-Induced Stress in Li-Ion Cells with Porous Electrodes". In: *J. Electrochem. Soc.* 157 (2010), A366.

[16] J. Park, W. Lu, and A. M. Sastry. "Numerical Simulation of Stress Evolution in Lithium Manganese Dioxide Particles due to coupled Phase Transition and Intercalation". In: *J. Electrochem. Soc.* 158.2 (2011), A201–A206.

[17] M. Y. Saidi, J. Barker, and Koksbang R. "Thermodynamic and Kinetic Investigation of Lithium Insertion in the Li1-xMn2O4 Spinel Phase". In: *JOURNAL OF SOLID STATE CHEMISTRY* 122 (1996), pp. 195–199.

[18] N. Kuwata et al. "Lithium diffusion coefficient in LiMn2O4 thin films measured by secondary ion mass spectrometry with ion-exchange method". In: *Solid State Ionics* 320 (2018), pp. 266–271.

[19] S. Takai et al. "Tracer diffusion coefficients of lithium ion in LiMn2O4 measured by neutron radiography". In: *Solid State Ionics* 256 (2014), p. 93.

[20] B. V. Merinov et al. "Li-diffusion at the interface between Li-metal and [Pyr14][TFSI]-ionic liquid: Ab initio molecular dynamics simulations". In: *J. Chem. Phys.* 152 031101 (2020).

[21] C. A. Brackley, A. N. Morozov, and D. Marenduzzo. "Models for twistable elastic polymers in Brownian dynamics, and their implementation for LAMMPS". In: *J. Chem. Phys.* 140 135103 (2014).

[22] J. C. Tully. "Molecular dynamics with electronic transitions". In: *J. Chem. Phys.* 93 1060 (1990).

[23] Y. Ida. "Interionic repulsive force and compressibility of ions". In: *Phys. Earth Planet.* (1976).

[24] K. Suzuki et al. "Structural properties of LixMn2O4 as investigated by molecular dynamics and density functional theory". In: *Japanese J. Appl. Physics, Part 1 Regul. Pap. Short Notes Rev. Pap.* (2000).

[25] K.E. Sickafus, J.M. Wills, and N.W. Grimes. "Structure of Spinel". In: *J. Am. Ceram. Soc.* (2004).

[26] S Plimpton. "Fast Parallel Algorithms for Short-Range Molecular Dynamics". In: *J. Comp. Phys.* 117 (1995), p. 1.

[27] R.T. Cygan, H.R. Westrich, and D.H. Doughty. "Ionic modeling of lithium manganese spinel materials for use in rechargeable batteries". In: *Mater. Res. Soc. Proc* 393 (1995), p. 113.

[28] G. V. Lewis and C. R. A. Catlow. "Potential models for ionic oxides". In: *J. Phys. C: Solid State Phys* 18 (1985), p. 1149.

[29] P. P. Ewald. "The calculation of optical and electrostatic grid potential". In: *Ann. Phys. (Leipzig)* 64.253 (1921).

[30] S. Nose. "A unified formulation of the constant temperature molecular dynamics methods". In: *J. Chem. Phys.* 81 (1984), pp. 511–519.

[31] A.K. Subramaniyan and C.T. Sun. "Continuum interpretation of virial stress in molecular simulations". In: *Int. J. Solids Struct.* (2008).

[32] A. Adan, C. T. Sun, and H. Mahfuz. "A molecular dynamics simulation study to investigate the effect of filler size on elastic properties of polymer nanocomposites". In: *Composite Science and Technology* 67 (2007), pp. 348–356.

[33] A. Grenall. "Isothermal Compositional Order-Disorder. I. Superstructure Solid Solutions in a Salt System". In: *J. Chem. Phys.* 17.1036 (2004), p. 1949.

[34] R. E. Garcia et al. "Microstructural Modeling and Design of Rechargeable Lithium-Ion Batteries". In: *J. Electrochem. Soc.* 152.1 (2005), A255–A263.

[35] T. Ohzuku, M. Kitagawa, and T. Hirai. "Electrochemistry of Manganese Dioxide in Lithium Nonaqueous Cell: III. X-Ray Diffractional Study on the Reduction of Spinel-Related Manganese Dioxide". In: *J. Electrochem. Soc.* (1990).

[36] M.M. Thackeray et al. "Lithium insertion into manganese spinels". In: *Mater. Res. Bull.* (1983).

[37] M.D. Chung et al. "Implementing Realistic Geometry and Measured Diffusion Coefficients into Single Particle Electrode Modeling Based on Experiments with Single LiMn2O4 Spinel Particles". In: *J. Electrochem. Soc.* 158.4 (2011).

[38] E. V. Vakarin, G. G. Belmonte, and J. P. Badiali. "Interplay of host volume variations and internal distortions in the course of intercalation into disordered matrices". In: *J. Chem. Phys.* 126.234709 (2007).

[39] N. H. Nachtrieb, E. Catalano, and J. A. Weil. "Self-Diffusion in Solid Sodium. I". In: *J. Chem. Phys.* 20.1185 (2004), p. 1952.

[40] S. Lee et al. "Molecular Dynamics Simulations of SOC-Dependent Elasticity of LixMn2O4 Spinels in Li-Ion Batteries". In: *J. Electrochem. Soc.* 160.6 (2013), A968–A972.

[41] A. Asadi, S. Aghamiri, and M. Talaie. "Molecular dynamics simulation of a LixMn2O4 spinel cathode material in Li-ion batteries". In: *RSC Advances* (2016).

[42] W.H. Woodford, Y.M. Chiang, and W.C. Carter. "Electrochemical Shock in Ion-Intercalation Materials with Limited Solid-Solubility". In: *J. Electrochem. Soc.* 160 (2013), A1286–A1292.

[43] N. Kuwata et al. "Lithium diffusion coefficient in amorphous lithium phosphate thin films measured by secondary ion mass spectroscopy with isotope exchange methods". In: *Solid State Ionics* 294 (2016), pp. 59–66.

[44] U. Kumar et al. "A Study of Transport Properties and Stress Analysis Using Atomistic and Macro Simulations for Lithium-ion Batteries". In: *J. Electrochem. Soc.* (2014).

[45] K. Hoang. "Understanding the electronic and ionic conduction and lithium over-stoichiometry in LiMn2O4 spinel". In: *J. Mater. Chem.* A.2 (2014), p. 18271.

[46] A. P. Zeke, O. M. Oluwaseun, and H. T. Ward. "Activation Energies and Beyond". In: *J. Phys. Chem.* 123 (2019), pp. 7185–7194.

[47] T. Bauer, P. Lunkenheimer, and A. Loidl. "Cooperativity and the Freezing of Molecular Motion at the Glass Transition". In: *Physical Review Letters* 111.22 (2013).

[48] Pablo G. Debenedetti. *Metastable Liquids: Concepts and Principles*. Princeton University Press, 1996.

[49] R. S. Smith and B. D. Kay. "The existence of supercooled liquid water at 150 K". In: *Nature* 398 (1999), pp. 788–791.

[50] D. Cangialosi, A. Angel, and J. Colmenero. "On the temperature dependence of the nonexponentiality in glass-forming liquids". In: *J. Chem. Phys.* 130.124902 (2009).

[51] C. A. Angell. "Formation of Glasses from Liquids and Biopolymers". In: *Science* 267.5206 (1995), pp. 1924–1935.

[52] F. Faupel et al. "Diffusion in metallic glasses and supercooled melts". In: *Rev. Mod. Phys.* 75.237 (2003).

[53] A. Pasturel et al. "Structural and dynamic evolution in liquid Au-Si eutectic alloy by ab initio molecular dynamics". In: *Phys Rev B* 81.140202 (2010).

[54] R. Trivedi, P. Magnin, and W. Kurz. "Theory of Eutectic Growth under Rapid Solidification Conditions". In: *Acta Metall Mater* 35 (1987), pp. 971–980.

Chapter 3

Doping and Co-doping Material selection and Multi-Scale modeling

PRELUDE: This chapter is been re-produced from the following manuscript with the permission of Wiley Publishing

R. Tyagi, A. Lanjan and S. Srinivasan, "Co-Doping Strategies to improve the Electrochemical Properties of $Li_xMn_2O_4$ Cathodes for Li-Ion Batteries", ChemElectroChem, 2021, 24, 101-125.

Contributing Authors:

- Ramavtar Tyagi - Setting up computational tools, performing all simulations, data collection, data analysis, and manuscript preparation.
- Amirmasoud Lanjan - Introduced to quantum mechanics calculations.

Abstract

Four novel cathode electrode materials with improved material properties have been derived from the Lithium Manganese Oxide spinel using co-doping strategies. Specifically, Aluminum, Nickel, Magnesium, and Yttrium were selected as the primary dopant to replace a fraction of Mn^{3+} (5%), and S^{2-} was selected as the secondary dopant to replace 1% of O^{2-}. A combination of quantum mechanics and molecular dynamics was used to study the fracture mechanics of the new materials for various State of Charge values, and improved performance is validated with experimental data. The results show that lattice constant values for all the doped structures decrease by 1.87%-2.07%. Overall, with co-doping, the diffusion properties improved, and activation energy required for Li^{+} vacancy migration reduced (0.21-0.25eV). We conclude that with reduced inter-atomic distance, the overall life of the LMO spinel can be improved. The Computational Fluid Dynamics simulations to study the macro-scale behaviour of these new materials shows a reduction in intercalation induced stress and heat generation.

3.1 Background

Lithium-ion batteries are very attractive solution for energy storage in the portable consumer electronic applications, hybrid and battery operated electric motor vehicles. This is made possible because of better theoretical and practical energy densities of lithium-ion batteries [1]. The electrodes play a key role in determining the discharge capacity or the amount of energy a battery can store. Since the anode is required to have as low potential voltage as possible to maintain the higher voltage difference with cathode, very limited options

are available for anode materials. In fact, graphite/silicon and more recently Lithium Titanate Oxide (LTO) have also been used as the anode material. On the other hand, for the cathode material, there are many potential candidates and several have been investigated by other researchers for specific applications [2, 3, 4, 5, 6].

In the last couple of decades, using Lithium Manganese Oxide ($LiMn_2O_4$) or simply LMO spinel as a cathode material for lithium-ion batteries has received considerable attention [7, 8, 9, 10, 11]. Generally, $LiMn_2O_4$ is favoured as a cathode material over other potential cathode materials such as Lithium Nickel Oxide ($LiNiO_2$), Lithium-titanate (Li_2TiO_3) and Lithium Cobalt Oxide ($LiCoO_2$) due to its lower cost and toxicity. Further, compared to Lithium Iron Phosphate ($LiFePO_4$), LMO spinel offers high operating voltage, higher energy density and better ionic conductivity. material [12, 13].

However, it has not been as popular as $LiCoO_2$ and other doped and co-doped derivation of $LiCoO_2$ such as Nickel Cobalt Mangenese (NMC) Oxide ($LiNi_xMn_yCo_zO_2$) and Nickel Cobalt Aluminium (NCA) Oxide ($LiNi_xCo_yAl_zO_2$), for high energy density applications such as Battery Electric Vehicles (BEVs). This is mainly due to the overall lower energy density and the lower cycle life due to cathode degradation [12, 13]. As it goes through a comparatively larger expansion and contraction processes during lithium-ion intercalation and deintercalation, respectively. The more pronounced expansion and contraction processes generate stress in the material, which can initiate fractures due to repeated charge and discharge cycles. This is an important cathode degradation mechanism in the lithium-ion batteries [14, 15, 16, 17, 18, 19, 20]. Further, as

described by Christensen et. al. [21], the stress generated in the active material due to intercalation process has a direct relationship with the concentration of lithium present in the electrode. This is due to the fact that the amount of lithium content in the host material, such as Mn_2O_4, determines the percentage of the Mn^{3+} and Mn^{4+} ions in the crystal since the addition of a Li^+ ion converts a Mn^{4+} to Mn^{3+} to balance the charge. Since the ionic radius of the Mn^{3+} is larger compared to Mn^{4+}, it results in a higher lattice expansion upon intercalation of every lithium-ion. Further, Mn^{3+} is also responsible for dissolving Manganese in the electrolyte as it forms Mn_2O_3, quickly degrading the cathode material [22]. There have been several research works focused on improving the cathode material's specific capacity either by coating the electrode or doping it with other lighter or higher ionic elements [23, 24, 25, 26, 27, 28, 29]. However, there is very limited experimental research focused on improving the $LiMn_2O_4$'s life since it is not easy to test every doping element for every possible composition. While extensive macro level numerical modeling has been undertaken in the literature to study the fundamental electrical and mechanical properties of Mn_2O_4 as an active cathode material, input parameters used for these simulations vary widely due to inconsistency in the experimental measurements, especially for partially charged states [16, 17, 20, 30]. Molecular and atomistic simulations can help overcome this inconsistency in the input parameter values and can help determine accurate input properties for the macro-scale simulations, enabling us to evaluate various lithiated structures more precisely.

The migration of lithium-ions in the electrolyte and especially within the electrodes governs the quality of charging and discharging processes within

an electrode material. Further, the propensity of the lithium ions to move within the cathode material is generally measured by the magnitude of the diffusion coefficient of lithium-ions inside the active particle. Often, the diffusion coefficient value used in the macro scale simulations is independent of the lithium content. In this chapter we will use more accurate values obtained from our MD simulations as explained in the Chapter 2 [31]. And these values will change based on battery's State of Charge (SOC) that changes the availability of the vacant lithium sites, varying the attractive and repulsive forces acting on the diffusing lithium-ions. Therefore, studying the movement of the lithium-ions at the atomistic scale and deriving the electro-mechanical properties of the doped and the undoped host material will enhance our understanding of the material behaviour. Further, as the temperature inside the cell rises, it increases the kinetic energy of the system which facilitates a faster diffusion rate. This is expected to increase the overall diffusion coefficient for these ions.

As established in the previous chapter, MD simulations are highly accurate in obtaining the material properties of the electrodes during the intermediate charging states. Therefore, in order to improve the material properties, elements that can be helpful will be studied in detail in this chapter. In addition to studying the impact of the four doping elements (Al, Mg, Ni and Y) on diffusivity, the effect of temperature on the diffusivity of lithium-ions at various SOC values of doped and undoped $Li_xMn_2O_4$ crystals has also been investigated. The findings emanating from this computational work will be useful to the battery research community since performing experiments at the molecular scale are not only very expensive but also continue to pose a great challenge in obtaining

precise results, especially for the variety of relevant doping scenarios investigated in this research. In fact, the challenge in performing precise experiments is also evident from the wide range of diffusion coefficients values at room temperature (10^{-8} - 10^{-15} cm^2s^{-1}) reported in the literature, all of which are obtained from a variety measuring techniques [32, 33, 34, 31]. This is not surprising because in addition to the limitation of the equipment used in these experiments, the transport and other properties strongly depend on the preparatory procedures that can influence the micro structure, defects, and atomic structure of the crystal.

In order to estimate the impact of doping elements, material properties like Young's modulus, diffusion coefficient, and the influence of the elevated temperature on various doped structures, has been studied in this chapter. In the Computational Tools and Analysis section (Section 3.2) the details of the quantum mechanics (QM), Molecular Dynamics (MD) simulation setup are described, which is more or less is similar to Section 2.2, and Computational Fluid Dynamics (CFD) simulation setup for macro scale modeling is also presented. Additionally, the theoretical background to calculate the mechanical properties such as Young's modulus and the diffusion coefficient is also described in this chapter. The selection criteria to pick the various doping elements have been outlined in Section 3.3. In the Results and Discussion section (Section 3.4), the effect of doping are explained and an experimental validation of the computational tool presented in this study with respect to data from various sources in the literature is included to establish the improvement in the material properties of $LiMn_2O_4$ with doping elements. Finally, in the Section 3.5, a summary of

findings are included and the major conclusions are drawn that provide the impetus for the work in the next chapter.

3.2 Computational Tools and Analysis

3.2.1 Quantum Mechanics Simulations

QM simulations were performed to verify the accuracy of the input parameters used in the MD simulations and to validate lattice structure of the doped cases where experimental validation is not possible. As shown in the Figure 3.1, the cubic spinel $LiMn_2O_4$ structure contains a total of 56 atoms in a unit cell: 8 lithium, 16 manganese and 32 oxygen atoms.

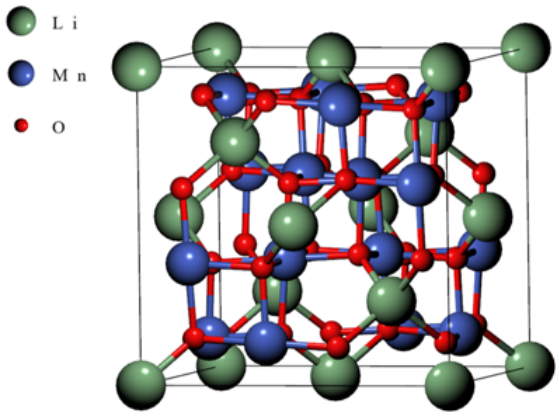

Figure 3.1: $LiMn_2O_4$ cubical spinel supercell for QM simulations.

QM calculations are performed on a single unit cell using the Density Functional (DFT) Theory along with Hubbard U model with the help of electronic structure investigation software, QUANTUM-ESPRESSO [35]. The cubical symmetry was applied to all point and space groups in all the simulations. Further, for lithium, manganese and Oxygen atoms, ultrasoft pseudopotentials (USPP)

based on the VANDERBILT code [36] were used, whereas pseudopotentials for other doped elements were Projector-Augmented Wave (PAW) type those uses "atomic" code from Corso [37]. Since the 3d electrons for most of the transition-metal atoms like Nickel, Manganese and other dopants might not be filled completely, spin-density approximation using the Perdew–Burke–Ernzerhof (PBE) form of the Generalized Gradient Approximation (σ-GGA) scheme [38, 39] has been used. To achieve better accuracy, the wave functions are stretched in the plane waves, with the cutoff energy of approximately 700eV, and the electronic charge density is elongated in a basis of cutoff energy of up to 6000eV. For lattice structure optimization calculations, the Brillouin zone integration was performed by using the $4 \times 4 \times 4$ Monkhorst–Pack k-points grid [40]. The geometry was optimized by relaxing the structure until the change in the maximum force on each atom reaches below 0.05GPa and variations in the stress values were also minimized. A convergence criterion for the total energy was set to 10^{-5}eV atom^{-1}. The Brillouin zone integration was applied with a Gaussian broadening of ~0.068eV. After geometry optimization calculations, the electronic structure and the electronic density of states were calculated with ($12 \times 12 \times 12$) Monkhorst–Pack k-point mesh [40].

3.2.2 Molecular Dynamics Simulations

As described in the section 2.2.1, Molecular Dynamics has been chosen to study the atomic scale multi-physics problems involved in the cathode material degradation mechanism. In order to gain appropriate information from the MD simulations, the inter-atomic potential function should be able to accomodate most of the physical and chemical phenomena, and experimentally validate it.

This is because a validated and genuine inter-atomic potential function would be able to reproduce various fundamental chemical and physical properties of the material such as Young's modulus, diffusion coefficient, activation energy etc. [41, 42, 43].

Inter-atomic pair interactions between different ions govern the potential energy which is responsible for the mobility of the ions, ultimately impacting the electrical and mechanical properties of the material. Gilbert-Ida-type [44] potential function has been used to evaluate the inter-atomic pair potential in our simulations which is presented in the Equation 2.1.

In the case of undoped structure, most of the potential function parameters are directly taken from Suzuki et al. [45] and are summarized in the Table 2.1.

A single cell of $Li_xMn_2O_4$ spinel consists of a total of 56 positions in a cubical structure in the Fd3m space group. In the crystal there are 8 lithium, 8 Mn^{3+}, 8 Mn^{4+}, and 32 oxygen ions. The ionic positions of these 56 ions are adopted from Sickafus et al. [46]. Further, for doping, depending upon the targeted doping percentages, a specific number of Mn^{3+} ions were replaced with the dopant ion in the super-cell.

As per Equation 2.1, the inter-atomic potential function depends upon the distance between the ions. Based on our previous work on $LiMn_2O_4$, as concluded from chapter 2, the value of the cutoff length was set to 10Å for all our MD calculations [31]. With this, knowing the length of a single unit cell as 8.24Å and recognizing the computational complexity involved in increasing the number of

cells in the calculations, as in Ref. [31], a supercell of $2 \times 2 \times 2$ unit cells in x, y and z-directions, has been used in this work (c.f. Figure 2.3)

All MD calculations were carried out using LAMMPS [47]. In order to estimate the inter-atomic interaction contribution, Gilbert-Ida-type potential function, as described in Equation 2.1, was used, and it was transformed into Buckingham potential which is available in LAMMPS [48, 49]. To calculate the long-range coulombic forces, the Ewald summation method has been applied [50]. A isothermal-isobaric ensemble (NPT) is used for the equilibration and production calculations, whereas a canonical ensemble (NVT) is used for the stress-strain calculations. Furthermore, in order to control the temperature of the crystal, Nose-Hoover thermostat has been implemented [51].

Following the strategy used in [31, 52, 53], simulations were carried out in two steps: First, an optimal crystal structure was achieved by simulating all initial configurations for one time step and from these we equilibrated four cases that had lowest potential energy. Second, when the setup is equilibrated, we ran the actual production simulations such as calculation of mean square displacement or stress generation with time. An average of the data from all four cases was then used as the overall output for that particular configuration. It must be noted that the number of configurations in which these ions can be arranged will depend upon the state of the charge of the battery since the number of lithium ions will vary, impacting the number of Mn^{3+} and Mn^{4+} as well. The variation in the Mn ions is because with changes in the number of lithium-ions, equivalent number of Mn^{4+} switch to Mn^{3+} to maintain the charge neutrality of the system.

As shown in Figure 2.3, all lithium-ions are located at the 8a tetrahedral sites, manganese (Mn^{3+} and Mn^{4+}) are positioned on 16d octahedral sites, and O^{2-} are placed at the 32e sites. Further, these ions could be arranged in numerous ways, resulting in many possible crystal configurations. For example, in a completely lithitated state, when all lithium-ions are intercalated in the host structure ($LiMn_2O_4$) for (SOC = 1), there are 12870 possible configurations. Similarly, replacing a Mn^{3+} ion with a doping element in a fully de-lithiated case will result in 102960 possible configurations (c.f. Table 3.1).

Table 3.1: Possible ionic configuration at each SOC for y=6.25% in $Li_xM_yMn_{2-x-y}O_4$.

State of Charge	# of lithium-ions	# of ways to arrange
0.000	0	16
0.125	1	128
0.250	2	6720
0.375	3	94080
0.500	4	509600
0.625	5	1223040
0.750	6	1345344
0.875	7	640640
1.000	8	102960

As summarized in Table 3.1, there are more than 3 million possible initial configurations that must be considered to obtain a crystal structure with the least potential energy. The number of possible crystal configurations is even higher with doping. Running equilibration simulations for all these combinations is time intensive and is not computationally feasible. Therefore, based on the strategy used in [31, 53, 52], we run LAMMPS simulation on the possible configurations for just one time step and then pick four configurations that have the lowest potential energy. However, with doping, the number of possible cases

are innumerable. As a result, performing even the one time step simulations for these millions of cases is not computationally feasible. Therefore, we sorted out the cases based on our findings from the $LiMn_2O_4$ simulations and performed the one time-step simulations for a total of 100,000 configurations for each state of charge. Subsequently, from these, four cases with least potential energy were selected for the equilibration and production calculations.

3.2.3 Calculation of Mechanical Properties

Young's modulus calculation:

In MD calculations, stress is mostly computed in the form of virial stress by applying gradual strain on the lattice boundary using the NVT ensemble. Equation 2.2, is being utilized to calculated the stress which is available in LAMMPS [54]. Since the stress in the system depends upon the stopping point of the equilibration simulation, to avoid fluctuations and to obtain a convergence, for each crystal configuration, stress calculations were made for the last 400 time steps as done for undoped cases. An average of these was used as the stress value for the specific crystal configuration. Young's modulus values were calculated from the virial stress output and further examined at the different state of charge. In order to quantify the Young's modulus, the relationship between the linear elastic stress and strain in the course of an uniaxial load are evaluated using the Equation 2.3[55].

Once we have the data for the above equation, the bulk modulus of elasticity, B, is computed using Equation 2.4. Finally, the Young's modulus, Y, is calculated

by substituting the values of Bulk modulus and, B and C_{11} from Equations 2.3 and 2.4 in the Equation 2.5

3.2.4 Diffusion Coefficient

With an elevation in the temperature, kinetic energy and thereby the total energy of the system increases. This increase in the energy enhances the movement of the ions within the system, i.e., increases the thermal diffusivity in the system. Additionally, as described in Equation 4.6, chemical diffusion coefficient is also relevant and will be influenced by the SOC, temperature, and the dopants. To be consistent with the literature, we use Equation 4.6, that includes the diffusion induced stress term, to calculate the diffusion coefficient at particle level. Further, the calculated values from this equation is also used to validate the results of our CFD simulations [19, 20, 52, 53].

In order to study the effect of the temperature on the various doped and undoped cases, several MD simulations were carried out at various temperature ranges, and the corresponding diffusion coefficients were evaluated using the change in the Mean Square Displacement (MSD) values of the lithium-ions with time. For this, the MSD values for lithium-ions were calculated using Equation 4.7. Further, in order to get the diffusion coefficient values from the MSD data, the Einstein equation 4.8 was used.

3.2.5 Macro-scale CFD modeling

An intercalation process inside the battery can be modeled as the transport of lithium-ions inside the host material by defining the diffusion flux at boundary

using rate of electrochemical reaction. The electrochemical potential difference between the electrodes or the current density are the major driving force in the movement of the lithium-ions inside the cell.

Lithium-ion transport equation: The intercalation based lithium diffusion in the electrode materials can be modeled by a governing equation for the transport of lithium-ions and the boundary conditions which are determined by the electrochemical kinetics. The porous solid phase of the cathode material in the lithium-ion batteries are made of solid active particles, and for the simulations purpose we have assumed spherical particle as the model domain. Therefore, the lithium-ion transport equation inside the cathode material can be given by [15]

$$\frac{\partial c}{\partial t} + \nabla \cdot J = 0, \tag{3.1}$$

where J is the diffusion flux and c is the concentration of lithium-ions. Further, to include the effects of the intercalation generated stress, the diffusion flux can be written as [19]

$$J = D_{Li^+}^{eff}(\nabla c - \frac{\Omega c}{RT}\nabla \sigma_h), \tag{3.2}$$

where ϵ_{ij}, σ_{ij} are the components of strain and stress, respectively, and Ω is the partial molar volume of the lithium. Further, $D_{Li^+}^{eff}$ is the effective diffusion coefficient for lithium-ion, σ_h is the hydrostatic stress, and R and T are general gas constant and temperature, respectively. Since the hydrostatic stress, σ_h, is a function of concentration, the transport of lithium-ions and the induced stress will be coupled. Therefore, the concentration equation for the coupled problem can be derived as suggested by Chu and Lee [56]. For a spherical

particle, Equation 3.2 can be written as

$$J = D_{Li^+}^{eff}\left(\frac{\partial c}{\partial r} - \frac{\Omega c}{RT}\frac{\partial \sigma_h}{\partial r}\right). \tag{3.3}$$

Using the chain rule, the term $\frac{\partial \sigma_h}{\partial r}$ in Equation 3.3 can be written as: $\frac{\partial \sigma_h}{\partial r} = \frac{\partial \sigma_h}{\partial c}\frac{\partial c}{\partial r}$, where the hydrostatic stress is given by

$$\sigma_h(r) = \frac{2\Omega Y}{9(1-\nu)}\left(\frac{3}{R^3}\int_0^R c(r)r^2 dr - c(r)\right). \tag{3.4}$$

The partial differentiation of hydrostatic stress with respect to concentration,

$$\frac{\partial \sigma_h}{\partial c} = -\frac{2\Omega Y}{9(1-\nu)}, \tag{3.5}$$

will provide the final stress coupled lithium flux equation

$$J = D_{Li^+}^{eff}\left(1 + \frac{2\Omega^2 YC}{9RT(1-\nu)}\right)\frac{\partial c}{\partial r}. \tag{3.6}$$

Boundary Conditions: For the boundary condition at the surface of the particle, the diffusion flux will be derived by the charge/discharge current density, i_n, as

$$J = D_{eff}\left(1 + \frac{2\Omega^2 YC}{9RT(1-\nu)}\right)\frac{\partial c}{\partial r} = \frac{i_n}{F}, \tag{3.7}$$

where i_n is the charge or discharge current density at the particle's surface which depends upon the rate of electrochemical reaction, and can be calculated using

the Butler-Volmer equation [57]

$$J = \frac{i_n}{F} = \frac{i_0}{F}\left[exp\left(\frac{(1-\beta)}{RT}F\eta\right) - exp\left(\frac{\beta}{RT}F\eta\right)\right], \tag{3.8}$$

where i_0 is the exchange current density, β is the symmetry factor, and $\eta = V - U$, represents the surface overpotential, with V being potential difference between electrodes, and U is the Open Circuit Voltage. The value of U is obtained by fitting the experimental data of LMO spinel from Doyle et al. [58] on the open circuit voltage as a function of the SOC [59]. Assuming uniform cathode particle size, the value of applied voltage, V, will be the potential difference between the electrodes, also obtained from their experimental data. Further, the exchange current density, i_0, can be calculated as

$$i_0 = Fkc_l^{1-\beta}(c_{max} - c_{surface})^{1-\beta}c_{surface}^{\beta}, \tag{3.9}$$

where k is the constant for reaction rate, c_l and $c_{surface}$ represent the lithium-ion concentration in the liquid phase (electrolyte) and at the surface of electrode, respectively.

Input parameters and Initial Conditions: Table 3.2 summarizes the values of all the parameters used for the CFD validation, as prescribed by Zhang et al. [60]. Further, input parameters such as the diffusion coefficient, the Young's modulus, and the partial molar volume will be different for the doped materials. These values have been obtained from the MD simulations of this work for the various SOCs. For the discharge cycle, at time $t = 0$, concentration of lithium-ion at the surface of the cathode particle will be almost maximum, i.e., $c_0 = 0.996c_{max}$.

Table 3.2: Parameters used in the CFD model. All parameters, are from Zhang et al. [60].

Symbol	Value	Unit
β	0.5	-
c_l	1000	mol m^{-3}
c_{max}	23700	mol m^{-3}
k	1.9×10^{-9}	$m^{5/2}s^{-1}mol^{-1/2}$
$D_{Li^+}^{eff}$	2.2×10^{-13}	m^2 s^{-1}
Y	10	GPa
Ω	$3.497 \times 10^{-}6$	mol m^{-3}
v	0.4	mV s^{-1}
r_0	5	μm

Stress generation model: In order to calculate the stress from applied strain on intercalation, we have used the following equation that uses the analogy of thermal stress:

$$\epsilon_{ij} = \frac{1}{Y}\Big[(1+\nu)\sigma_{ij} - \nu\sigma_{kk}\delta_{ij}\Big] + \frac{\widetilde{c}\Omega}{3}\delta_{ij}, \tag{3.10}$$

where $\widetilde{c} = c - c_0$ represents the change in lithium-ion concentration before and after intercalation. As per Equation 3.10, the generated strain will be influenced by the Young's modulus, the stress components, the partial molar volume and the change in the lithium-ion concentration. Therefore, in this work, we have used these properties as a function of SOC.

Heat generation model: Heat generation during charge and discharge cycle is an important phenomena in the lithium-ion batteries, which can be calculated as

$$\dot{Q}_g = I(V - U^{avg}) + IT\frac{\partial U^{avg}}{\partial T} + \sum_k \Delta H_k^{avg} r_k + \int \sum_j \sum_i (\overline{H}_{ij} - \overline{H}_{ij}^{avg}\frac{\partial c_{ij}}{\partial t} dv), \tag{3.11}$$

where the first term represents the irreversible resistance induced heating which is generated from the change in the cell potential with respect to its original equilibrium. The second and third terms are the heat generation due to reversible entropy, and the side chemical reactions, respectively. The third term, $\sum_k \Delta H_k^{avg}$, is the enthalpy of the side reaction, and r_k is the reaction rate for the reaction k. Assuming no side reactions are involved, this term will be neglected in this work. The fourth term in the above equation represents the heat generation because of mixing, as localized concentration (c_{ij}) of species i in phase j varies with time. dv, $\overline{H}_{ij}$ and $\overline{H}_{ij}^{avg}$ are the differential volume of the localized element, partial molar enthalpy and average partial molar enthalpy, respectively. The simplified version of the heat generation due to mixing can be written as [61]

$$\dot{Q_{mixing}} = \frac{\partial}{\partial t}\left[\frac{1}{2}\frac{\partial \overline{H}_s}{\partial c_s}\int (c_s - c_{s,\infty})^2 dv)\right], \tag{3.12}$$

where term $\frac{\partial \overline{H}_s}{\partial c_s}$ is the enthalpy potential over concentration, as described by Zhang et al. [20]. In Equations 3.11 and 3.12, $\frac{dU}{dT}$ and $\frac{dH}{dc}$ are obtained from the experimental data of the LMO spinel [62]. Since we have used a very small amount of doping, the change in the $\frac{dU}{dT}$ and $\frac{dH}{dc}$ curve will be very minimal. Therefore, in this research, we have used the experimental curve proposed in Ref. [62].

3.3 Materials: Selection of Doping Elements

There has been a lot of research on electrode materials that is focused on achieving higher specific capacity, better structural stability, and ability to function at

higher charge and discharge rates [63, 64]. Moreover, studies have been carried out to control the electrochemical potential dictated by the electronic structure and atomistic energy of the electrode materials [65]. In designing and evaluating novel electrode materials for the required energy density, cycling capability and structural stability, the cell voltage and the electrochemical potentials of both anode and cathode materials are important quality indicators.

Specifically, the anode and cathode materials must be selected in such a way that the electrochemical potential of the anode (μ_A) remains below the Lowest Unoccupied Molecular Orbital, and the electrochemical potential of the cathode (μ_C) is always above the Highest Occupied Molecular Orbital line. Without this, the electrolyte will start oxidizing on the cathode side or a reduction process will occur at the anode which can form unwanted solid electrolyte interphase (SEI) layer [66]. Besides the electrolyte's cell voltage window, the number of electrons in the p orbital of anions also determines the possible cathode voltage. Also, a large difference in electronegativity values between the cathode and anode materials is preferred to ensure condensed and stable structures. Finally, the variation in the Gibbs free energy, and the potential which can be offered by a particular electrode material strongly depend upon the ionic radius, oxidizing power, electronegativity, and the surrounding environment of these cations in the metal oxides.

It must be noted that the electrochemical properties of a material are dictated by its crystal, electronic and micro-structure, and they are generally decided by the original behaviour of the adopted material. Their molecular structures may differ widely due to different synthesis or processing methodologies and

environmental conditions. For example, if active ions are intercalated into the cathode material through a particular direction, it could expose the host structure's surface for easier lithium ion transfer, which can enhance the ionic movement and the charge/discharge rate capability [67]. Though the structure of the crystal is an intrinsic property of a particular material, it can still be modified by instituting relevant doping elements. For example, introduction of Ni^{2+} into V_2O_5 results in the simultaneous enhancement in the performance of the material since its structure is more stable during the cycling process, attaining a higher specific capacity. Introducing the dopant or co-dopants atoms can notably change the crystal field, which can help us fine-tune the electronic and mechanical structure of these materials which can also adjust the electrochemical potential values [68].

With these in mind, several benchmarks have been proposed in the literature to select the potential cathode materials. These are based on societal, financial feasibility, and practical consideration. These also include their natural abundance, eco-friendly processing characteristics, reusability, recycling capacity, and cost. From a technical point of view, the cathode materials should offer extensive reversible energy storage capabilities for the required voltage range. The theoretical discharge capacity of a cathode material represents the maximum possible energy storage capacity, and is given by

$$C_{th} = \frac{nF}{3.6 \times M}. \tag{3.13}$$

In the above equation, n is the number of active electrons for every mole or

formula unit, and M is the molar mass of electrode material [69]. The number of active electrons are directly related to the number of lithium-ions that can be accommodated in the host material's lattice structure. Thus, as per Equation 3.13, by using entities with smaller molecular mass that can accommodate more number of electrons per mole, we can obtain a better theoretical capacity. For example, the maximum theoretical capacity of $LiMn_2O_4$ is 148mAh/g since only one electron is released for every lithium-ion insertion into the vacant site of the host Mn_2O_4. On the other hand, if we compare this with V_2O_5, it offers a better theoretical energy storage capacity of ~440mAh/g because it can release 3 electrons for every active ion insertion into the host lattice [63]. Nevertheless, lighter and smaller elements are preferred as a cathode materials due to their higher gravimetric and volumetric specific capacities. Therefore, majority of the elements from first 4 rows of the periodic table could be a potential candidate for doping as long as they do not have restrictions based on the other selection criterion. Additionally, elements such as Zr, Mo, Ru etc. have also been used in some of the recent and more expansive cathode materials [70, 71]. A benefit of selecting transition metal oxides as a cathode material is that they offer changeable valence states that can easily accommodate more electrons.

Based on these criteria and recommendations, several bi- or trivalent cations, such as Al, Ni, Mg, Y, Cr, Ga etc. have been identified as good doping candidates that can partially substitute the Mn^{3+} in LMO spinel. In this research, we have explored the use of Al, Ni, Mg and Y as dopants. Among the proposed elements, Al has smallest ionic radius, forms stronger chemical bond with oxygen and is found in abundance [72]. Magnesium and Nickel offer changeable

valence state. Therefore, doping with them can also improve intercalation voltage. With a smaller ionic radius and low electronegativity, Mg, will form a smaller and stronger bond with oxygen as compared to Mn-O [73]. On the other hand, Yttrium is heavier and has a larger ionic radius. However, it has a low electronegativity and forms a stronger bond with the oxygen ion, improving the structural stability. Additionally, introduction of a small amount of sulfur in the LMO spinel structure can reduce the undesirable phase transition situation which occurs at around room temperature. Recent studies have established that doping with a transition metal can restrict the movement of the lithium ions. However, this can be overcome by replacing oxygen ions by Sulfur that will significantly improve the mechanical and electrochemical properties of the cathode materials for lithium-ion batteries [74, 75]. Therefore, in addition to introducing the dopant, we replaced 1% of the O^{2-} with S^{2-}, resulting in a crystal structure of $Li_xM_yMn_{2-x-y}O_{4-z}S_z$.

In order to completely understand the impact of each doping element, we have performed the following four sets of diffusion simulations: 1. A baseline simulation without any doping element. 2. A set of cases with the different doping elements (Al, Ni, Mg and Y). 3. A case with the addition of only sulfur as the doping element. 4. A set of cases with a doping element and using sulfur as the co-dopant. For the simplicity of the nomenclature, doped structures with just one of the elements, i.e., Al, Ni, Mg, Y and S, are called LMO-A, LMO-N, LMO-M, LMO-Y and LMO-S, respectively. Co-doped structures with a doping element (Al, Ni, Mg and Y) and sulfur as the co-dopant are labelled as LMO-SA, LMO-SN, LMO-SM, and LMO-SY, respectively. The undoped structure will be

referred to as LMO. Adding lighter elements like Al will also increase the overall discharge capacity. Therefore, as summarized in the Table 4.2, with minor doping by 1-2%, the overall discharge capacity, calculated using Equation 3.13, will still be comparable to that of $LiMn_2O_4$. Table 4.3 summarizes the potential parameters from the literature that has been used for the MD simulations in this work [76, 77, 78, 79, 80].

Table 3.3: Theoretical cell discharge capacity with different doping elements.

Structure	Theoretical discharge capacity (Ah/kg)
LMO	148
LMO-SA	149
LMO-SN	147
LMO-SM	149
LMO-SY	146

Table 3.4: The potential parameters of the different doping ions.

Doping element	Z	a(Å)	b(Å)	References
Al^{3+}	+1.4	0.530	0.050	[76, 78]
Ni^{2+}	+1.4	0.700	0.059	[79]
Mg^{2+}	+1.4	0.720	0.060	[78]
Y^{3+}	+1.4	0.900	0.068	[77]
S^{2-}	−1.2	1.840	0.075	[80]

3.4 Results and Discussion

To ensure the validity of the simulation results, the lattice parameter of the $Li_xMn_2O_4$ structure optimized at 300K was calculated by measuring the size of the equilibrated system for various SOC values, and the results were compared with the experimental data from the literature. In the doped cases, where experimental data is not available, we undertook a preliminary validation of

the lattice structure using Quantum Mechanics simulations, and then continued with the LAMMPS simulations.

3.4.1 Validation of the Computational Models

QM Simulations

The QM calculations were used to verify the accuracy of the input parameters used in the MD simulations. To ensure the accuracy of the QM calculations, we calculated the lattice constant for the LMO spinel and compared it with the measured values from the literature as well as our findings from LAMMPS results. More precisely, the lattice cell length of LMO was calculated as 8.254 Å and this is in excellent agreement with the experimental data of 8.247 Å with an error of 0.08% [81, 82]. In view of the fact that the experimental data on the lattice cell length for the new materials explored in this work do not exist, the QM calculations are used to support the MD results.

The MD Model

To validate the MD model, we compared the lattice length and diffusion coefficient for $Li_xMn_2O_4$ spinel with the experimental data as well as the QM simulation. As seen in the first row of Table 4.8, there is an excellent agreement between the MD calculations and the measured values as well as results from our QM calculations. More precisely, for LMO, the MD calculation is 0.15% higher than the experimental data, and 0.23% lower than the QM calculation. This accuracy clearly establishes the validity of the MD model. Since there is no experimental data for co-doped structures studied in this work, we have

compared the lattice structure length predicted by MD with the values from QM simulations (c.f. Table 4.8).

Table 3.5: Lattice cell length for undoped and doped materials.

				Deviation of MD with respect to:	
Structure	MD (Å)	QM (Å)	Experiment (Å)	Experiment (%)	QM (%)
LMO	8.235	8.254	8.247 [81, 82]	0.15	-0.23
LMO-SA	8.221	8.146	–	–	+0.92
LMO-SN	8.223	8.209	–	–	+0.17
LMO-SM	8.212	8.216	–	–	-0.05
LMO-SY	8.219	8.325	–	–	-1.27

As seen in Table 4.8, for each co-doped material, the lattice length predicted by MD and QM are in close agreement. The maximum deviation of 1.27% was calculated for the Sulfur-Yttrium co-doped structure. While the lattice length values calculated by MD simulations are higher than the values from the QM calculations in LMO-SA and LMO-SN, the MD simulations show a slight underprediction in LMO-SM and LMO-SY structures. Nevertheless, in all cases these small variations are due to the numerical fluctuations that is governed by the termination time of the equilibration simulations in MD, and can be considered statistically insignificant.

A further validation of our MD simulation tool is presented in Figure 3.2. As seen in this figure, for the fully lithiated LMO spinel, there is a good agreement between the diffusion coefficient values calculated from MD simulations and the experimental data of Takai et al. [34] and Kuwata et al. [33]. Specifically, the agreement is excellent for a temperature in the range of 573K-1000K.

At temperatures below 573K, the diffusion process is greatly subdued, requiring us to increase the simulation duration from 2ns to 5ns. Faced with the similar

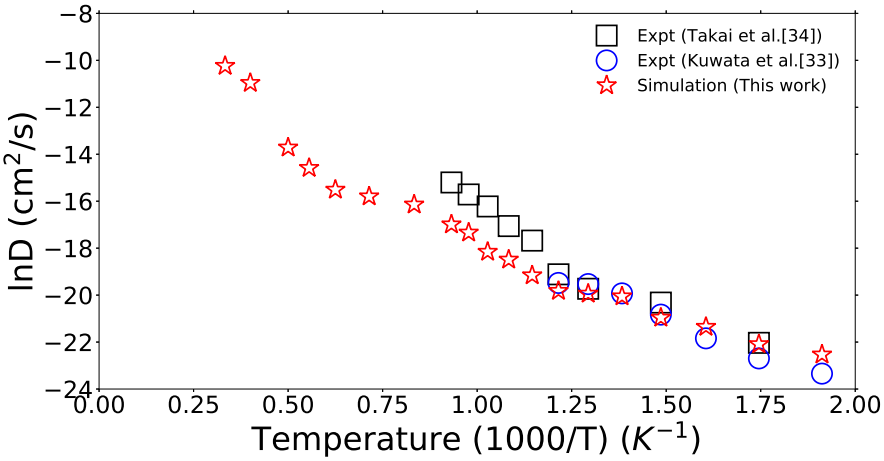

Figure 3.2: Lithium-ion diffusion coefficient compared with experimental results for SOC=1.

challenge, Kuwata et al. [33] extrapolated their experimental data to predict a diffusion coefficient of approximately 10^{-15} cm^2s^{-1} at room temperature. In their experiments, they used electrochemical ion-exchange and simple ion-exchange methodologies using different isotopes of the lithium. It must be noted that this is several orders of magnitude lower than the chemical diffusion coefficient that is approximately 10^{-12} cm^2s^{-1}. On the other hand, the MD simulations from this work estimate the diffusion coefficient as approximately 7.4×10^{-11} cm^2s^{-1}. This is within the range of the chemical diffusion coefficient data published by Chung et al. [83], instilling further confidence in our MD simulations.

The CFD Model

As described in Section 2.5, we have used the computational modeling framework suggested by Newman et al. [15], with input parameters as defined in Table 3.2. To validate our macro-scale model, we have compared the results from our simulations with the corresponding results from Zhang et al. [20] and

Clerici et al. [84]. Specifically, in Figure 3.3, we have shown the radial stress generated inside the active particle during the charge and discharge cycles. The first 2000 seconds in this figure represents the charging cycle when lithium ions are extracted from the cathode material (LMO). Hence, during this time, the radial stress reduces with time. The later half of the plot from 2000s to 4000s shows the stress generation as lithium concentration increases in the cathode particle. As seen in this figure, the results from our simulations are in excellent agreement with the findings of Zhang et al. [20]. The minor variations in the peaks in this figure are due to the number of data points selected for the presentation of the image. In the ensuing sections, we present the findings from employing the validated models to study the doped materials.

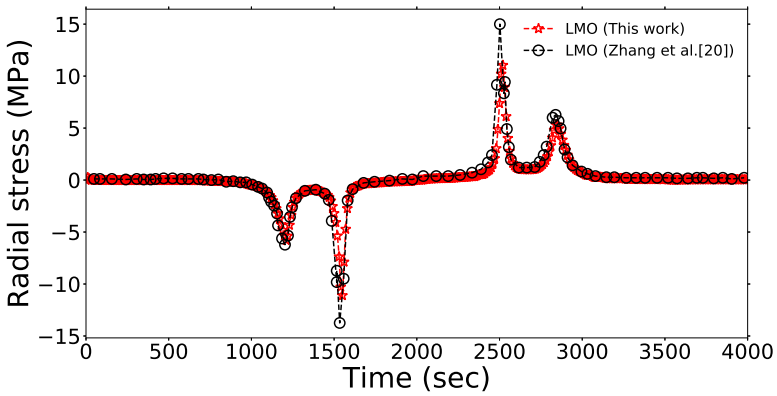

Figure 3.3: Radial stress with charge (de-lithiation) and discharge (lithiation) time.

3.4.2 Effects of Doping

Lattice structure

The lattice constant values of the fully lithiated structure of undoped, doped and co-doped cases are shown in Table 3.6. The results from our MD simulations

show that the lattice length of the undoped crystal and the crystals doped with three transition metals are in close agreement with the experimental data from several studies in the literature. As expected, when doped with a transition metal, the lattice structure shrinks since the ionic radius of all the doping elements are smaller than that of Mn^{3+}. This will impede the diffusion of lithium ions. To overcome this, we can add sulfur as a co-dopant. The addition of sulfur results in an expansion of the crystal because of its larger ionic radius compared to the oxygen ion that it replaces. In Table 3.6, this is evidenced by that fact that LMO-S has a larger lattice length than LMO. Thus, co-doping with S will help offset the shrinking effect of the transition metal dopants and aids the diffusivity of lithium ions. As seen in Table 3.6, the co-doped materials have a larger lattice length compared to the materials doped with just the transition metals. This has also been observed in the literature by other researchers [85, 86].

Table 3.6: Lattice length validation for various doping elements. Numbers in the brackets indicate the references. There is no experimental data available for some of the doped and co-doped substitution in the literature.

Structure	lattice length Å (This work)	lattice length Å (Literature)
LMO	8.235	8.240 - 8.247 [87, 81, 82]
LMO-A	8.217	8.222 [72]
LMO-N	8.220	8.238 [88]
LMO-M	8.208	8.231 [89, 24, 90]
LMO-Y	8.216	–
LMO-S	8.237	–
LMO-SA	8.222	–
LMO-SN	8.224	–
LMO-SM	8.212	–
LMO-SY	8.219	–

The volume expansion during the intercalation process is directly related to the lattice constant. As seen in Figure 3.4, for every co-doped materials, the

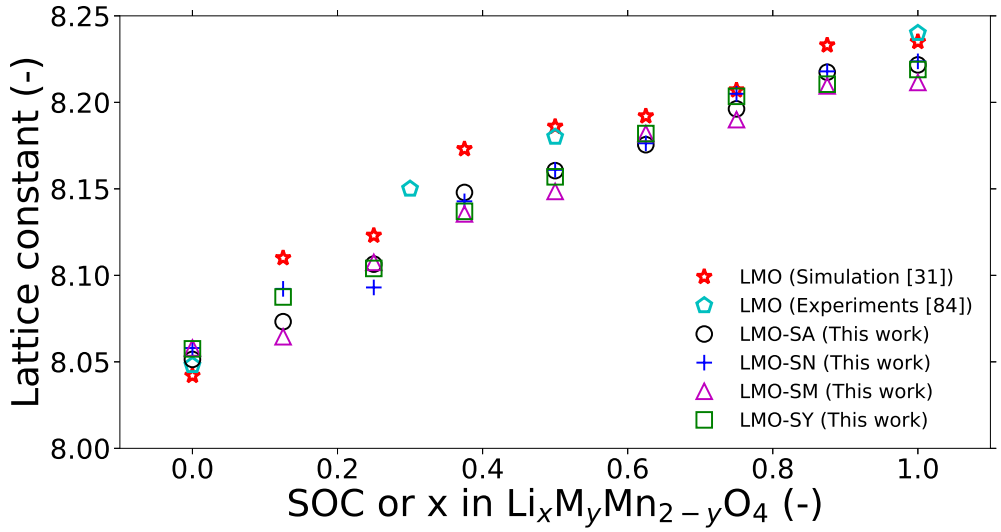

Figure 3.4: Lattice parameter with SOC for $Li_xM_yMn_{2-x-y}O_{4-z}S_z$.

lattice length increases with SOC values. However, for most of the co-doped materials, for a given SOC, the lattice constants are relatively smaller compared to the undoped $Li_xMn_2O_4$. More precisely, the lattice constant varies from 8.042Å in the fully charged state to 8.235Å in the fully discharged state for $Li_xMn_2O_4$. Thus, the total change in the lattice length and volume during a full charging cycle is 2.35% and 6.87%, respectively, and is in excellent agreement with the corresponding experimental values of 2.37% and 6.85%, presented by Park et al. [30]. On the other hand, the change in lattice length and volume over a charge/discharge cycle for new materials (LMO-SA, LMO-SN, LMO-SM, and LMO-SY), are comparatively less which can seen in the Table 4.9. Therefore, the maximum stress due to constant expansion and contraction process will be lower in these new materials.

Elastic properties

In our earlier research on $LiMn_2O_4$, we identified SOC, strain rate, and the temperature as three key parameters that affect the material properties [31]. It was also observed that a material will respond differently to an applied strain based on its charging state. Equation 2.1 clearly shows that the pair interactions, governed by the concentration of lithium-ion in the cathode material, determine the output potential of the system. **SOC**: With an increase in the lithium-ion concentration inside the cathode, SOC increases and this will have an impact on the material properties. **Strain-rate**: In most of the intercalation materials, like $LiMn_2O_4$, an intercalation initiated fracture mechanism is present, particularly at higher temperature and higher strain (charge/discharge) rates wherein the material experiences an intense stress [91]. **Temperature**: With an increase in the temperature of the crystal structure, the kinetic energy of the system increases, directly contributing to the diffusivity of the lithium-ions and the total stress [92].

As described by Lee et al. [53], interactions between the ions contribute significantly to the generation of stress in the cathode material, especially during the intercalation process. With the intercalation or deintercalation of a Li^+ ion, the number of Li^+, Mn^{3+}, and Mn^{4+} changes. This affects the overall ionic interaction, influencing the cathode material's mechanical properties [53]. This implies that the SOC has an impact on the elastic properties of the doped LMO spinel ($LLi_xM_yMn_{2-x-y}O_{4-z}S_z$) material. In order to study the elastic nature of the doped material, uniaxial strain equivalent of 0.5C discharge rate is applied on one of the crystal walls.

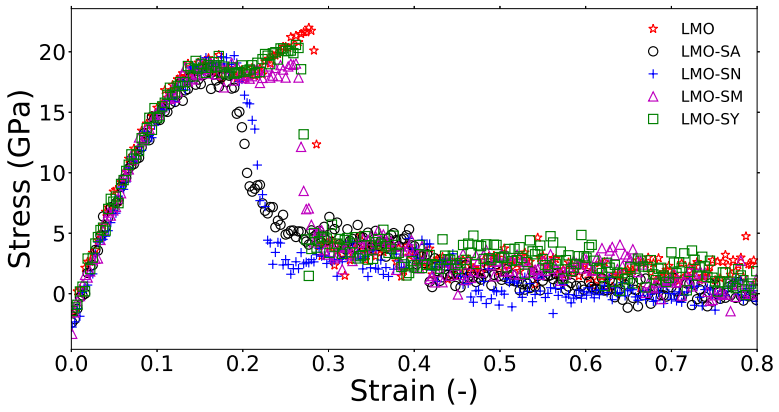

FIGURE 3.5: Stress vs Strain plot for the co-doped materials at SOC=1.

Figure 3.5 shows the stress versus strain plot for the fully lithiated undoped and doped structures. As seen in this figure, the yield stress for all doped elements are similar to that of $LiMn_2O_4$ (Mn^{3+}). However, the ultimate stress is somewhat lower when we use Ni or Al dopants. This can again be explained by the pair interaction theory that is largely responsible for the stress generation. Specifically, with the undoped structure, there is a total of 10 possible ionic pair interactions: Li^+–Li^+, Mn^{3+}–Mn^{3+}, Mn^{4+}–Mn^{4+}, O^{2-}–O^{2-}, Li^+–Mn^{4+}, Li^+–O^{2-}, Mn^{3+}–Mn^{4+}, Li^+–Mn^{3+}, Mn^{3+}–O^{2-}, and Mn^{4+}–O^{2-}. With doping, the total number of pair interaction types will increase as there will also be interaction between the doped elements and the other ions. The lower ultimate stress for Al and Ni can be attributed to their smaller ionic radius and pair interaction contribution in the stress. In the case of $LiMn_2O_4$ spinel, the stress versus strain plot shows a non-linearity around a strain of approximately 0.2, ultimately reaching a maximum stress of around 21.5 GPa at a strain of approximately 0.28. After attaining this peak, the stress decreases rapidly since the material fractures. At SOC=1, the Young's modulus values of LMO-SM and LMO-SY are

very close to the undoped $LiMn_2O_4$. This is evident from the almost overlapping Yield stress part of the curves, which is the linear stress-strain portion up until a strain value of approximately 0.2 in Figure 3.5, and the Young's modulus values summarized in the Table 4.9.

Table 3.7: Reduction in volume expansion and the potential increase in the cycle life of various doping elements.

Structure	Change in length (%)	Change in volume (%)	Change in volume w.r.t. LMO (%)	Young's Modulus (GPa)	Potential increase in # of cycles
LMO	+2.350	+6.87	-	132	-
LMO-SA	+2.071	+6.08	-11.50	118	4570
LMO-SN	+2.015	+5.92	-13.82	125	5353
LMO-SM	+1.869	+5.50	-19.94	128	7718
LMO-SY	+1.965	+5.78	-15.86	128	6093

With the changes in the total number of ions during the charge and discharge cycles, there is a change in the number of ion-pair interactions, affecting the material properties such as Young's modulus [53]. Also, as mentioned in the previous section, the stress-strain behavior is strongly coupled with the SOC [17, 31]. To explore this, we simulated every doped material at all partially charged states. Figure 4.9 shows the stress-strain curve at SOC=0.125, when only 1 out of 8 lithium-ions have been intercalated in the doped host $M_yMn_{2-x-y}O_{4-z}S_z$, and compared with the undoped Mn_2O_4.

In the partially charged states, yield stress values differ for each material. As shown in Figure 4.9 (a), the Yield stress for the Al doped structure (8.10GPa) is almost overlapping with the undoped $Li_{0.125}Mn_2O_4$ crystal (8.11GPa) . On the other hand, the yield stress in LMO-SM (7.3GPa) and LMO-SN (~5GPa) are much lower than the undoped structure (c.f. Figure 4.9 (b) and (c)). This can be attributed to the fact that for partially lithiated cases when the material is doped with ions such as Ni^{2+} or Mg^{2+}, the structure is relatively unstable. On

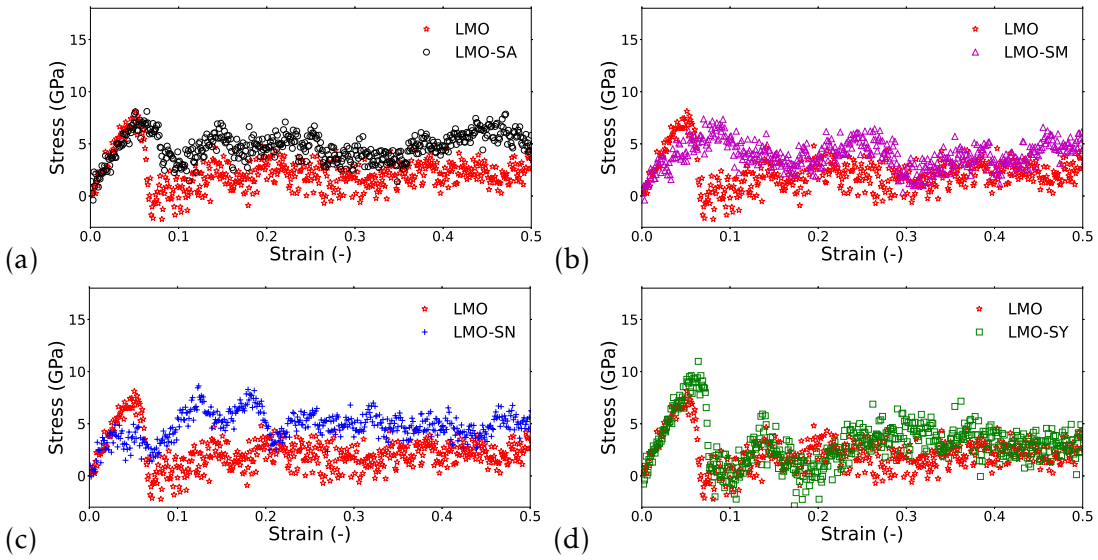

Figure 3.6: Stress vs strain curve at SOC=0.125 for co-doped structures with respect to LMO; Doping elements are (a) S and Al, (b) S and Ni (c) S and Mg, and (d) S and Y.

the other hand, Yttrium doped structure has better yield strength and thereby a better Young's modulus value compared to $Li_{0.125}Mn_2O_4$ at the same state of charge. Again, this is mainly due to the stronger pair interaction between Y^{3+}-O^{2-} compared to Mn^{3+}-O^{2-}. In Figure 3.5, we can observe that for a fully lithiated structure, doping with Yttrium has similar ductility property as pristine $LiMn_2O_4$. Further, as can be seen in Figure 4.9 (d), even in the partially charged state, Y-doped structure tends to fracture much later than other doped materials. Results in Figures 3.5 and 4.9 confirm that doping study on just the fully lithiated structures might not be enough to predict the behaviour of the engineered structure at other charging states. For example, the yield stress part of the curve for LMO-SM overlaps with that of the LMO spinel at SOC=1 (Figure 3.5) but not at SOC=0.125 (Figure 3.6 (b)).

As proposed by Nishijima et al. [93], with a reduction in volume expansion

and contraction, mechanical degradation will be less, and this can enhance the cathode life cycle by up until 80% capacity discharge. In this research, we found that even with a trace amount of doped material (e.g. 5%), there is a significant decrease in the Relative Volume Change (RVC) (c.f.Table 4.9). As summarized in this table, the maximum percentage reduction in the RVC was for LMO-SM. However, as shown in the stress-strain curve for partially charged state in Figure 4.9, the overall yield strength of this material is low and so we might not obtain a significant increase in number of cycles. On the other hand, upon studying the material's stress-strain curve in partially charged states, we found that LMO-SY and LMO-SA are most promising materials with an improved life. However, a conclusion cannot be drawn just yet since the diffusion coefficient, discussed in the ensuing section, is another important material property to be evaluated before concluding that a doping element will improve the LMO spinel's life cycle.

Diffusion coefficient

Lithium ion's ability to diffuse inside the electrolyte and an active cathode particle dictates the performance of the lithium-ion battery. Due to its very light nature and the lack of a suitable radioisotope for lithium-ion, there are very limited experimental investigations on its diffusion coefficient [94]. Further, there is no consensus on the stoichiometric ratio used for these experiments. Here, we use MD simulations to estimate the diffusion coefficient of the lithium-ion in undoped, doped and co-doped LMO spinel phases. In order to understand the effect of the individual elements, diffusion simulations are first performed for undoped structure and compared with transition metal and sulfur doped

cases. Subsequently, the co-doped structures are studied. The calculations have been made for a temperature range of 673K-3000K. Temperatures lower than 673K were not considered because the time required to notice change in the mean square displacement becomes too large due to a subdued diffusion activity. In our MD simulations, for each crystal, the structure was relaxed until the change in total energy is within 5eV. This is followed by equilibration for 20ps, and finally the actual MSD production simulations were performed for another 5ns to study the motion of ions.

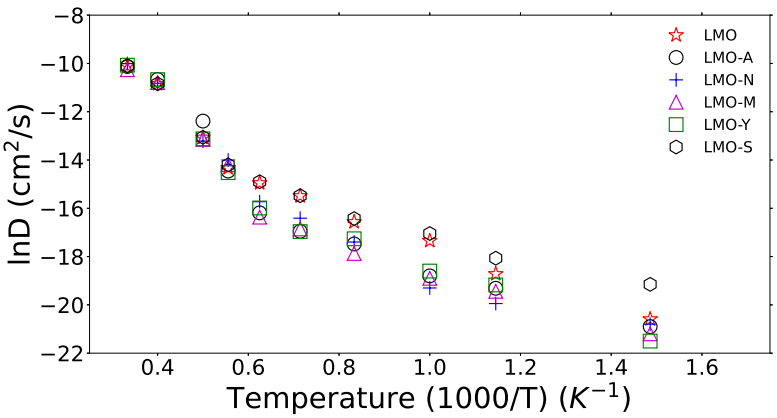

Figure 3.7: Lithium-ion diffusion coefficient as a function of temperature for undoped and doped structures.

As shown in the Figure 3.7, the diffusion coefficient for the transition metal doped structures is slightly lower than the undoped LMO crystal structure. On the other hand, doping with sulfur allows the crystal to expand a bit (c.f. Table 3.6), facilitating the easy migration of lithium ions. This results in an increase in the diffusion coefficient, especially at lower temperatures ($T < 1000$K) (c.f. Figure 3.7). This is consistent with the propositions in the literature [86, 85], and a major reason behind the co-doping strategy. As seen in Figure 3.8, co-doping with S is able to compensate for the marginal decline in the diffusion coefficient

when we dope LMO with transition metals. In fact, in the low temperature zone ($T < 1000$K), the diffusion coefficient is enhanced with the addition of S.

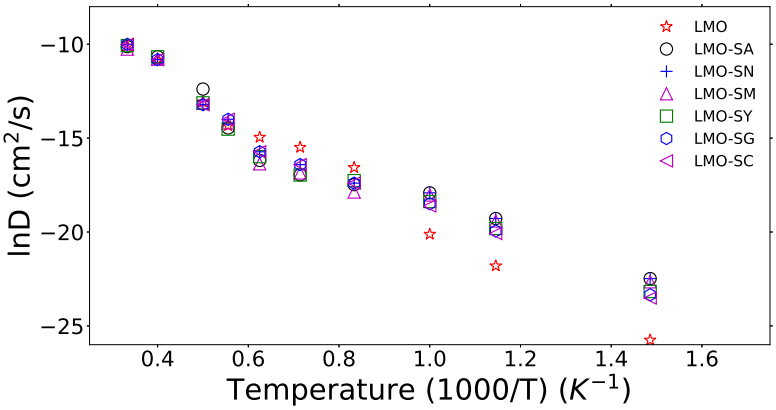

Figure 3.8: Lithium-ion diffusion coefficient as a function of temperature for various co-doped structures.

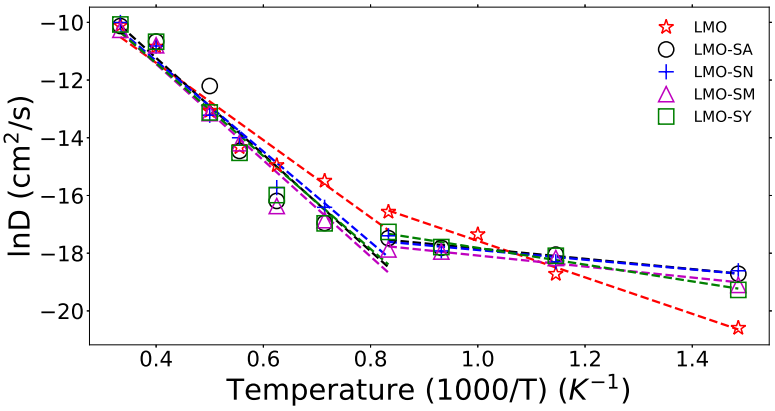

Figure 3.9: The slopes of the dotted lines for each type of material indicate two different activation energies, one each for the two distinct temperature zones bifurcated around the phase transition temperature.

Arrhenius behavior: The effect of temperature on the diffusion of lithium-ions in doped crystals were studied, and the results are plotted in Figure 3.8. The results suggest that we could use the following Arrhenius equation to model the

temperature dependence of the diffusion coefficient:

$$D_{Li^+} = A\ exp\left(-\frac{E_a}{k_B T}\right), \tag{3.14}$$

where A is the pre-exponential constant, E_a is the total activation energy for an ion to migrate, and k_B is the Boltzmann constant (8.62×10^{-8} eV K^{-1}). As per this equation, the diffusion coefficient is directly proportional to the temperature and inversely proportional to the activation energy. If we assume constant values for A and E_a, then $\ln D_{Li^+}$ vs T should exhibit a linear relationship for the entire range of temperature. However, as seen in Figure 3.9, there are two distinct linear regions, bifurcated around the phase transition region. This indicates that the pre-exponential constant and activation energy is probably different in the two regions. This is consistent with the propositions of Zeke et al. [95], i.e., assuming a single value for the activation energy for the entire range of temperature is not appropriate.

On the other hand, the above results can be better explained by the theory suggested by Kuwata et al. [33] and it is also consistent with our earlier findings [31]. Specifically, by splitting the temperature range into two different zones, Zone-Low with $T < 1000$K and Zone-High with $T > 1000$K, and assigning distinct values for A and E_a in each zone, we can employ the ion vacancy and migration theory of Hoang [96] to successfully explain the diffusion phenomena. Specifically, according to this theory, for an ion to diffuse without an available vacant site, the total activation energy required will be the sum of vacancy formation and migration energy. In their experiments, Kuwata et al. [33] calculated the enthalpy of vacancy formation and migration as ~0.6eV and ~0.5eV, respectively.

This is in good agreement with our calculation for LMO (c.f. Table 3.8).

Table 3.8: Lithium-ion diffusion activation energy for various co-doped structures. Note that the experimental values for LMO are from [33], indicating that our calculations are quite accurate.

Element	Migration energy (eV)	Total activation energy (eV)
LMO (expt)	0.50	1.1
Undoped Structure of This Study		
LMO	0.42	1.15
Doped Structures of This Study		
LMO-SA	0.21	1.24
LMO-SN	0.21	1.21
LMO-SM	0.22	1.24
LMO-SY	0.25	1.19

With this validation, we calculated the vacancy migration energy and the total activation energy for the other doped crystals, and the results are summarized in Table 3.8. As seen in this table, for the doped crystals, the migration energy is in the range of 0.21-0.25eV, which is significantly lower compared to 0.42eV for $LiMn_2O_4$. The sharp decline in the vacancy migration energy in the doped materials can be attributed to the presence of S^{2-} ions that enhance the diffusivity of the material by facilitating the easy migration of lithium-ions. This observation is also reported in the work of Kubicka et al. [86] in which they showed that in S-doped spinels the diffusion of Li^+ improved due to lattice expansion caused by the substitution of sulfur.

3.4.3 Inter-atomic distance

The better mechanical properties of the doped crystal structures can also be attributed to the reduced inter-atomic distances. Specifically, the smaller ions that have shorter bonds with other ions will enhance the structural stability. In

this subsection we present the calculated values of the inter-atomic distance between ions. For this, the equilibrium structure of doped $Li_xMn_2O_4$ for different doping elements is studied by evaluating the radial distribution function (RDF), $g(r)$. The RDF represents the spatial positioning of different ions with respect to the central ion in the lattice structure, and can be written as:

$$g_{ij}(r) = \frac{V}{N_i N_j} \sum_{i=1}^{N_{ij}} \frac{n_{ij}}{4\pi r^2 \Delta r}, \tag{3.15}$$

where N_i and N_j represent the total number of ions of type i and j, respectively, in that particular unit cell. V is the total volume occupied by the unit cell, and n_{ij} is the total number of ions in the spherical shell centered around the ion i and between the radii of r and $r + \Delta r$. Figure 3.10 shows the results of the RDF calculation for doped and undoped crystals at 300K.

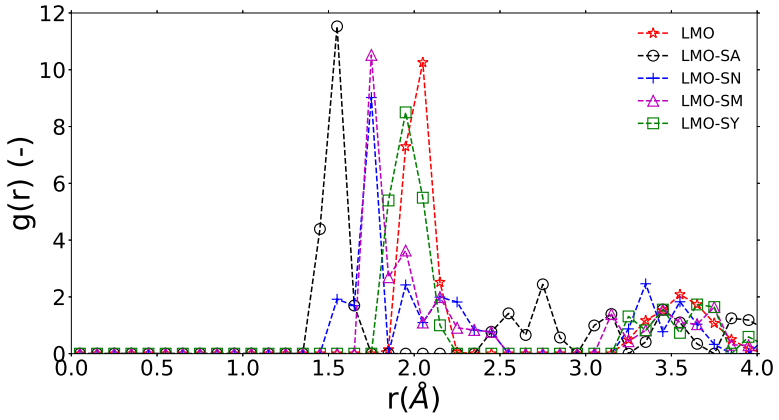

Figure 3.10: Radial distribution function between O^{2-} and other doping ions.

In each curve, the first peak of the curve represents the nearest neighbour distance between two ions, i.e., the bond length. As seen in this figure, every doping element helps reduce the bond length. Finally, though the yield stress

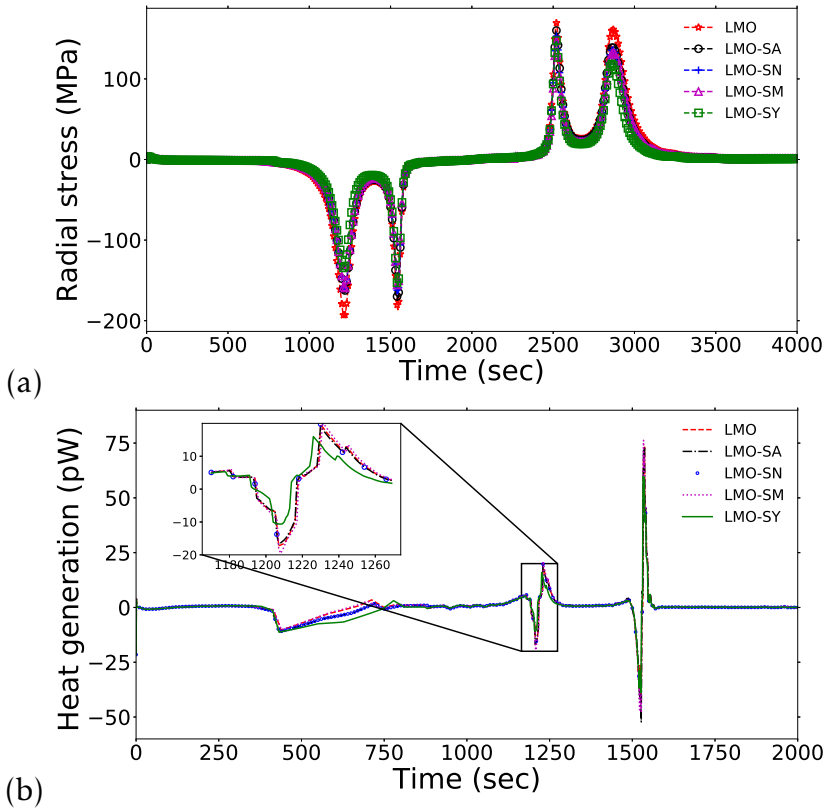

Figure 3.11: (a) Radial stress for a complete charging and discharging cycle. (b) Heat generation during a full charging cycle.

for Al-doped material for the partially charged state is lower than the material with Yttrium doping (c.f. Figure 4.9), the inter-atomic distance between Al^{3+}-O^{2-} is the lowest (c.f. Figure 3.10). This can be attributed to the ionic radius of Aluminum (approximately 1.55Å) that is the lowest among all the dopants. Thus, all the mechanical properties would improve with doping, especially with Yttrium and Aluminum, and we could extend the life of the battery by 4000-7000 cycles with a trace amount of doping.

3.4.4 Macro-scale simulation results

From the investigation so far, it is clear that co-doping with appropriate elements can help improve the LMO spinel's life, i.e., reduce capacity degradation due to battery cycling. Molecular scale investigations have been made to verify that there is no negative impact of doping, by evaluating the diffusion coefficient and the Young's modulus at the molecular level.

In this section, the focus is on the effects of doping on the macro scale behaviour. Specifically, we are interested in knowing if co-doping results in any major changes in the stress and heat generation in the new materials. In doing so, to ensure that the impact of the phenomena at the molecular level are accurately reflected in the macro-scale, key input parameters such as Young's modulus, diffusion coefficient, partial molar concentration etc., have been taken from our MD results.

Figure 3.11a shows the radial stress distribution at the centre of the active particle during complete discharge and charge cycles for doped and undoped materials. As expected, for partial co-doping, there is not much difference

since most of the input parameters are nearly the same. However, the LMO-SY material shows comparatively smaller peaks. This is mainly due to lower strain experienced by it because of smaller volume expansion and better structural stability. Figure 3.11b shows the intercalation induced heat generation during a complete charging cycle. Once again, it can be seen that LMO-SY structure performs slightly better than the other materials. In other words, from the macro-scale simulations it is clear that doping with these elements will not cause any unwanted issues such as thermal runaway.

3.5 Summary and Conclusions

The major drawback of the $Li_xMn_2O_4$ spinel as a cathode material is its reduced cycle life due to large amount of volume expansions and contractions during cycling. To address this drawback and to enhance its material properties, we present a co-doping strategy in this work. Specifically, 5% of the

Mn^{3+} was replaced with other transition metal ions, and 1% of O^{2-} was substituted with S^{2-}. Specific dopants studied in this work include Al, Ni, Mg and Y. Parameters like lattice volume expansion, stress-strain curve, and diffusivity of the Li^+ ions were studied in detail using MD simulations. Further, to study the material behaviour during intercalation process and doping effects on other electrochemical properties of LMO spinel, multi-scale modeling using a combination of Quantum Mechanics, Molecular Dynamics and Computational Fluid Dynamics, has been used. The computational tool was validated by employing it to estimate the lattice constant and diffusion coefficient for the optimized structure of $LiMn_2O_4$ spinel, and comparing the estimates with experimental

data from the literature. An investigation of the co-doping strategies shows that with doping, the overall relative lattice volume expansion during charge and discharge cycles can be reduced by 11-19% in comparison to the pristine undoped material ($LiMn_2O_4$). Though almost same yield and ultimate stresses are reported for fully lithiated case, Yttrium-doped material tends to perform better than undoped $LiMn_2O_4$, especially during partially charged state. Aluminum and Yttrium doped materials have better yield stress compared to other doping elements. We also obtained lower vacancy migration energy (0.21-0.25eV) with the new doped materials proposed in this research. In conclusion, if we replace approximately 5% of the Mn^{3+} with either Al, Mg, Ni or Y, and 1% of the O^{2-} with S^{2-}, the overall life of the LMO spinel material can be improved by 4000-7000 cycles, without compromising on the discharge capacity. Finally, macro scale CFD simulations verify that co-doped engineered structure will help reduce the intercalation induced stress as well as unwanted heat generation.

References

[1] A. Manthiram. "Materials Challenges and Opportunities of Lithium Ion Batteries". In: *J. Phys. Chem. Lett.* 2,3.176-184 (2011).

[2] Y. Yang et al. "Investigations of lithium manganese oxide materials for lithium-ion batteries". In: *J. Power Sources* 65 (1997), pp. 227–230.

[3] J. Shu et al. "A new look at lithium cobalt oxide in a broad voltage range for lithium-ion batteries". In: *J. Phys. Chem. C* 114 (2010), pp. 3323–3328.

[4] Y. Yang et al. "Graphene nanoribbon/V2O5 cathodes in lithium-ion batteries". In: *ACS Appl. Mater. Interfaces* 6 (2014), pp. 9590–9594.

[5] Y. Kim. "Lithium nickel cobalt manganese oxide synthesized using alkali chloride flux: Morphology and performance as a cathode material for lithium ion batteries". In: *ACS Appl. Mater. Interfaces* 4 (2012), pp. 2329–2333.

[6] L. H. Hu et al. "Graphene-modified LiFePO4 cathode for lithium ion battery beyond theoretical capacity". In: *Nat. Commun.* 4 (2013), p. 1687.

[7] X. Hui, L. Zhentao, and Jianping X. "Nanostructured LiMn2O4 and their composites as high-performance cathodes for lithium-ion batteries". In: *Progress in Natural Science: Materials International* 22.572-584 (2012).

[8] E. Iguchi et al. "Electrical transport properties in LiMn2O4, Li0.95Mn2O4, and LiMn1.95B0.05O4 (B=Al or Ga) around room temperature". In: *Journal of Applied Physics* 91.2149 (2002).

[9] S. Y. Luchkin et al. "Li transport in fresh and aged LiMn2O4 cathodes via electrochemical strain microscopy". In: *Journal of Applied Physics* 118.072016 (2015).

[10] R. Sharma, N. Sharma, and M. Sharma. "LiMn2O4 spinel structure as cathode material for Li-ion batteries". In: *AIP Conference Proceedings* 2142.040024 (2019).

[11] H. Y. Amanieu et al. "Mechanical properties of commercial LixMn2O4 cathode under different State of Charge". In: *Acta Materialia* 89 (2015), pp. 153–162.

[12] J.M. Tarascon and M. Armand. "Issues and challenges facing rechargeable lithium batteries". In: *Nature* (2001).

[13] J. Cabana et al. "Enhanced high rate performance of LiMn2O4 spinel nanoparticles synthesized by a hard-template route". In: *J. Power Sources* (2007).

[14] C. Julien et al. *Lithium Batteries: Science and Technology*. Springer International Publishing, 2016.

[15] J.and Thomas K.E. Newman, H. Hafezi, and Wheeler D.R. "Modelling of Lithium-ion batteries". In: *J. Power Sources* 119 (2003), pp. 838–843.

[16] J. Christensen and J. Newman. "A Mathematical Model of Stress Generation and Fracture in Lithium Manganese Oxide". In: *J. Electrochem. Soc.* 153 (2006), A1019.

[17] W. H. Woodford, Y.-M. Chiang, and W. C. Carter. ""Electrochemical Shock" of Intercalation Electrodes: A Fracture Mechanics Analysis". In: *J. Electrochem. Soc.* (2010), A1052.

[18] Y. Hu, X. Zhao, and Z. Suo. ""Averting cracks caused by Insertion reaction In lithium-ion batteries". In: *J. Mater. Res., 2010* (2010).

[19] X. Zhang, W. Shyy, and A. M. Sastry. "Numerical Simulation of Intercalation-Induced Stress in Li-Ion Battery Electrode Particles". In: *J. Electrochem. Soc.* 154 (2007), A910.

[20] X. Zhang, A. M. Sastry, and W. Shyy. "Intercalation-Induced Stress and Heat Generation within Single Lithium-Ion Battery Cathode Particles". In: *J. Electrochem. Soc.* 155 (2008), A542.

[21] J. Christensen. "Modeling Diffusion-Induced Stress in Li-Ion Cells with Porous Electrodes". In: *J. Electrochem. Soc.* 157 (2010), A366.

[22] Y. Tesfamhret et al. "On the Manganese Dissolution Process from LiMn2O4 Cathode Materials". In: *ChemElectroChem* 8.8 (2021), pp. 1516–1523.

[23] P. Angelopoulou et al. "Enhanced Performance of LiAl0.1Mn1.9O4 Cathode for Li-Ion Battery via TiN Coating". In: *Energies* 14.4 (2021), p. 825.

[24] Z. Yang et al. "Mg2+ and Ti4+ Co–Doped Spinel LiMn2O4 as Lithium-Ion Battery Cathode". In: *Chemistry SELECT* 4.33 (2019), pp. 9583–9589.

[25] Y. Deng et al. "Enhanced Electrochemical Performance in Ni-Doped LiMn2O4-Based Composite Cathodes for Lithium-Ion Batteries". In: *ChemElectroChem* 4.6 (2017), pp. 1362–1371.

[26] M. Michalska et al. "Improved electrochemical performance of LiMn2O4 cathode material by Ce doping". In: *Electrochimica Acta* 276 (2018), pp. 37–46.

[27] R. Thirunakaran et al. "Cerium and zinc: Dual-doped LiMn2O4 spinels as cathode material for use in lithium rechargeable batteries". In: *Journal of Power Sources* 187.2 (2009), pp. 565–574.

[28] D. Zhang, B.N. Popov, and R.E. White. "Electrochemical investigation of CrO2.65 doped LiMn2O4 as a cathode material for lithium-ion batteries". In: *Journal of Power Sources* 76.1 (2009), pp. 81–90.

[29] D.-L. Fang et al. "Synthesis of a Co–Ni doped LiMn2O4 spinel cathode material for high-power Li-ion batteries by a sol–gel mediated solid-state route". In: *Journal of Alloys and Compounds* 640 (2015), pp. 82–89.

[30] J. Park, W. Lu, and A. M. Sastry. "Numerical Simulation of Stress Evolution in Lithium Manganese Dioxide Particles due to coupled Phase Transition and Intercalation". In: *J. Electrochem. Soc.* 158.2 (2011), A201–A206.

[31] R. Tyagi and S. Srinivasan. "Molecular Dynamics modelling of lithium ion intercalation induced change in the mechanical properties of LixMn2O4". In: *J. Chem. Phys.* 153 (2020), p. 164712.

[32] M. Y. Saidi, J. Barker, and Koksbang R. "Thermodynamic and Kinetic Investigation of Lithium Insertion in the Li1-xMn2O4 Spinel Phase". In: *JOURNAL OF SOLID STATE CHEMISTRY* 122 (1996), pp. 195–199.

[33] N. Kuwata et al. "Lithium diffusion coefficient in LiMn2O4 thin films measured by secondary ion mass spectrometry with ion-exchange method". In: *Solid State Ionics* 320 (2018), pp. 266–271.

[34] S. Takai et al. "Tracer diffusion coefficients of lithium ion in LiMn2O4 measured by neutron radiography". In: *Solid State Ionics* 256 (2014), p. 93.

[35] P. Giannozzi et al. "QUANTUM ESPRESSO: a modular and open-source software project for quantum simulations of materials". In: *J. Phys.: Condens. Matter* 21.39 (2009), p. 5502.

[36] D. Vanderbilt. "Soft self-consistent pseudopotentials in a generalized eigenvalue formalism". In: *Phys. Rev. B* 41 (1990), p. 7892.

[37] A. D. Corso. "Pseudopotentials periodic table: From H to Pu". In: *Computational Materials Science* 95 (2014), pp. 337–350.

[38] R.O. Jones and O. Gunnarsson. "The density functional formalism, its applications and prospects". In: *Reviews of Modern Physics* 61.3 (1989), pp. 689–746.

[39] J. P. Perdew, K. Burke, and M. Ernzerhof. "Generalized Gradient Approximation Made Simple". In: *Phys. Rev. Lett.* 78 (1997), p. 1396.

[40] H. J. Monkhorst and J. D. Pack. "Special points for Brillouin-zone integrations". In: *Phys. Rev. B* 13.12 (1976), pp. 5188–5192.

[41] B. V. Merinov et al. "Li-diffusion at the interface between Li-metal and [Pyr14][TFSI]-ionic liquid: Ab initio molecular dynamics simulations". In: *J. Chem. Phys.* 152 031101 (2020).

[42] C. A. Brackley, A. N. Morozov, and D. Marenduzzo. "Models for twistable elastic polymers in Brownian dynamics, and their implementation for LAMMPS". In: *J. Chem. Phys.* 140 135103 (2014).

[43] J. C. Tully. "Molecular dynamics with electronic transitions". In: *J. Chem. Phys.* 93 1060 (1990).

[44] Y. Ida. "Interionic repulsive force and compressibility of ions". In: *Phys. Earth Planet.* (1976).

[45] K. Suzuki et al. "Structural properties of LixMn2O4 as investigated by molecular dynamics and density functional theory". In: *Japanese J. Appl. Physics, Part 1 Regul. Pap. Short Notes Rev. Pap.* (2000).

[46] K.E. Sickafus, J.M. Wills, and N.W. Grimes. "Structure of Spinel". In: *J. Am. Ceram. Soc.* (2004).

[47] S Plimpton. "Fast Parallel Algorithms for Short-Range Molecular Dynamics". In: *J. Comp. Phys.* 117 (1995), p. 1.

[48] R.T. Cygan, H.R. Westrich, and D.H. Doughty. "Ionic modeling of lithium manganese spinel materials for use in rechargeable batteries". In: *Mater. Res. Soc. Proc* 393 (1995), p. 113.

[49] G. V. Lewis and C. R. A. Catlow. "Potential models for ionic oxides". In: *J. Phys. C: Solid State Phys* 18 (1985), p. 1149.

[50] P. P. Ewald. "The calculation of optical and electrostatic grid potential". In: *Ann. Phys. (Leipzig)* 64.253 (1921).

[51] S. Nose. "A unified formulation of the constant temperature molecular dynamics methods". In: *J. Chem. Phys.* 81 (1984), pp. 511–519.

[52] A. Asadi, S. Aghamiri, and M. Talaie. "Molecular dynamics simulation of a LixMn2O4 spinel cathode material in Li-ion batteries". In: *RSC Advances* (2016).

[53] S. Lee et al. "Molecular Dynamics Simulations of SOC-Dependent Elasticity of LixMn2O4 Spinels in Li-Ion Batteries". In: *J. Electrochem. Soc.* 160.6 (2013), A968–A972.

[54] A.K. Subramaniyan and C.T. Sun. "Continuum interpretation of virial stress in molecular simulations". In: *Int. J. Solids Struct.* (2008).

[55] A. Adan, C. T. Sun, and H. Mahfuz. "A molecular dynamics simulation study to investigate the effect of filler size on elastic properties of polymer nanocomposites". In: *Composite Science and Technology* 67 (2007), pp. 348–356.

[56] J.L. Chu and S. Lee. "The effect of chemical stresses on diffusion". In: *J. Appl. Phys.* 75 (1994), pp. 2823–2829.

[57] T. F. Fuller, M. Doyle, and J. Newman. "Simulation and Optimization of the Dual Lithium Ion Insertion Cell". In: *J. Electrochem. Soc.* 141.1 (1994).

[58] M. Doyle and J. Newman. "Modeling the performance of rechargeable lithium-based cells: design correlations for limiting cases". In: *J. Power Sources* 54 (1995), pp. 46–51.

[59] M. M. Thackeray. "Manganese oxides for lithium batteries". In: *Prog. Solid State Chem.* 25.1 (1997).

[60] D. Zhang, B.N. Popov, and R.E. White. "Modeling Lithium Intercalation of a Single Spinel Particle under Potentiodynamic Control". In: *J. Electrochem. Soc.* 147 (2000), pp. 831–838.

[61] K. E. Thomas and J. Newman. "Thermal Modeling of Porous Insertion Electrodes". In: *J. Electrochem. Soc.* 150 (2003), A176–A192.

[62] K. E. Thomas, C. Bogatu, and J. Newman. "Measurement of the Entropy of Reaction as a Function of State of Charge in Doped and Undoped Lithium Manganese Oxide". In: *J. Electrochem. Soc.* 148.6 (2001), A570.

[63] M. S. Whittingham. "Ultimate Limits to Intercalation Reactions for Lithium Batteries". In: *Chem. Rev.* 114.23 (2014), pp. 11414–11443.

[64] L. Mai et al. "Nanowire Electrodes for Electrochemical Energy Storage Devices". In: *Chem. Rev.* 114.23 (2014), pp. 11828–11862.

[65] M. S. Islam and C. A. J. Fisher. "Nanowire Electrodes for Electrochemical Energy Storage Devices". In: *Chem. Soc. Rev.* 43.1 (2014), pp. 185–204.

[66] J. B. Goodenough and Y. Kim. "Challenges for Rechargeable Li Batteries". In: *Chem. Mater.* 22.3 (2010), pp. 587–603.

[67] L. Zhang et al. "Sphere-Shaped Hierarchical Cathode with Enhanced Growth of Nanocrystal Planes for High-Rate and Cycling-Stable Li-Ion Batteries". In: *Nano Lett.* 15.1 (2015), pp. 656–661.

[68] Y. Z. Zheng et al. "Nickel-mediated polyol synthesis of hierarchical V2O5 hollow microspheres with enhanced lithium storage properties". In: *J. Mater. Chem. A* 3 (2015), pp. 1979–1985.

[69] M. Zhi et al. "Nanostructured carbon–metal oxide composite electrodes for supercapacitors: a review". In: *Nanoscale* 5 (2013), pp. 72–88.

[70] Z. Moradi, A. Lanjan, and S. Srinivasan. "Enhancement of Electrochemical Properties of Lithium Rich Li2RuO3 Cathode Material". In: *J Electrochemical Society* 167.11 (2020), p. 110537.

[71] Z. Moradi, A. Lanjan, and S. Srinivasan. "Multi-Scale Investigation into Co-Doping Strategy on The Electrochemical Properties of Li2RuO3 Cathode for Li-Ion Batteries". In: *ChemElectroChem* 8.1 (2021), pp. 112–124.

[72] L. Xiao et al. "Enhanced electrochemical stability of Al-doped LiMn2O4 synthesized by a polymer-pyrolysis method". In: *Electrochimica Acta* 54.2 (2008), pp. 545–550.

[73] H. Zhang et al. "Structure and Performance of Dual-doped LiMn2O4 Cathode Materials Prepared via Microwave Synthesis Method". In: *Electrochimica Acta* 125 (2014), pp. 225–231.

[74] M. Molenda et al. "Synthesis and characterisation of sulphided lithium manganese spinels LiMn2O4-ySy prepared by sol-gel method". In: *Solid State Ionics* 176 (2005), pp. 1702–1709.

[75] M. Bakierska, M. Molenda, and R. Dziembaj. "Optimization of sulphur content in LiMn2O4-ySy spinels as cathode materials for lithium-ion batteries". In: *Procedia Eng* 98 (2014), pp. 20–27.

[76] M. Nakayama, M. Kanekoa, and M. Wakiharaa. "First-principles study of lithium ion migration in lithium transition metal oxides with spinel structure". In: *Phys. Chem. Chem. Phys.* 14 (2012), pp. 13963–13970.

[77] K. Okhotnikov, B. Stevensson, and M. Eden. "New interatomic potential parameters for molecular dynamics simulations of rare-earth (RE = La, Y, Lu, Sc) aluminosilicate glass structures: exploration of RE3+ field-strength effects". In: *Phys. Chem. Chem. Phys.* 15 (2013), pp. 15041–15055.

[78] P. Shukla et al. "Effect of inversion on thermoelastic and thermal transport properties of MgAl2O4 spinel by atomistic simulation". In: *J Mater Sci* 46 (2011), pp. 55–62.

[79] P. D. Battle, T. S. Bush, and C. A. Catlow. "Structures of Quaternary Ru and Sb Oxides by Computer Simulation". In: *J. Am. Chem. Soc.* 117.23 (1995), pp. 6292–6296.

[80] K. Wright and J. D. D. Gale. "Interatomic potentials for the simulation of the zinc-blende and wurtzite forms of ZnS and CdS: Bulk structure, properties, and phase stability". In: *Phys. Rev. B* 70 (2004), p. 035211.

[81] Y.Y. Xia and M. Yoshio. "An investigation of lithium ion insertion into spinel structure Li-Mn-O compounds". In: *Journal of The Electrochemical Society* 143.3 (1996), pp. 825–833.

[82] N. Ishizawa et al. "Structural disorder along the lithium diffusion pathway in cubically stabilized lithium manganese spinel: I. Synchrotron X-ray studies". In: *Journal of Solid State Chemistry* 174.1 (2003), pp. 167–174.

[83] M.D. Chung et al. "Implementing Realistic Geometry and Measured Diffusion Coefficients into Single Particle Electrode Modeling Based on Experiments with Single LiMn2O4 Spinel Particles". In: *J. Electrochem. Soc.* 158.4 (2011).

[84] D. Clerici, F. Mocera, and A. Soma. "Analytical Solution for Coupled Diffusion Induced Stress Model for Lithium-Ion Battery". In: *energies* 13.7 (2020), p. 1717.

[85] K. Okada, I. Kimura, and K. Machida. "High rate capability by sulfur-doping into LiFePO4 matrix". In: *RSC Adv.* 8.11 (2018), pp. 5848–5853.

[86] M. Kubicka et al. "The Temperature Effect on the Electrochemical Performance of Sulfur-Doped LiMn2O4 in Li-Ion Cells". In: *Nanomaterials* 9 (2019), p. 1722.

[87] D. Zhan et al. "Al-doped LiMn2O4 single crystalline nanorods with enhanced elevated-temperature electrochemical performance via a template-engaged method as a cathode material for lithium ion batteries". In: *RSC Adv.* 5.9 (2015), pp. 6372–6377.

[88] J. H. Lee et al. "Degradation mechanisms in doped spinels of LiM0.05Mn1.95O4 (M=Li, B, Al, Co, and Ni) for Li secondary batteries". In: *Journal of Power Sources* 89.1 (2000), pp. 7–14.

[89] A. Llusco, M. Grageda, and S. Ushak. "Kinetic and Thermodynamic Studies on Synthesis of Mg-Doped LiMn2O4 Nanoparticles". In: *nanomaterials* 10.7 (2020), p. 1409.

[90] Y. Yu et al. "Enhancing the durable performance of LiMn2O4 at high-rate and elevated temperature by nickelmagnesium dual doping". In: *Nature* 9 (2019), p. 16864.

[91] E. V. Vakarin, G. G. Belmonte, and J. P. Badiali. "Interplay of host volume variations and internal distortions in the course of intercalation into disordered matrices". In: *J. Chem. Phys.* 126.234709 (2007).

[92] N. H. Nachtrieb, E. Catalano, and J. A. Weil. "Self-Diffusion in Solid Sodium. I". In: *J. Chem. Phys.* 20.1185 (2004), p. 1952.

[93] M. Nishijima et al. "Accelerated discovery of cathode materials with prolonged cycle life for lithium-ion battery". In: *Nature Communications* 5 (2014), p. 4553.

[94] N. Kuwata et al. "Lithium diffusion coefficient in amorphous lithium phosphate thin films measured by secondary ion mass spectroscopy with isotope exchange methods". In: *Solid State Ionics* 294 (2016), pp. 59–66.

[95] A. P. Zeke, O. M. Oluwaseun, and H. T. Ward. "Activation Energies and Beyond". In: *J. Phys. Chem.* 123 (2019), pp. 7185–7194.

[96] K. Hoang. "Understanding the electronic and ionic conduction and lithium over-stoichiometry in LiMn2O4 spinel". In: *J. Mater. Chem.* A.2 (2014), p. 18271.

Chapter 4

Molecular Dynamics modelling for engineered cathode structures

Prelude: This chapter is been re-produced from the following manuscript with permission from Royal Society of Chemistry Publishing:
R. Tyagi, and S. Srinivasan, "Co-Doping Studies to Enhance the Life and Electro-Chemo-Mechanical Properties of $Li_xMn_2O_4$ Cathode using Multi-scale Modeling and Neuro-Computing Techniques ", Phys. Chem. Chem. Phys., 2022.

Contributing Author: Ramavtar Tyagi

Abstract

A number of engineered cathode materials with longer life cycle and better electro-chemo-mechanical properties can be obtained by partially replacing

some of the elements with other relevant once without compromising much with structure. To design such superior cathode materials, in this work, we replace a small number (5% or 10%) of Mn^{3+}, with one of the following elements: Aluminium, Nickel, Magnesium, Gallium, Chromium, and Yttrium. Additionally, S^{2-} and F^{-} were used to replace some ($\sim$ 1%) of the O^{2-} ions (anion) in the crystal. In this work we have used a combination of Quantum Mechanics (QM), Molecular Dynamics (MD), Neural Network (NN) and Computational Fluid Dynamics (CFD) modeling. QM has been used to validate the Molecular Dynamics (MD) simulation results for engineered structures where experimental data not available. MD simulations are used for material properties such as lattice expansion, Young's modulus, diffusion coefficients for un-doped, doped and co-doped structures. NN models are implemented in order to reduce the computational time to evaluate millions of possible crystal configurations. CFD modeling is utilized to study the impact of co-doping strategies at macroscale. As a first step, we employed neuro-computing techniques to identify the optimum ionic configuration for all crystal structure, saving ~88% of the computational time. Next, molecular scale simulations were performed to study the material properties. Molecular Dynamics (MD) modeling findings suggest that relative volume expansion between fully charged and discharged state of the battery can be reduced by ~1.9% to ~2.25%, indicating an improvement in the life of the cathode material by several hundreds of cycles. Findings from both QM and MD simulations suggest that for these novel engineered materials, electro-chemo-mechanical properties such as ionic mobility, chemical diffusion coefficient and elasticity, improved. Further, MD simulations showed that the inter-ionic space

between doped metal ions and oxygen is smaller compared to the spacing between Mn^{3+}-O^{2-} in the original LMO spinel, indicating an improvement in the material's structural strength along with total number of discharge cycle. Finally, macro scale computational modelling results shows that chances of thermal runaway can be reduced significantly for some of the co-doped structures since the intercalation induced maximum stress is lower.

4.1 Background

Climate change and the continuously deteriorating environment is reminding us to move towards sustainable energy technologies. A major problem with most of the renewable energy technologies such as wind and solar is that unlike conventional power generation methods, they are inconsistent. Therefore, the need for highly efficient, environmental friendly, and economical energy storage technologies have increased exponentially in the last few decades. Lithium ion batteries (LIBs) are a very promising technological solution for the exponentially growing energy storage demand, especially in the consumer electronics and automotive sectors. This has only been possible due to improved energy densities of LIBs [1] in the last few years. In any LIB, electrodes are the important components as they dictate the energy storage capacity of the battery. Ideally, the anode's electric potential should be significantly lower than the cathode, providing a high potential difference. This limits the possible materials that can be used as an anode. Currently, Graphite or Silicon are widely used anode materials [2]. While cathode materials have been explored more [3, 4, 5], more recently, there has been a lot of focus on the Li-metal, lithium alloyed metals,

carbon nano-tubes, graphene, and Lithium Titanate Oxide (LTO) based anode materials [6, 7, 8].

With respect to cathodes, Lithium Cobalt Oxide ($LiCoO_2$) and it's derivatives are widely used especially in the long range Electric Vehicles [9]. However, Cobalt is expensive and toxic, prompting researchers to explore the doped variants such Nickel Cobalt Aluminium ($LiNi_xCo_{1-x-y}Al_yO_2$) and Nickel Manganese Cobalt ($LiNi_xMn_yCo_{1-x-y}O_2$) that are more popular these days [7, 4]. It must be noted though that the addition of Ni introduces the risk of hazards such as thermal runaway [10]. Lithium Manganese Oxide ($LiMn_2O_4$) spinel or LMO spinel has been explored in the past and mostly used in the low energy density applications [11, 12, 13, 14, 15]. Its advantages over other cathode materials like Lithium Cobalt Oxide ($LiCoO_2$), Lithium Nickel Oxide ($LiNiO_2$) and Lithium-titanate (Li_2TiO_3) include lower cost, abundant availability of Manganese, and no toxicity. Further, Lithium Iron Phosphate ($LiFePO_4$) is also another material which is gaining popularity due to its longer life. However, compared to a LMO spinel, it suffers from low values of operating potential, ionic conductivity and energy density [16, 17].

While it has its advantages, a $LiMn_2O_4$ spinel suffers from a relatively higher mechanical stress induced by higher volume change during the charge and discharge cycles [18]. It also experiences cycling capacity fade due to the structural changes induced by the dissolution of Manganese [19]. In fact, this is one of the key degradation mechanisms, impacting the battery life [20, 21, 22, 23, 24, 25, 26]. Christensen et. al [27] have developed a model which can estimate the stress generated due to the lithium ion intercalation inside the cathode material.

Specifically, as the lithium content in the anode increases, the number of Mn^{3+} replacing Mn^{4+} increases. The former has a larger ionic radius, resulting in the expansion of the crystal.

Additionally, Mn^{3+} tends to dissolve in the electrolyte and converts into Mn_2O_3, aggravating the degradation of the cathode material [28]. To avoid such problems, thin surface coatings over $LiMn_2O_4$ have been tried to reduce or inhibit the manganese dissolution [29, 30]. However, coating layers cannot ameliorate the effect of Jahn-teller instability [31]. Recent investigations have focused on partial substitution of Mn^{3+} by elements with similar properties (Al, Ni, Co, Mg, etc.) to enhance the life cycle of a LMO spinel [32, 33, 34, 35, 36, 37, 38, 39, 40]. Researchers have shown that by resolving some of the above issues, the overall life of the cathode material LMO spinel could be enhanced by as much as 2000 cycles at room temperature[41]. However, these doped structures suffer from irreversible capacity fading at elevated temperature (>318K). Recently, there has been a focus on introducing partial substitutions with anions such as S^{2-} and F^{-} in place of O^{2-}, to improve the efficiency of energy storage at elevated temperatures [42]. In this work, we focus on studying co-doping with cations instead of Mn^{3+}, and anions such as S^{2-} and F^{-} to partially replace O^{2-}.

Computational investigations have made it possible to design, develop and test several engineered microstructures and novel chemistries, and to study the performance analysis of the batteries under various operating conditions [22]. One of the issues with these simulations is the inconsistency in the parameter values that are deduced from different experimental researchers, especially for the intermediate charging states [22, 23, 26, 43]. Multi-scale modeling techniques

can overcome this challenge by accounting for a multitude of phenomena at varying time and length scales in a cathode material. Hence, such formulations can be used for a quicker and accurate evaluation of various lithiated structures.

In a recent work [44, 45], as highlighted in Chapter 2 and 3, we have successfully demonstrated how molecular dynamics simulations can be used to accurately predict the input properties such as Elastic modulus, diffusion coefficient, and activation energy. We showed that, investigating the ionic movements at atomic level and extracting the material properties such as electrical, chemical and mechanical from there for all engineered structures will help us obtain accurate input parameters for macro scale modeling [44, 45]. In this chapter, we investigate the influence of more number of cation dopants, namely, Al, Ni, Mg, Ga, Cr and Y on the properties and performance of the battery. Additionally, we also study the influence of co-dopants such as S^{2-} and F^{-}.

These co-doping strategies were evaluated by studying key material properties such as Young's modulus, diffusion coefficient, stress and heat generation inside the structure are studied in detail.

One of major challenges in the computational modeling techniques from Chapters 2 and 3 is the innumerable potential ionic configurations, especially for co-doped engineered structures. Evaluating all the possible configurations using detailed MD or QM simulations is not computationally feasible, and yet important to ensure that an exhaustive search has been undertaken. In order to solve this problem, in this chapter principles of Artificial Neural Network (ANN) has been employed to minimize the computational time and evaluate all possible

crystal configurations. In Section 4.2, guidelines for further dopants along with important properties which qualify them to be potential doping candidate are described in detail. Further, ANN modeling along with other previously studied models such as Molecular Dynamics, Quantum Mechanics, and Macro scale simulations are described in the Sections 4.3-4.6. In Section 4.7, findings from different modeling techniques are presented and validated with the experimental results wherever it was possible. In Section 4.8, the conclusions identifying the optimal co-doping structures for a longer battery life are presented.

4.2 Doping Ions Guidelines

As highlighted in our previous work [44, 45], in addition to the cell voltage gap between HOMO and LUMO, the electronegativity difference between the anions and cations also determine the stability of the crystal structure. Further, a change in the Gibbs free energy, and the possible electropotential value of a cathode or anode material, depends upon the radius of ions of the elements in the crystal structure, and the oxidizing power of the anion.

Generally, the electro-chemo-mechanical properties of any material is mostly governed by the quantum chemistry and microstructures which are determined by the elements used to form a particular crystal. However, it is entirely possible for the same elements to form a different molecular structure based on the synthesis process it has undergone and the surrounding conditions. For instance, if the same ions are inserted into the host material from a different side of the crystal, it can open up the crystal structure and make the migration of the ions easy [46]. Although the microstructures of any crystal is its natural

property, it is possible to alter it by inserting appropriate elements. Thus, partial insertion of one or more types of elements can change the dimensions of the crystal significantly, enabling the refinement of the microstructure of some of the materials [47].

In considering some of these important parameters to develop novel materials with enhanced properties, there are several design guidelines suggested in the literature as well as in Section 3.3, to select potential cathode materials. These include the impact of the elements on the society, economic affordability, and ease of use. Apart from these, one should also consider their availability in nature, ability to support environmental friendly manufacturing processes, and re-usability and re-cycling ability. A critical requirement of the cathode material is its ability to hold a large amount of reversible energy within the electrochemical potential gap. This is defined by the maximum energy storage limit of any electrode material which is basically the maximum re-usable energy it can offer when battery starts discharging, and is calculated using the Equation 3.13 [48].

The factor 3.6 in the Equation 3.13 is used to convert the energy capacity from Coulomb/sec to mAh/g. Generally, the number of electrons in a cathode material is decided by the change in the ionic charge of the transition metal as it dictates the number of lithium ions it can accommodate per formulae unit. Recently, numerous rare earth elements such as Nb, Zr, La, Ru, Mo, etc. have been tested as doping elements [49, 50]. To avoid expensive, environmental unfriendly, toxic and rare earth materials, only metal ions have been considered as candidates in this research. The major advantage of some of the metal oxides are that they can change their valance states, offering more electrons if needed.

Table 4.1 shows the extended list of the doping and co-doping ions along with the relevant properties.

Table 4.1: Properties of the doping elements.

Element	Oxidizing power	Ionic radius(Å)	Electronegativity
Al^{3+}	−1.66	0.530	1.5
Ni^{2+}	−0.26	0.700	1.9
Mg^{2+}	−2.36	0.720	1.2
Y^{3+}	−0.22	0.900	1.22
Ga^{3+}	−0.55	0.620	1.6
Cr^{3+}	−0.74	0.630	1.6
S^{2-}	+1.20	1.840	2.5
F^{-}	+2.87	1.330	4.0

With these criteria and guidelines, numerous positive bivalent and mostly trivalent elements are identified as good replacement for substituting some fraction of the Mn^{3+} ions. Particularly, the elements of interest include Aluminium, Nickel, Magnesium, Yttrium, Chromium, and Gallium. As summarized in the Table 4.1, among all selected elements, Al^{3+} is the smallest with an ionic radius of 0.53Å. Therefore, the bond length with anions will be smaller, making it much stronger. This is in addition to its abundant availability [51]. Mg and Ni are bivalent elements that can change the charge valence and hence can increase the voltage of the battery. Since ionic radius (0.72Å) and electronegativity are low, it is expected to form a stronger Mg-O bond with anions [52]. Both Ga and Cr offer almost similar ionic radius (0.62Å and 0.63Å, respectively) and electronegativity values, making them good candidates to replace Mn^{3+}. Although, Yttrium is a comparatively large and heavy element, it offers low oxidizing power and electronegativity, and hence forms a stronger bond with anions, helping improve the structural strength.

In addition to these, to enhance the ionic diffusivity and structural strength at elevated temperatures, co-doping with anions such as Sulfur and Fluorine has been explored [53, 54, 55]. It must be noted that doping with the smaller transition metal ions can shrink the crystal size and hinder the lithium ion diffusivity. Recent studies suggest that the impact can be reduced by trace doping with Sulfur ions, replacing oxygen in the crystal structure [56, 57]. Therefore, based on the parametric values shown in the Table 4.1, in addition to doping with metal ions, 1% of the O^{2-} positions are filled either by S^{2-} or by F^{-}, resulting in $Li_xM_yMn_{2-x-y}O_{4-z}S_z$ or $Li_xM_yMn_{2-x-y}O_{4-z}F_z$ structures.

To study the effect of individual dopants, the following sets of simulations are carried out: 1. Simulation of undoped LMO spinel is the baseline model. 2. Simulation with an individual doping element (Al, Ni, Mg, Ga, Cr, Y, S and F). 3. Simulations containing a cation (Al, Ni, Mg, Ga, Cr and Y) and Sulfur. 4. Simulations containing a cation (Al, Ni, Mg, Ga, Cr and Y) and Fluorine. Further, in order to simplify the naming convention, first letter of the element's name is added after LMO. For example, Al doped structure is named as LMO-A. Similarly structures doped with Ni, Mg, Ga, Cr, Y, S and F will be named as, LMO-N, LMO-M, LMO-G, LMO-C, LMO-Y, LMO-S and LMO-F, respectively. For co-doped structures, first letter of the doped anion is added prior to the doped cation. For example, Al & S co-doped structure is named as LMO-SA. Similarly, we have LMO-SN, LMO-SM, LMO-SG, LMO-SC, and LMO-SY for Ni, Mg, Ga, Cr, and Y co-doped with Sulfur, respectively. Finally, co-doped structures with Fluorine are called LMO-FA, LMO-FN, LMO-FM, LMO-FG, LMO-FC, and LMO-FY, respectively. As summarized in Table 4.2, by replacing 5% of the Mn^{3+}, the

initial discharge capacity of the structure remains close to the undoped LMO spinel. However, there is a drastic drop in the theoretical discharge capacity with 10% of metal ions as dopants. This is due to the fact that with increased doping, the number of Mn^{4+} available for conversion into Mn^{3+} decreases since some of the Mn^{3+} positions are already filled with the doped metal ions.

Table 4.2: Maximum energy storage limit for various co-doped structures.

Structure	Maximum energy storage limit (mAh/g)	
LMO	148	
	5% Mn^{3+} replaced	10% Mn^{3+} replaced
LMO-SA	149	120
LMO-SN	147	117
LMO-SM	149	121
LMO-SY	146	116
LMO-SG	145	117
LMO-SC	139	118
LMO-FA	148	118
LMO-FN	147	116
LMO-FM	148	117
LMO-FY	146	114
LMO-FG	147	115
LMO-FC	148	116

4.3 Molecular Dynamics Modeling

Again, similar to previous chapters 2 and 3, MD simulations were setup using inter ionic pair interaction potential equation developed based on Gilbert-Ida-type pair interaction potential function as described in Equation 2.1.

For the MD simulations, the appropriate potential parameters to be employed with Equation 2.1 were either obtained from the literature or deduced if it was

not directly available in the literature [58, 59, 60, 61, 62]. Table 4.3 presents the parametric input values used for calculating the potential energy in this work.

Table 4.3: The parametric input values for various doping ions.

Doping ion	Z	a(Å)	b(Å)	References
Al^{3+}	+1.4	0.530	0.050	[58, 60]
Ni^{2+}	+1.4	0.700	0.059	[61]
Mg^{2+}	+1.4	0.720	0.060	[60]
Y^{3+}	+1.4	0.900	0.068	[59]
Ga^{3+}	+1.4	0.620	0.055	[63]
Cr^{3+}	+1.4	0.630	0.056	[61]
S^{2-}	−1.2	1.840	0.075	[62]
F^{-}	−1.2	1.330	0.072	[62]

As described in Equation 2.1, to calculate the inter-ionic potential between two ionic pairs, Gilbert-Ida-type pair interaction utilising Buckingham potential parameter format which is available in LAMMPS [64, 65], was used. Ewald method was used to compute the long-range coulombic forces [66]. Further, the isothermal isobaric (NPT) ensemble was performed for equilibration and production processes, and canonical ensemble (NVT) was utilised for the stress-strain computation. With NPT ensemble, the total number of ions, pressure and system temperature remain the same throughout the simulation. On the other hand, with the NVT ensemble, the system volume, temperature and total number of ions are kept constant. Further, in order to regulate the system at particular temperature, Nose–Hoover thermostat has been implemented [67].

A single cell of the LMO spinel has 56 locations in the cubical structure, occupied by certain types of elements [44, 45]. For example, 8 lithium ions can be placed at the 8a tetrahedral sites, manganese (Mn^{3+} or Mn^{4+}) or other

doped metal ions can take 16d octahedral positions, and O^{2-} or doped anions (S^{2-} or F^{-}) can be located at the 32e sites. The positions taken by these ions determine the potential energy of the crystal structure. The first step of the MD simulations is to equilibrate the setup. The crystal structures with the least potential energy have the highest probability to achieve equilibrium quickly. In order to find out the total number of potential configurations, we calculated the possible permutations of all scenarios. For example, when one Li^{+} ion is inserted in the cathode, there are 16 possible Mn^{3+} positions that a doping metal ion can take while there are 8 positions that Li^{+} ions could occupy, resulting in a total of 128 potential configurations. It has also been discussed in further detail in our previous publications [44, 45, 68]. Table 3.1 summarizes the total number of initial configurations that we need to equilibrate when just one Mn^{3+} is replaced by a metal doping element.

As seen in the Table 3.1, the number of potential configurations increases to millions with co-doping, when a doped anion can take any of the 56 positions. Therefore, evaluating the innumerable co-doped crystal structures and selecting the one with the least potential energy becomes computationally infeasible. This is particularly true for the intermediate charging states (SOCs between 0.500 and 0.875). Therefore, in order to reduced the computational time, neuro-computing techniques were used to identify the most feasible crystal structures that will have the least energy when equilibrated. To design such a neural network model, we evaluated 100,000 crystal structures, each with random initial configuration, using LAMMPS for 1 time-step. Using the data from these configurations, a neural network model was created that can explore millions of possible crystal

configurations and identify four configurations with the lowest potential energy, which were subsequently equilibrated. After equilibration, the MD production simulations for stress and diffusion calculations were performed as highlighted in our previous work [44, 45]. In the ensuing section, the neuro-computing model is described in detail.

4.4 Neural Network Modelling

Neural Network (NN) modeling is gaining popularity in almost every field. A NN model reads the input and output parameters from the sample or training data and deduces mathematical relationships between the input and output data for unknown cases. A typical NN architecture has several neurons as an input, neuron layers in the middle also known as "hidden layer", and output neurons. Number of neurons in the input, hidden, and the output layers need not be the same. In order to develop effective NN algorithms, there are the *weight* (w) factors or weightage and *biases* (B) assigned to each neuron layer. The value of these *weights* (w) and *biases* (B) are optimized using an appropriate algorithm and performance of the optimized NN is tested on a subset of the data. Generally, as input data propagates along the neural network, a profile is being generated which is amended based on the values assigned for biases and weights. These profiles are used to estimate the output values. The following equation shows the output generated for the neuron j in the hidden layer k

$$z_j^{(k)} = f^{(k)}\left(B_j^{(k)} + \sum_{i=1}^{n} z_i^{(k-1)} w_{ij}^{(k)}\right), \tag{4.1}$$

where z_i^{k-1} represents the output for the i^{th} neuron in the layer $(k-1)$, which has a maximum of n neurons. $w_{ij}^{(k)}$ is the weight factor of the j^{th} neuron using i^{th} input neuron in the $(k-1)$ hidden layer. Similarly, $B_j^{(k)}$ is the Bias value of the j^{th} neuron in layer (k). f^k represents the activation function, which receives the algebraic combination of z, w and B as an argument. Figure 4.1 shows the schematic of the output from a neuron, based on the above equation.

The transfer functions that are widely used comprise of the functions such as Rectified Linear Unit (ReLU), tanh, sigmoid, softmax etc. [69]. Compared to the other transfer functions, ReLU is easy to implement, offers quicker simulations and provides a consistent accuracy. Therefore, to avoid a longer training duration and yet retain better accuracy, we have used ReLU transfer function in this study [70, 71]. Specifically, the ReLU transfer function can be described by

$$f(x) = max(0, x), \tag{4.2}$$

where x represents the input argument as per Equation 4.1. Thus, as per the ReLU transfer function, only positive input values are allowed to pass to the next layer [70].

4.4.1 Database preparation:

Database for all the input parameters are prepared based on the results from the LAMMPS simulations. As shown in Table **??**, there are over 3 million possible crystal configurations when a single metal is used for doping. The possible cases increases to over 8 million with additional doping.

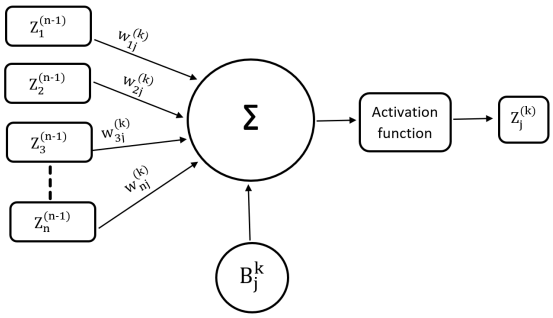

Figure 4.1: Schematic of a neuron in layer k with input from n neurons of the previous layer $k-1$.

In order to prepare the data, results from LAMMPS is arranged in the matrix form with ionic positions, and ionic properties such as radius, partial charge and compressibilty as the input parameters, with the corresponding potential energy as the output values. As shown in the Table 4.4, we generated 100,000 random cases for SOC $\in [0.500, 0.875]$ and trained the ANN model using 75% of this data, using the rest for testing. In this, we used all possible configurations and ran MD simulations for 1 timestep and selected 4 minimum potential energy structures for further molecular dynamics study. For the other SOC values, the number of potential configurations are not too many and so a brute force evaluation is possible without the need for a NN approach.

Table 4.4: The total possible ionic arrangements for various SOCs, and the number of randomized arrangements selected for NN training and testing in this study.

	Single Metal Doped Configurations for Different SOCs	
State of Charge	# of Possible Ionic arrangements	# Selected for NN Model Training and Testing
0.500	509,600	100,000
0.625	1,223,040	100,000
0.750	1,345,344	100,000
0.875	640,640	100,000

As part of model training, the values of weight and bias factors in the NN were determined by performing a grid search optimization (c.f. Table 4.5). For NN training, we employed the the *adaptive moment (adam)* algorithm [72] that offers a high level of accuracy and completes the training in a short time.

Table 4.5: Parametric values of inputs used during the grid search optimization.

	ANN Grid Search Parameters
Learning Rate (η)	10^k, $k = -1, -2, \cdots, 6$
Batch Size	2^k, $k = 1, 2, \cdots, 8$
Optimization Algorithm	Batch Gradient Descent, Adam, RMSProp
Activation Function	ReLU, Tanh, SoftMAX, Sigmoid

For any input data-set, the batch gradient descent optimization method uses the slope of a grid search parameter values such as the learning rate to obtain the optimum weights and bias values.

The Adam optimization algorithm is an extension to the batch gradient descent algorithm that is appropriate in handling large data-sets [72]. In this algorithm, the learning rate is maintained for each network weight, and adapted separately as the learning progresses. Further, this algorithm utilizes the first (m_t) and second (v_t) order moments of the predicted cost gradient in order to update the weights and biases. Adam optimization algorithm was applied to train our ANN models, with the values of the parameters employed being determined using a grid search (c.f. Table 4.6). As suggested by Kingma et al. [72], the values for the first (β_1) and second (β_2) order moment bias were fixed at 0.9 and 0.999, respectively.

As expected, the Adam algorithm was able to train the models accurately while using a higher learning rate which enhances the convergence rate [72]. Initial learning learning rate for the Adam algorithm was set to 1×10^{-3} (c.f. Table 4.6), which was automatically optimized through the iterations.

Table 4.6: Optimum values for the NN models derived from the grid search simulations

NN Model for SOC value	$0.500 - 0.875$
Parameters	
Learning Rate (η)	1×10^{-3}
Batch Size	8
Optimizer	Adam
Activation Function	ReLU

In order to avoid any pre-biases, all the values were initialized to zero before training any NN model. Also, prior to model training, the weights (w) were initialized using Glorot Uniform Initializer [73]. In this, to initialize the weights of neurons within each neuron layer, a uniform distribution, $U[a, b]$, was used, where a and b are the boundaries of the distribution function. Further, boundaries of the uniform distribution function for each neuron in the current layer were dependent on previous layer. For example, with n_{k-1} number of neurons in the $(k-1)$ hidden layer. Further, the initial parametric value of the weight factor for any neuron in the k^{th} hidden layer is obtained using following equation:

$$w_k \in U\left[-\frac{1}{\sqrt{n_{k-1}}}, \frac{1}{\sqrt{n_{k-1}}}\right]. \tag{4.3}$$

In order to find optimum parameters to train the NN, (R^2) value [74] is the major determining factor. Combinations of parametric values that offer the higher (R^2) score were given the preference. The value of (R^2) [74] was calculated for the NN using

$$R^2 = 1 \; - \; \frac{\sum_{i=1}^{N} (E_i - \hat{E}_i)^2}{\sum_{i=1}^{N} \left(E_i - \bar{E}\right)^2}, \tag{4.4}$$

in which

$$\bar{E} = \frac{\sum_{i=1}^{N} E_i}{N}, \tag{4.5}$$

where, N is the total data points or crystal arrangements utilized to validate the the model. Additionally, potential energy value for a specific crystal arrangement estimated by the NN is represented by, $\hat{E}_i$. Further E_i and $\bar{E}$ represent the potential energy and its average over all used crystal arrangements obtained through the MD simulations, respectively.

4.5 Quantum Mechanics Calculations

To get the input parameters for MD simulations and validate the structural results for engineered crystals for which experimental references are not available, QM calculations are performed. Figure 3.1, shows the $LiMn_2O_4$ single cell structure which consist of 8 Li, 16 Mn and 32 oxygen atoms.

In a doped crystal, some of the Mn^{3+} ions are replaced with metal ions in the input crystal structure. Similarly, in a co-doped crystal, in addition to Mn^{3+}, some of the O^{2-} ions are also replaced either by S^{2-} or F^{-}. For the QM

simulations, in order to account for the structural, vibrational, electronic and thermodynamic properties, Density Functional Theory (DFT) combined with the Hubbard+U model is implemented. To perform QM simulations, Quantum-Espresso [75], which is an open source software, has been utilized. Further, for the input files, it was assumed that the structure upholds the cubic symmetry through all points, including space groups for all calculations. Ultrasoft Pseudopotentials (USPP) type was used for input parameters such as lithium, manganese, and oxygen which uses the Vanderbilt code [76]. On the other hand, for the doping elements (cations and anions), Projector Augmented Wave (PAW) pseudopotential type was used [77]. For metal doping, in order to account for the spin-density, Perdew–Burke–Ernzerhof (PBE) form of the Generalized Gradient Approximation (σ-GGA) [78, 79] scheme is being utilized. Most of the QM parameter settings are similar to the ones described in Section 3.2.1.

4.6 Macroscale Computational Modeling

To evaluate the material properties at the macroscale, intercalation of lithium ions within the AMs could be modeled using mass transport equations inside the host material. The boundary conditions of the governing equations include the diffusion flux at the boundary which uses electrochemical reaction rate. In this case, the major force which moves lithium ions within the cathode structure is the electrochemical potential difference between the two electrodes. In order to model the movelent of lithium-ions at the macro scale along with diffusion induced stress and heat generation, Equations from 3.1 till 3.12 have been used. The only changes are the input values such as Young's modulus for co-doped

structures.

4.7 Results and Discussion

Findings from the multi scale modeling such as QM,MD, macro scale CFD along with the NN modeling are described and discussed in detail in this section.

4.7.1 NN simulations

NN models were used to simultaneously minimize the computational cost and maximize the accuracy. The NN models' results, their accuracy, and the required simulation time are presented in this subsection.

Prediction performance: A total of 4 NN models were developed in this study, one for each SOC value between 0.5 till 0.875. As mentioned in Section 4, these models were developed using 100,000 data points. While 75% of this data was used for training, the remaining was used for testing. To check each model's performance, coefficient of determination (R^2) score is calculated as described in the Equation 4.4. While a high R^2 indicates high accuracy, a score equal to or almost 1 is also not desirable as it could lead to over-fitting [80] and there loss of generalization [81]. The R^2 score for both training and testing data is presented in Table 4.7.

As seen in Table 4.7, for all 4 NN models, R^2 score for the training and testing data are in the range $[0.962, 0.986]$ and $[0.961, 0.984]$, respectively. This validates the accuracy of the developed models and also in consistent with our previous publication [68]. Figure 4.2 and 4.2 shows the comparison between the potential

Table 4.7: R^2 score for training and testing data for all 4 Neural Network models. The model number corresponds to the respective SOC dataset.

Model Number	SOC	Training R^2	Testing R^2
1	0.500	0.986	0.984
2	0.625	0.976	0.971
3	0.750	0.962	0.961
4	0.875	0.982	0.978

energies estimated by MD simulations and predictions from these NN models. In each plot in this figure, the solid line represents the ideal match between the NN models and the results from the MD simulations. With a strong confidence on the accuracy of the NN model emanating from these results, the NN model can be employed to rapidly evaluate all possible crystal configurations to identify the configurations with the least potential energy.

Pristine LMO spinel and some of the single ion doped structures can be validated with the experimental results, which was done by comparing the lattice constant values [82]. However, it becomes harder to get experimental data or perform tests for engineered co-doped structures. Therefore, we performed Quantum Mechanics simulations on the these configurations under similar environmental conditions and the results were used to verify the calculations from the MD simulations.

4.7.2 QM Simulations

Before using QM data for validation, it is essential to establish QM as a reliable tool to generate this data. For this, lattice constant values calculated through QM

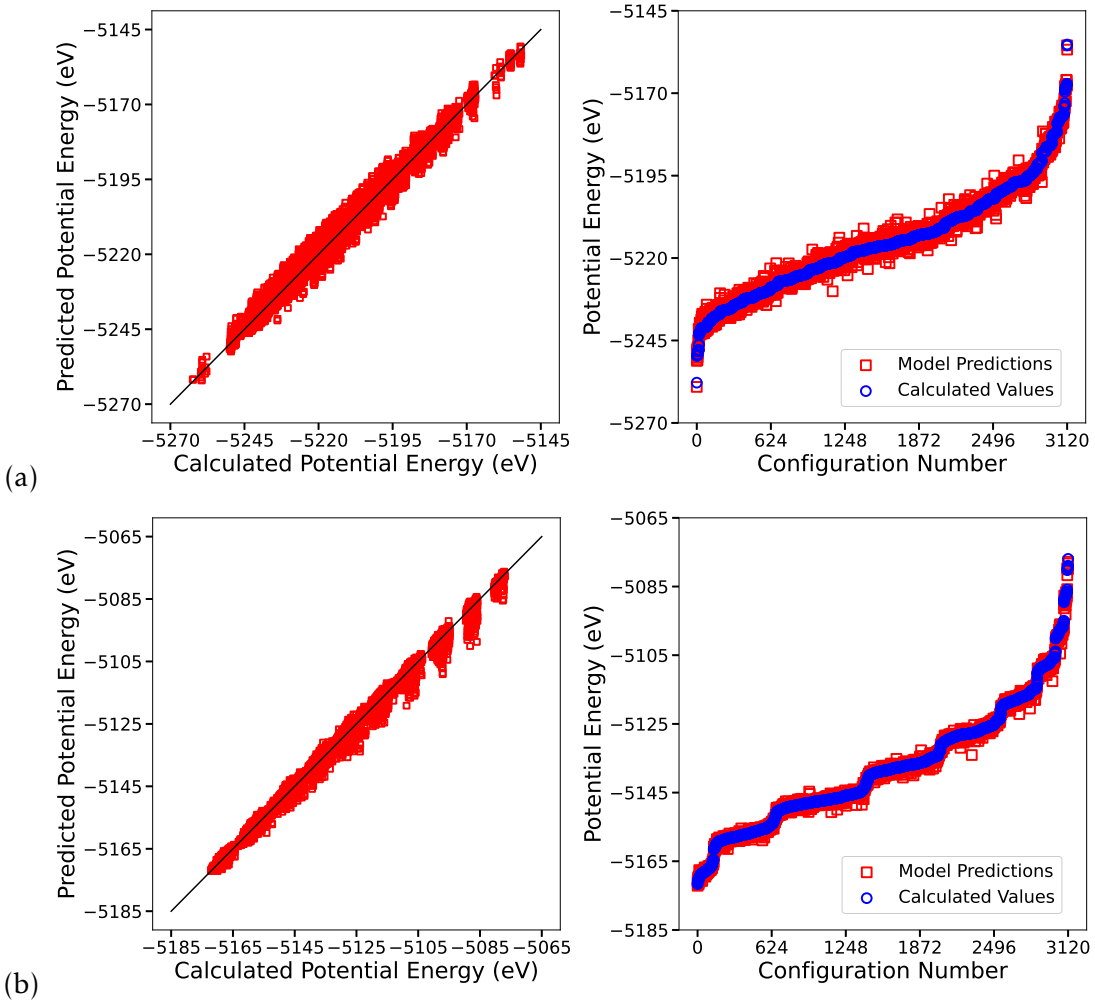

Figure 4.2: Model performance for SOC values of (a) 0.500 and (b) 0.625; **Left:** Potential energy values predicted by the NN model compared with the values obtained from LAMMPS; **Right:** Potential energy values from the NN model for each crystal configuration for this SOC.

simulations for the pristine LMO spinel were compared with the available experimental data. Table 4.8 shows that the lattice constant values calculated from QM simulation has an accuracy of ~99.92% with respect to the experimental data. Specifically, the lattice constant value for the pristine LMO spinel observed from experiments is 8.247 Å [83, 82] which is ~0.08% lower than the value from

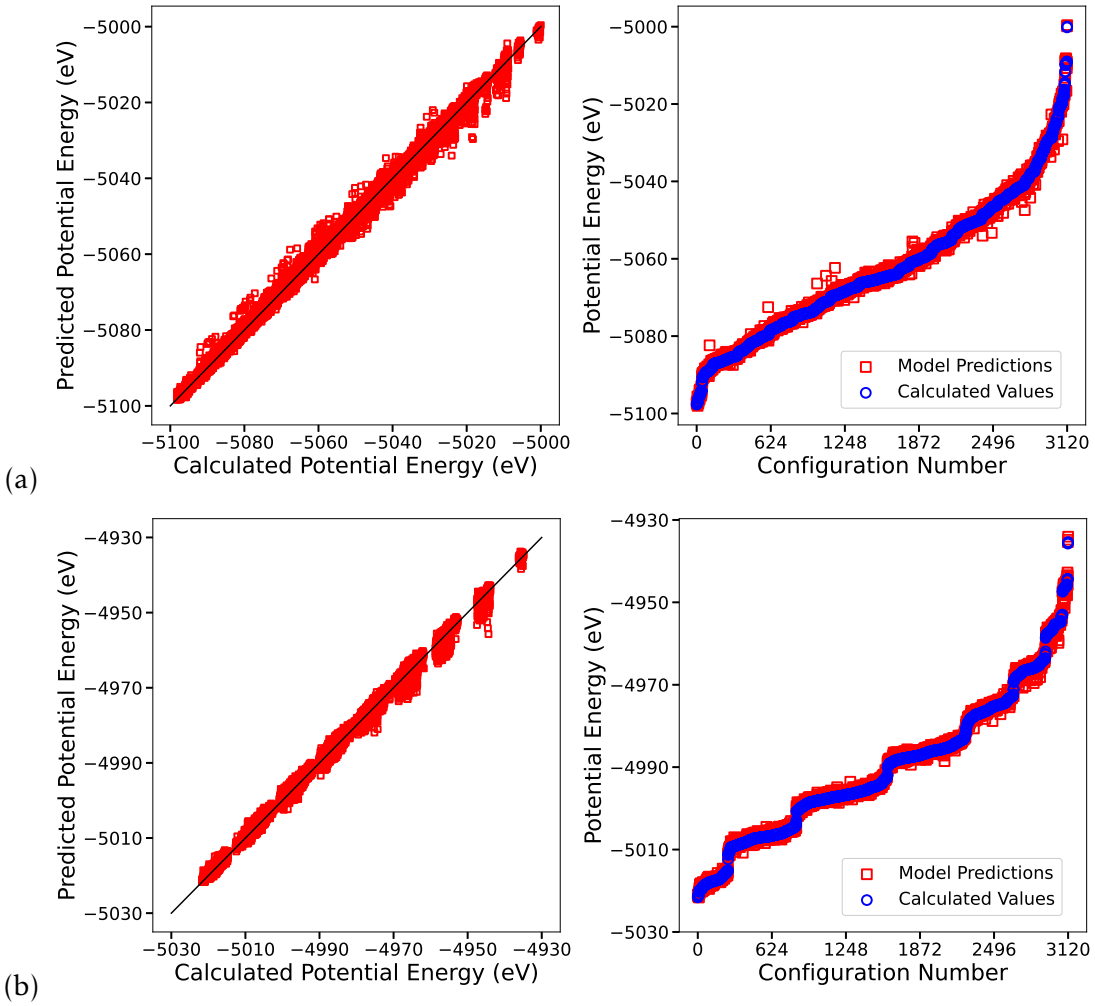

Figure 4.3: Model performance for SOC values of (a) 0.750; and (b) 0.875. **Left:** Potential energy values predicted by the NN model compared with the values obtained from LAMMPS; **Right:** Potential energy values from the NN model for each crystal configuration for this SOC.

the QM simulations (8.254 Å). With this confidence in the accuracy of the QM simulations, since we do not have measurements for the lattice constant values for the new engineered materials, especially when doped with more than one element, we have employed QM calculations to validate the lattice cell length results predicted by the MD simulations for the different materials.

4.7.3 The MD simulation

A detailed validation of the MD simulation framework used in this work has been presented in Refs. [44, 45] where we have compared the predicted diffusion coefficient as a function of temperature with the experimental data from Takai et al. [84] and Kuwata et al. [85]. For additional validation, we present the consistency of the lattice constant values for the undoped $Li_xMn_2O_4$ obtained from MD simulation, the experimental data as well as the QM simulation results. The first row in the Table 4.8 shows the comparison. It is clear from the results that lattice constant values from the MD simulations are fairly accurate and hence reliable. More precisely, the deviation is 0.23% with respect to QM results. Similarly, the MD simulation under-predicts the lattice constant by a mere 0.15% with respect to the experimental data from the literature [83, 82]. With these validations, we can confidently use MD simulations to investigate the doped and co-doped cases.

Table 4.8 presents a summary of the lattice cell length for each co-doped material investigated in this research using MD and QM simulations. As seen in this table, every doping element has a distinct effect on the lattice length that is dictated by its ionic radius and other parameters such as electronegativity, ionic compressibility, and oxidizing power. Barring Sulfur, most elements tend to reduce the overall lattice expansion. The anomalous behaviour of Sulfur is due to the fact that it has a relatively larger size which increases the size of the crystal. For each engineered structure, doped or co-doped, the lattice constant values obtained from both MD and QM simulations are in excellent agreement (c.f. Table 4.8). In fact, the largest disagreement of 1.3% is for LMO-SY. Also, in

Table 4.8: Lattice constant values from MD, QM simulations, and experiments for pristine and doped LMO spinel.

				% offset of MD results w.r.t.:	
Structure	MD (Å)	QM (Å)	Experiment (Å)	Experiment (%)	QM (%)
LMO	8.235	8.254	8.247 [83, 82]	0.15	-0.23
LMO-A	8.217	8.222 [51]			-0.06
LMO-N	8.220	8.238 [86]			-0.22
LMO-M	8.208	8.231 [87, 35, 88]			-0.28
LMO-Y	8.216	8.220			-0.05
LMO-G	8.219	8.227	–	–	-0.10
LMO-C	8.220	8.229	–	–	-0.11
LMO-F	8.223	8.231	–	–	-0.10
LMO-S	8.237	8.239			-0.02
LMO-SA	8.222	8.146			+0.93
LMO-SN	8.223	8.209			+0.17
LMO-SM	8.212	8.216			-0.05
LMO-SY	8.219	8.325			-1.27
LMO-SG	8.224	8.229	–	–	-0.06
LMO-SC	8.225	8.228	–	–	-0.04
LMO-FA	8.218	8.138	–	–	+0.98
LMO-FN	8.219	8.200	–	–	+0.23
LMO-FM	8.211	8.215	–	–	-0.05
LMO-FY	8.216	8.234	–	–	-0.22
LMO-FG	8.220	8.227	–	–	-0.09
LMO-FC	8.223	8.227	–	–	-0.05

general, as highlighted in the previous section, the MD simulation tends to under-predict the lattice constant values. The only exceptions are LMO-SA and LMO-SN structures. Nevertheless, these variations are very small and could be attributed to the mathematical deviations that arise from the MD simulation's equilibrium state termination time, and for all practical purposes, these variations are negligible.

4.7.4 Effect of doping and co-doping

In this subsection, we present the findings on the effect of doping and co-doping on the different crystals.

Volume expansion:

The expansion of the cathode material upon lithium ion intercalation when the battery is discharging is a well known phenomena and is directly reflected in the lattice constant. One of the major objectives behind co-doping was to reduce this volume expansion. It is evident from the Figure 4.4 that for all engineered structures, the lattice constant is directly proportional to the state of charge of the battery. At a given SOC value, the lattice constant of the pristine LMO spinel is higher than all engineered structures except when Sulfur is introduced.

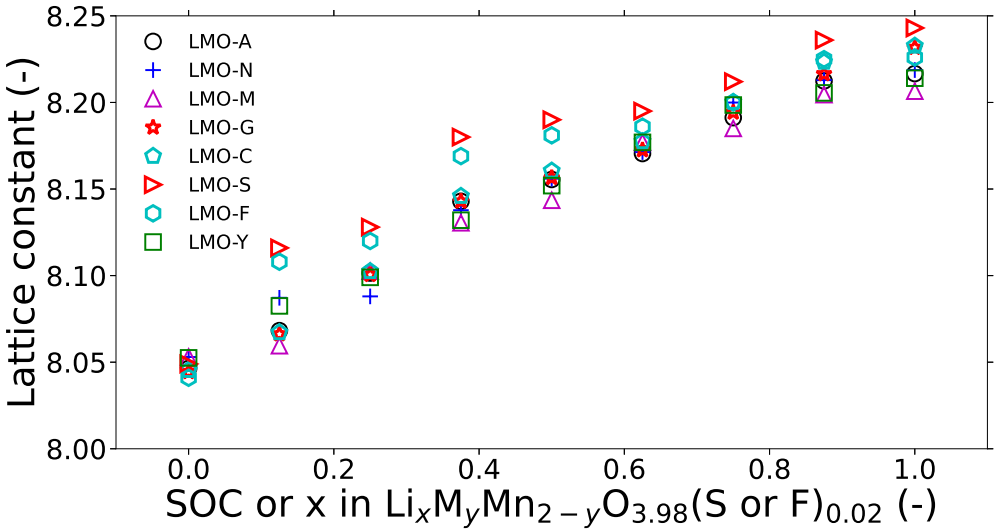

Figure 4.4: Lattice length expansion for each doping elements cases.

More precisely, from Figures 4.4, 4.5 and 4.6, we can concluded that for all doped as well as co-doped $Li_xMn_2O_4$, the overall lattice length of the structure increases from 8.038Å to 8.237Å during lithium intercalation. Table 4.9 summarizes the relative lattice length and volume expansion for the all the structures which includes prestine LMO spinel, single and double element doping. As seen in this table, all cathode crystals go through a volume change of as high

as 7% through a complete charge discharge cycle. Further, with the exception of LMO-S crystal, relative to the LMO spinel, the volume expansion of doped and co-doped crystals decrease by 1.7% – 20%. As suggested by by Nishijima et al. [41], these reductions in the volume expansion of the doped and co-doped crystals with respect to LMO spinel can translate to an increase in the battery's life by several thousands of cycles.

Table 4.9: Impact of dopants on the volume expansion and the cycle life of the battery.

Structure	Change in length (%)	Change in volume (%)	Change in volume w.r.t. LMO (%)	Young's Modulus (GPa)	Potential increase in # of cycles
LMO	+2.350	+6.87	-	132	-
LMO-A	+2.072	+6.09	-11.32	118	+4134
LMO-N	+2.016	+5.93	-13.71	123	+5007
LMO-M	+1.870	+5.50	-19.95	117	+7283
LMO-G	+2.275	+6.69	-2.65	119	+968
LMO-C	+2.275	+6.69	-2.65	125	+972
LMO-Y	+1.966	+5.78	-15.85	122	+5788
LMO-S	+2.354	+6.92	+0.72	128	-262
LMO-F	+2.249	+6.61	-3.75	117	+1371
LMO-SA	+2.071	+6.08	-11.50	118	+4570
LMO-SN	+2.015	+5.92	-13.82	125	+5353
LMO-SM	+1.869	+5.50	-19.94	128	+7718
LMO-SG	+2.288	+6.72	-2.16	113	+787
LMO-SC	+2.288	+6.73	-2.17	127	+790
LMO-SY	+1.965	+5.78	-15.86	128	+6093
LMO-FA	+2.092	+6.15	-10.48	117	+4878
LMO-FN	+2.054	+6.04	-12.10	122	+3999
LMO-FM	+1.904	+5.60	-18.53	121	+7170
LMO-FG	+2.296	+6.75	-1.73	114	+631
LMO-FC	+2.298	+6.76	-1.67	122	+608
LMO-FY	+1.998	+5.88	-14.48	123	+5560

The Young's modulus values at room temperature for the fully lithiated structures show that for some of the co-doped cases such as LMO-SM and LMO-SY, the compromise in the structural strength is marginal (c.f. Table 4.9). As highlighted in the Introduction section, it must be noted that S and F co-doped structures tend to perform better in terms of relative volume expansion and manganese dissolution during charge and discharge cycles at elevated temperatures.

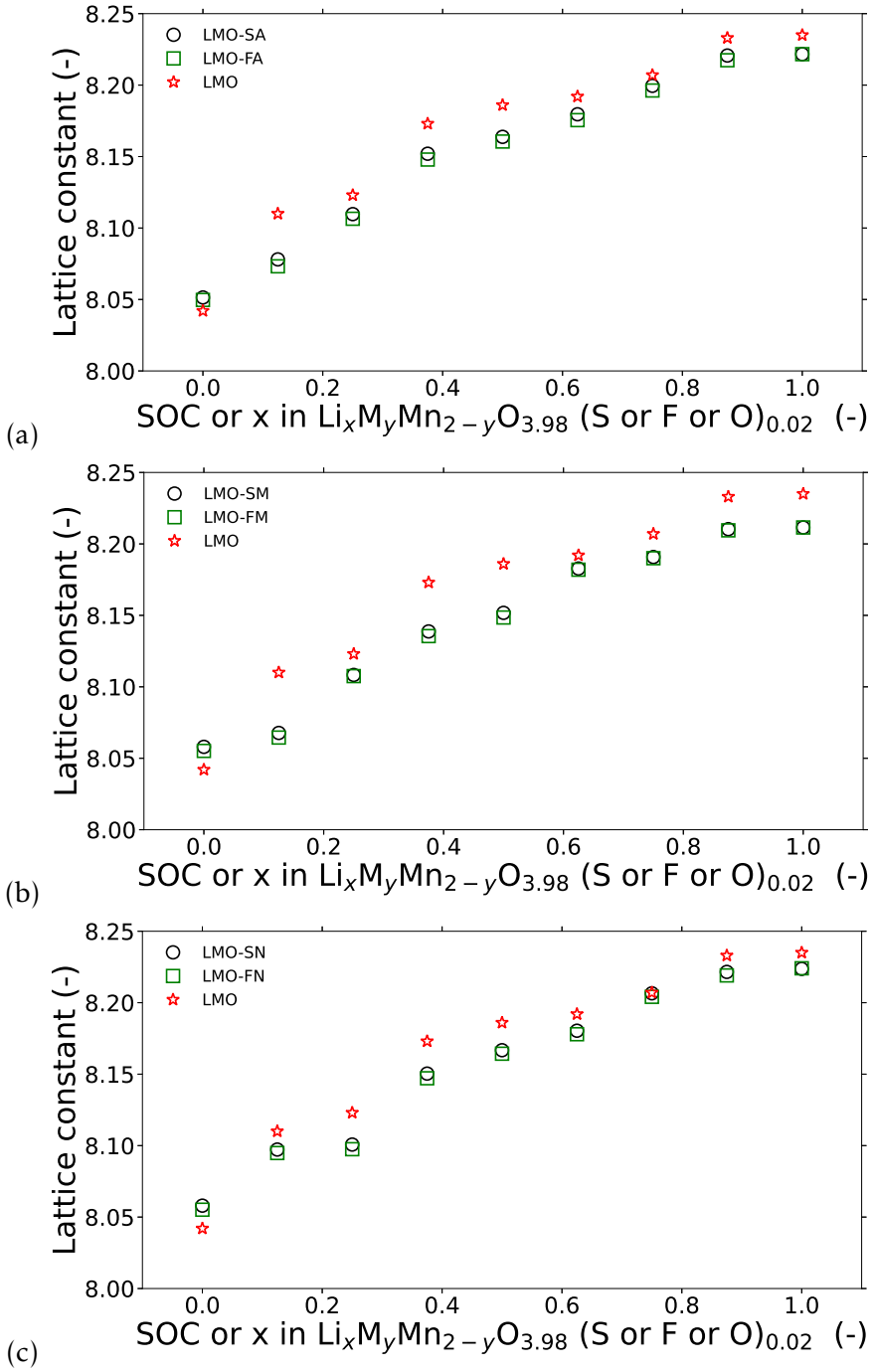

Figure 4.5: Change in lattice length at various SOC for undoped structures, and structures co-doped with S or F, and (a) Al, (b) Mg and (c) Ni.

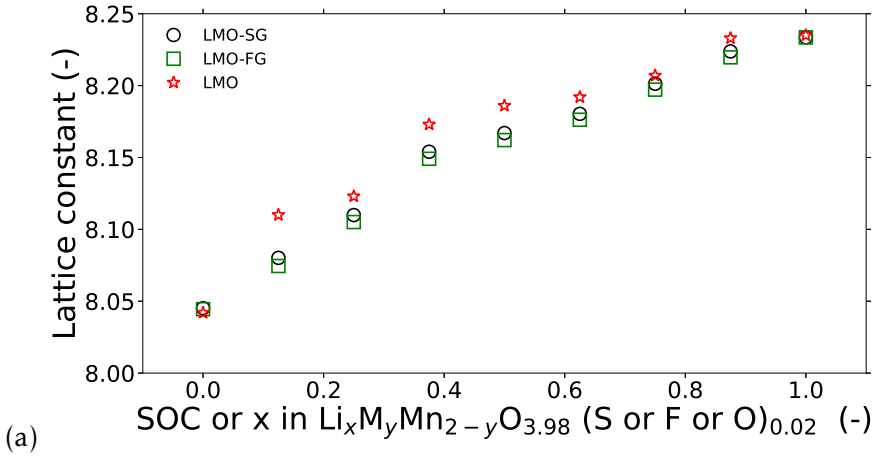

(a)

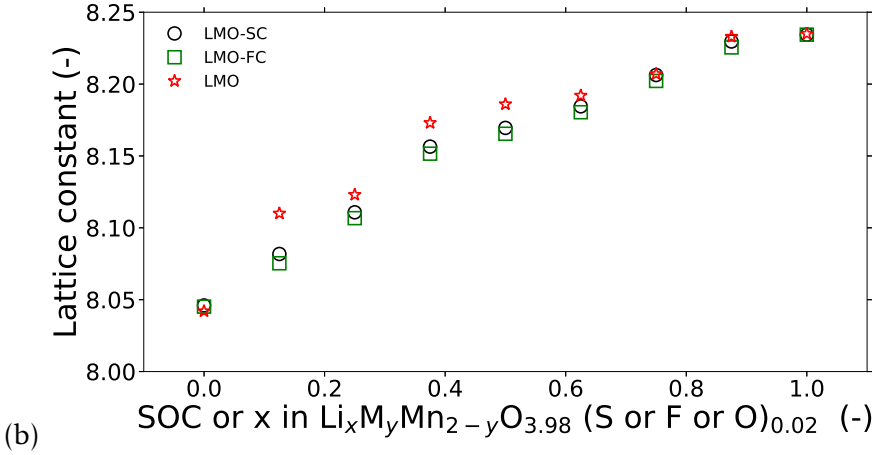

(b)

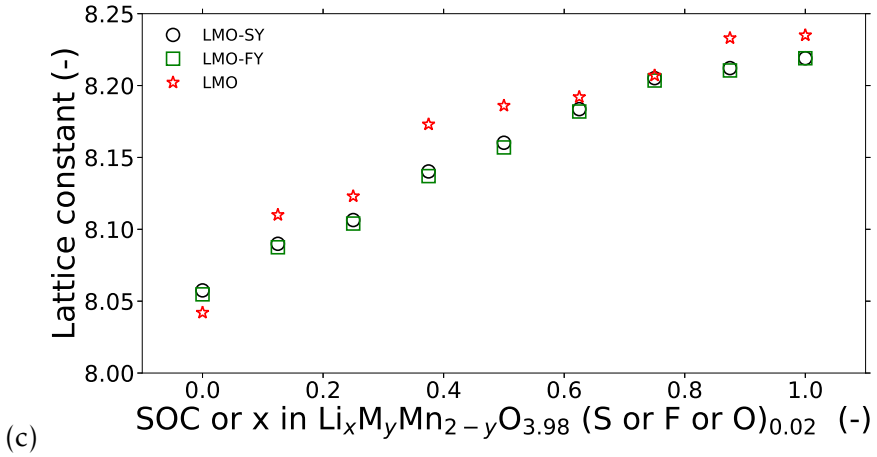

(c)

Figure 4.6: Change in lattice length at various SOC for undoped structures, and structures co-doped with S or F, and (a) Ga, (b) Cr and (c) Y.

Yield and ultimate stress:

In our previous work on the $LiMn_2O_4$ spinel, we observed that the state of charge and temperature are the key parameters to test the material properties [44]. We investigated the effect of these parameters for different strain rates [44]. We also found out [44] that the crystal structure of the cathode material is a direct function of the charged or discharged state of the battery, which is in agreement with the work of Vakarin et. al. [89]. Based on these observations, we have investigated the stress-strain relationship for a strain rate of 0.5C (0.01 p/s) for fully and partially lithiated structures co-doped with Sulfur or Fluorine.

Lee et al. [90] found that ionic interactions contribute immensely to the stress generation in the crystal structure, especially during intercalation. The introduction of the Li^+ into the host material during charging and discharging is responsible for changing the number of ions in the crystal (Li^+, Mn^{3+}, Mn^{4+}, and ions of other dopants). As per Equation 2.1, this eventually impacts the overall interactions between the ions and thereby the mechanical properties of the electrode material [90]. It also means that the SOC values not only influence the elastic properties of the undoped LMO spinel but also impact the doped and co-doped structures. To understand the fracture behaviour of each material, we applied a uniaxial strain which is equivalent of C/2 charge/discharge rate, on two sides of the crystal boundaries. Figure 4.7 and 4.8 presents the results for stress and strain values for the various structures co-doped with Sulfur and Fluorine. As seen in this figure, LMO spinels doped with Ga, Ni or Mg tend to miss the ultimate stress part of the curve. However, based on the Young's modulus values summarized in Table 4.9, we can conclude that the yield stress

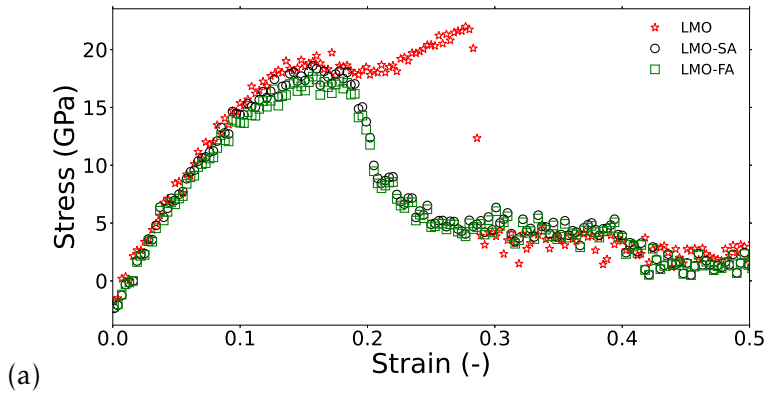

(a)

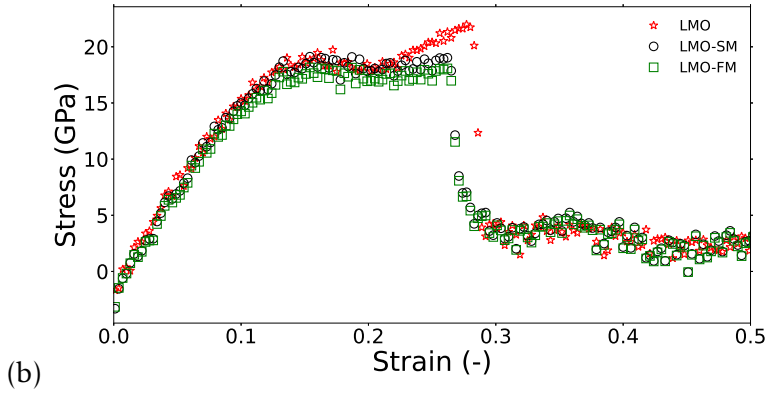

(b)

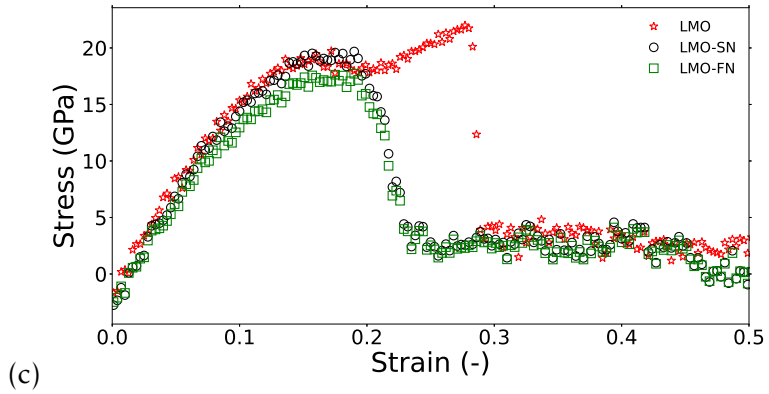

(c)

FIGURE 4.7: Stress-strain curves for an undoped structure and structures co-doped with Sulfur or Fluorine at SOC=1: and doped with (a) Al, (b) Mg and (c) Ni.

values for most of the cases will overlap with each other.

Intermediate stage elastic properties:

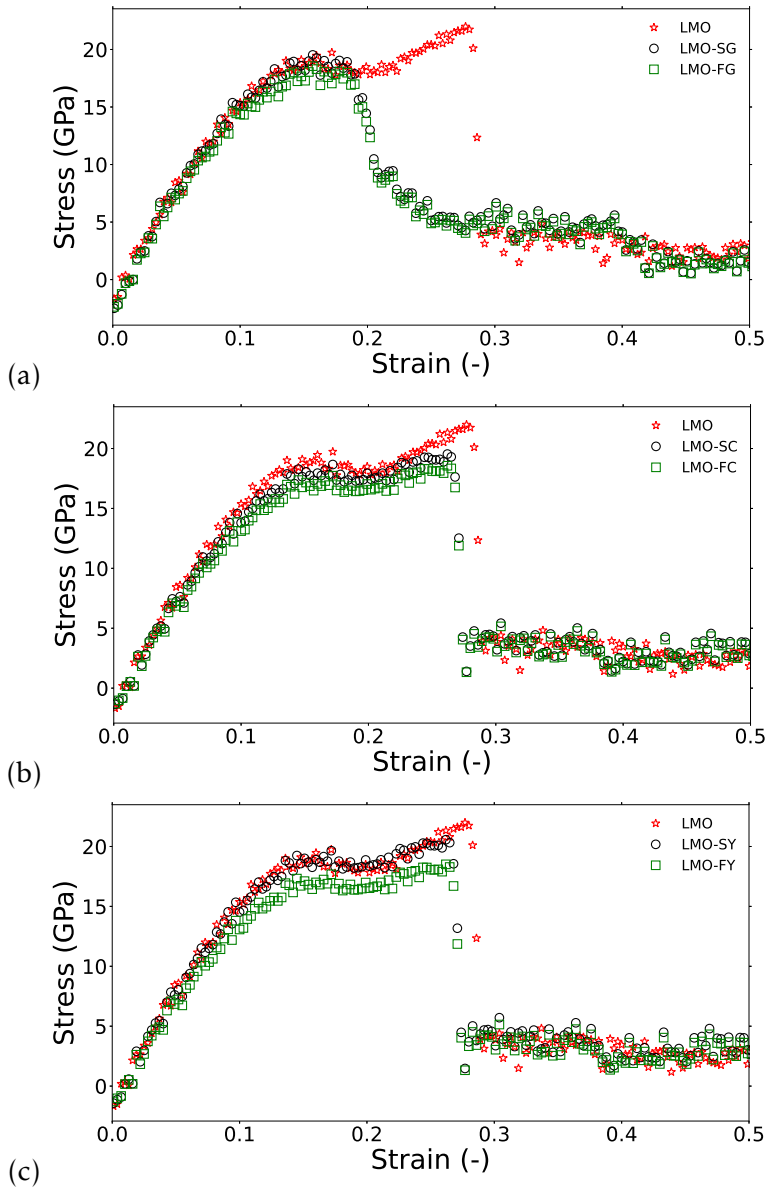

Figure 4.8: Stress-strain curves for an undoped structure and structures co-doped with Sulfur or Fluorine at SOC=1: and doped with (a) Ga, (b) Cr and (c) Y.

It is possible that co-doped material shows promising results when fully charged [44, 45]. However, the material may not be stable in the partially charged states. At lower SOCs, the LMO spinel could be more unstable. To investigate this,

we have compared the results for both Sulfur and Fluorine co-doped structures with undoped LMO spinel at SCO=0.125. The results are shown in the Figures 4.9-4.12.

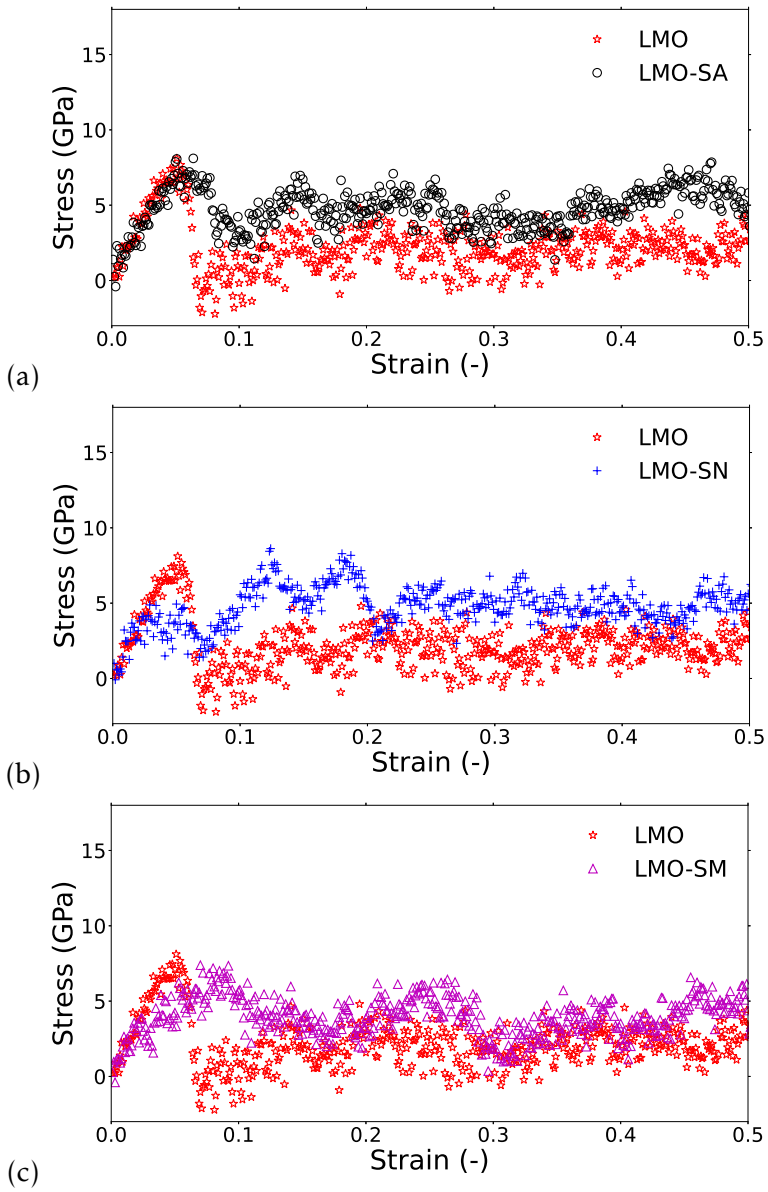

Figure 4.9: Elastic behaviour of various co-doped structures at SOC=0.125 with respect to original LMO structure; Doping elements are (a) S and Al, (b) S and Ni (c) S and Mg.

As shown in Figure 4.9 (b) and (c), compared to the undoped LMO spinel, structures doped with Ni and Mg tend to have a lower yield stress. Specifically, LMO-SN, LMO-SM and LMO have yield stress values of 4.9GPa, 7.4GPa and 8.1GPa, respectively. In case of Ni co-doped structures, the material fractures quite early at a strain of around 0.03. On the other hand, materials doped with Chromium (LMO-SC, LMO-FC) and Yttrium (LMO-SY and LMO-FY) outperform the pristine LMO spinel's crystal structure (c.f. Figure 4.10 (b), 4.10 (c), 4.12 (b) and 4.12 (c)).

It must also be noted that doping with either Sulfur or Fluorine produces almost the same results. This is expected because: (i) the input parameters corresponding to these two dopants are very close, and (ii) only 1% of the oxygen ions are replaced, resulting in a very small contribution from the corresponding ionic interactions.

Diffusion coefficient:

It is well known that with an increase in the ambient temperature, the enhanced kinetic energy (KE) increases the total energy of the system. This results in an increased ionic mobility within the crystal structure, eventually increasing the diffusivity of the lithium ions inside the crystal structure. Further, as evident in the Equation , contribution from the chemical diffusion coefficient, dictated by the battery's charging state, operating temperature, and the doping elements, is also equally important:

$$D_{Li^+}(c_{Li^+}) = D_0 c_{Li^+}(1 - c_{Li^+})\left(-\frac{zF}{RT}\frac{\partial V(c_{Li^+})}{\partial c_{Li^+}} + \frac{2v^2 Y c_{max}}{9RT(1-\nu)}\right), \tag{4.6}$$

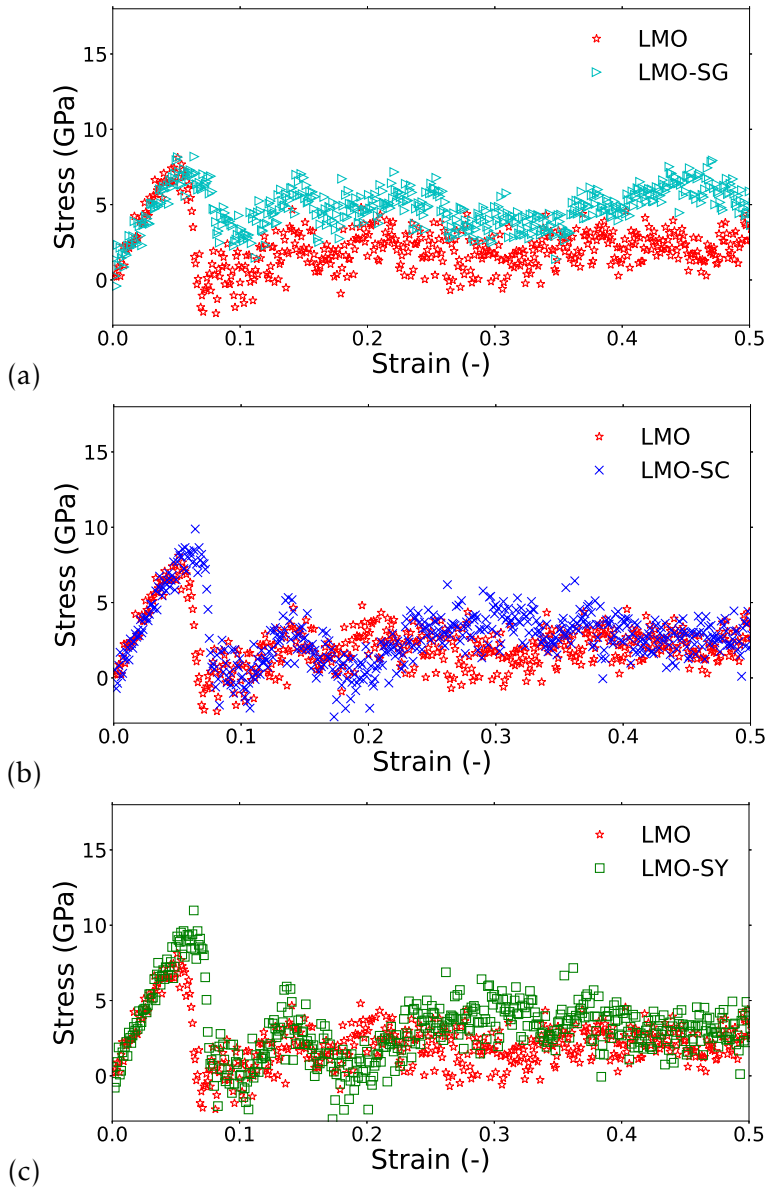

Figure 4.10: Elastic behaviour of various co-doped structures at SOC=0.125 with respect to the original LMO structure; Doping elements are (a) S and Ga, (b) S and Cr, and (c) S and Y.

where D_0 is the initial diffusion coefficient, and c_{Li^+} is the concentration of the lithium ions. Further, z, is the ionic charge of lithium, and V is the voltage or potential at particular lithium concentration. v, and c_{max}, are the partial

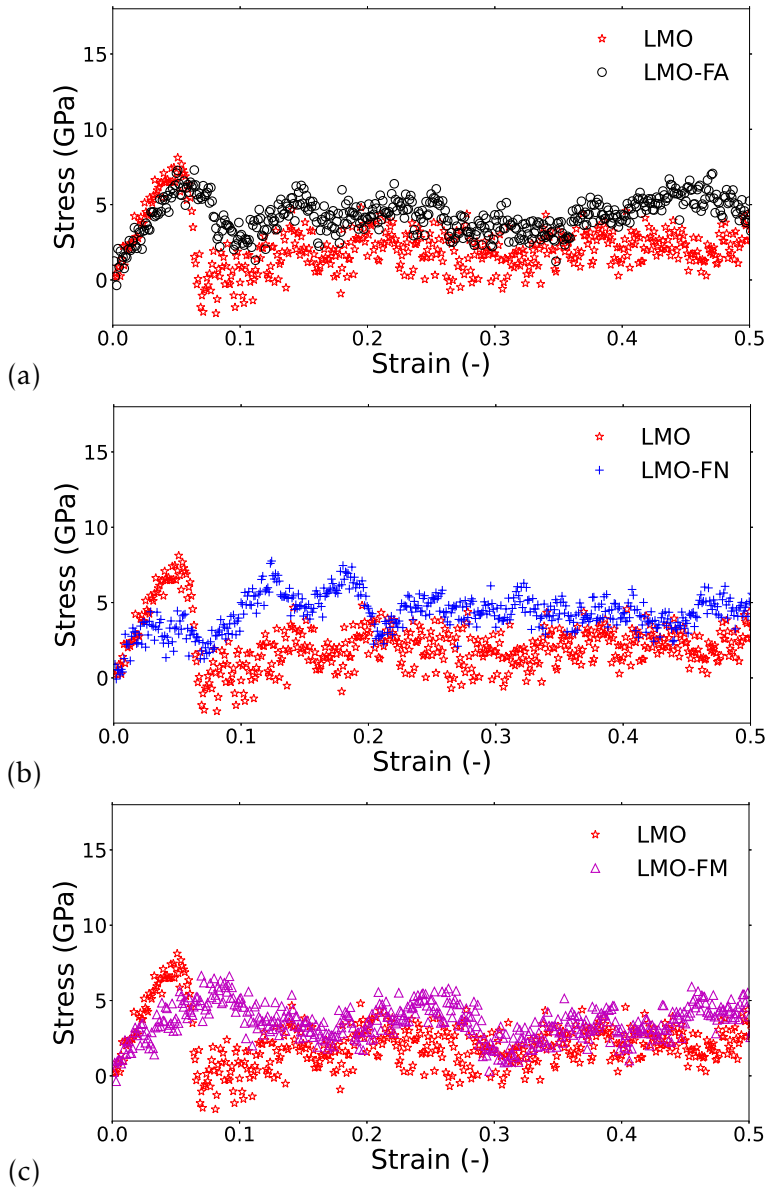

Figure 4.11: Elastic behaviour of various co-doped structures at SOC=0.125 with respect to the original LMO spinel structure; Doping elements are (a) F and Al, (b) F and Ni (c) F and Mg.

molar volume and maximum concentration of the lithium ions, and Y and ν, represent the Young's modulus and Poisson's ratio of the material, respectively. Equation 4.6 accounts for the intercalation induced diffusion for lithium ions,

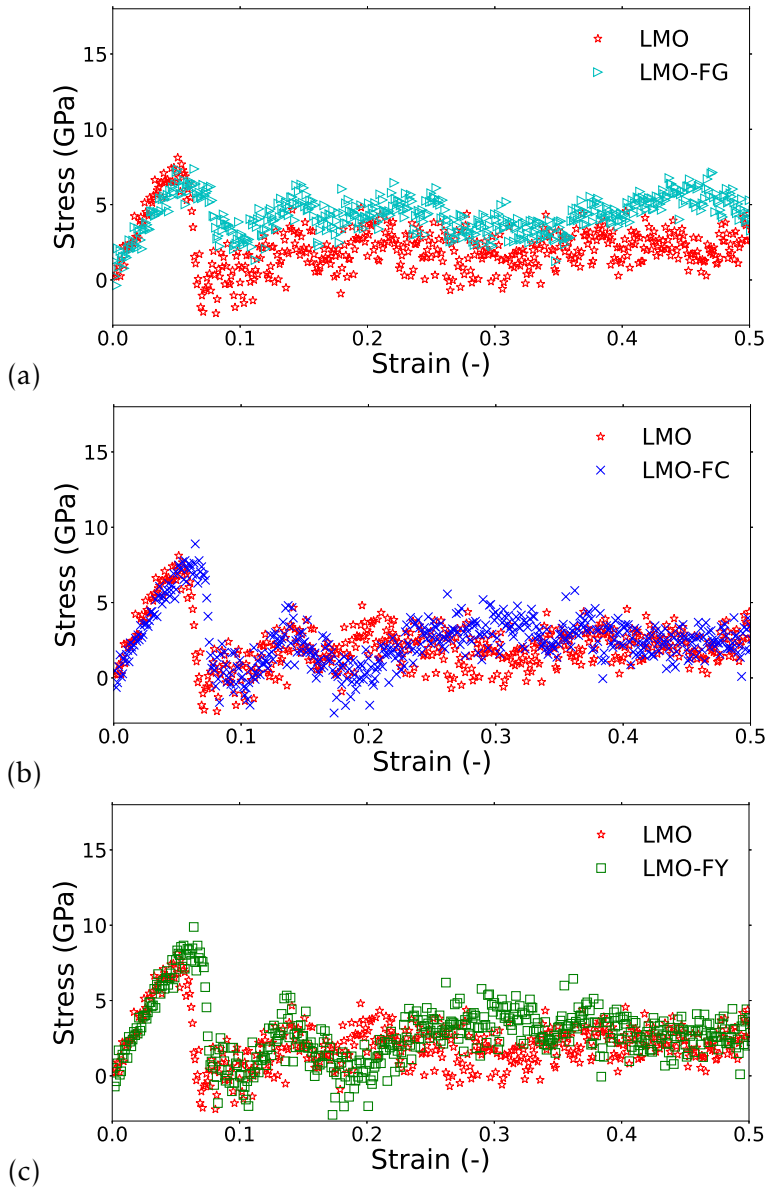

Figure 4.12: Elastic behaviour of various co-doped structures at SOC=0.125 with respect to the original LMO spinel structure; Doping elements are (a) F and Ga, (b) F and Cr, and (c) F and Y.

and can be used to validate the results from our simulations [25, 26, 91, 90].

MD simulations were undertaken to investigate the impact of the doping and co-doping on the diffusivity of the lithium ions at different temperatures. To

estimate the diffusion coefficient, Mean Square Displacement (MSD) values of the lithium ions were calculated using the Equation 4.7. MSD of the lithium ions was evaluated based on the average change in the positions of the lithium ions with time with respect to its original position.

$$MSD_{Li^+}(time) = \overline{|x(time) - x(time_{initial})|^2}, \tag{4.7}$$

where $x(time)$ and $x(time_{initial})$ represent the ionic positions of the lithium ions at two different times. Further, the bar on top of the square displacement value in Equation 4.7 suggests that we have averaged the values for one ion type, particularly lithium ion in this work. Using this averaged mean square displacement data, we have employed the following Einstein equation to calculate the diffusion coefficient:

$$D_{Li^+} = \frac{1}{6} \lim_{t \to \infty} \frac{d}{dt} MSD_{Li^+}. \tag{4.8}$$

In this equation, as time approaches infinity, the slope of the MSD with time represents the diffusion coefficient.

In the high temperature zone ($T > 1000$K), the MSD slopes can be accurately determined after a short simulation duration [44, 45]. However, at lower temperatures, this becomes harder since the ions require more time to diffuse. Therefore, at lower temperatures, we create an impurity by removing an ion and run the simulation for 5ns. Since vacancy was already created, the results from these simulations provide us the energy required to move an ion when there is a vacant site available. The activation energy from this calculation is added to the

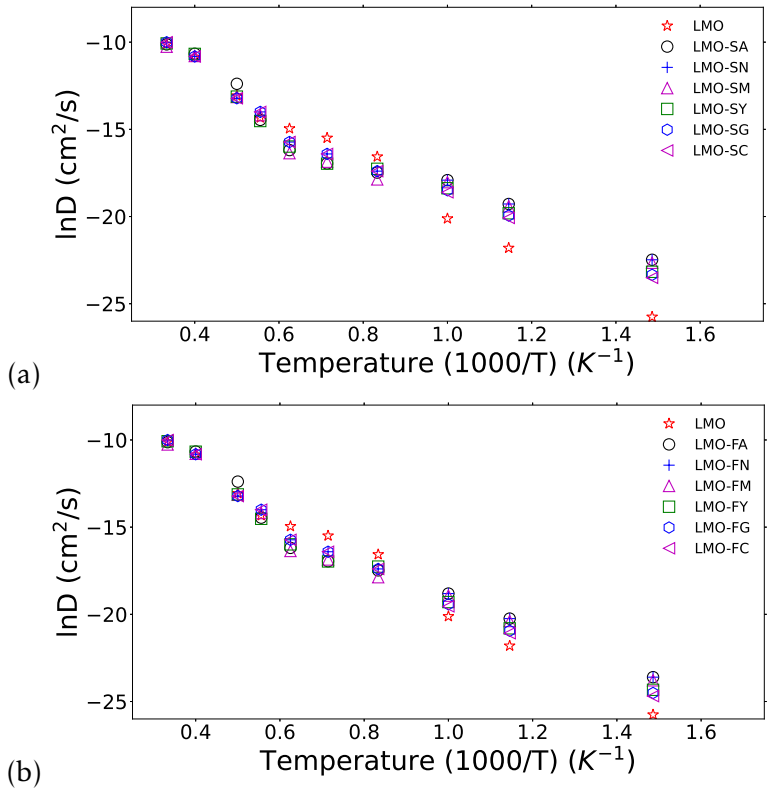

Figure 4.13: Diffusion coefficient vs temperature for various engineered structures in a fully discharged state. (a) Structures co-doped with Sulfur, and (b) structures co-doped with Fluorine.

vacancy formation activation energy from higher temperature zones. Kuwata et al. [85] have used this approach in their experimental work and we have used their data to validate this process [45]. Our simulation results for LMO spinel are in excellent agreement with their experimental data, and in agreement with Chung et al. [92], outperform Kuwata et al.'s [85] extrapolation for room temperature diffusion coefficient.

Continuing this computational investigation on diffusion in coped and co-doped crystals, we found that almost all co-doped structures outperform the undoped LMO spinel, especially at lower temperature (c.f. Figure 4.13 (a) and

(b)). However, an improvement in the diffusivity is better for materials doped with Sulfur instead of Fluorine. This is because doping with Sulfur results in a larger lattice size, facilitating the easy movement of the lithium ions, especially at lower temperatures. In the high temperature zone there is hardly any difference because a small change in the lattice size does not have any additional effect since the structure has already gone through a phase change.

4.7.5 Inter-Ionic distance

Ionic interactions can be studied to understand the strength of the crystal structure. In general, ions with smaller distance have a stronger bond, providing a better structural strength. To investigate this, average inter-ionic distances between different ions were calculated using MD simulations. For this, the radial distribution function (RDF), $G(r)$, production simulations were performed on the equilibrated structures of the doped as well as undoped LMO spinels. The output of the MD simulations provide us the x, y and z coordinates for the requested ionic pair within a defined cutoff radius. $G(r)$ is calculated using Equation 3.15.

Figure 4.14 shows the radial distribution function of the undoped LMO spinel along with Sulfur co-doped structures, at room temperature. In each plot, the first peak represents the distance between the metal dopant and the nearest oxygen ion, i.e., the bond length. As shown in Figure 4.14, compared to undoped LMO spinel where Mn^{3+} forms a bond with O^{2-} (bond length of about 2Å), almost all co-doped structures have a smaller inter-ionic distance. Doping with Al and Ga results in the smallest ionic distance of ~1.55Å and ~1.65Å,

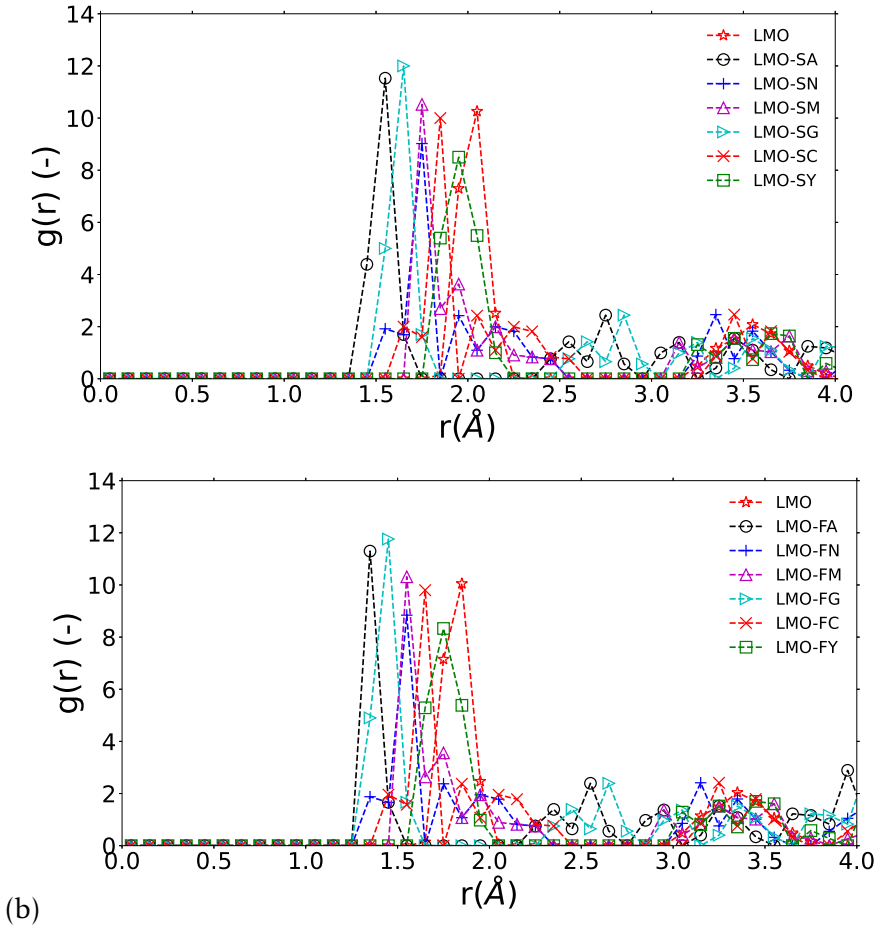

(b)

FIGURE 4.14: Inter-ionic distance between O^{2-} and other doped metal ions for various structures at SOC=1 for (a) Sulfur and (b) Fluorine, co-doped structures.

respectively. Though Al^{3+}-O^{2-} has the smallest bond length, the yield strength values for all the Al doped and co-doped structures, especially at intermediate charging states, was slightly lower than the yield strength of materials with other dopants such as Y, Cr (c.f. Figure 4.14(a) and (b)).

This is because with Al, the contribution towards smaller ionic distance is attributed to smaller radii of the Al ion (0.53Å). Figure 4.9 (a) and (b) are almost identical because both figures represent the ionic distance between a

Table 4.10: Average Bond length between O^{2-} and other doped metal ions (in Å)

Bond name	Sulfur co-doped	Fluorine co-doped
Ni-O	1.75	1.65
Mg-O	1.75	1.65
Al-O	1.55	1.45
Y-O	1.95	1.85
Mn-O	2.05	2.00
Ga-O	1.65	1.55
Cr-O	1.85	1.75

doped metal ion and oxygen, with just a variation in the co-dopant (Sulfur or Fluorine). Further, Table 4.10 shows the average bond length between metal and oxygen ions for structures co-doped with Sulfur or Fluorine. Fluorine co-doped structures shows minor reduction on the overall bond length which is probably due to the smaller lattice structure and higher electronegativity of the Fluorine ion as compared to Sulfur.

4.7.6 Multi-scale simulation results

The QM and MD simulations have established that trace co-doping with appropriate ions can enhance the structural properties as well as the charge/discharge cycles of $Li_xMn_2O_4$. Further, removing a small amount of Mn^{3+} can help retard the material degradation which occurs after charge and discharge processes, especially when the ambient temperature is high. With these promising results at atomic and molecular scale, in order to verify these finding at larger scale, Spherical Particle Model (SPM) simulations were performed. To improve the

quality of the employed input parameters, important inputs such as diffusion coefficient and the Young's modulus are acquired from our QM and MD simulations. These values along with the right boundary conditions are used for macro-scale simulations to investigate the possibility of thermal runway due to large internal stress generation in the co-doped materials. Specifically, we looked at the development of the stress or heat generation in all the novel cathode structures.

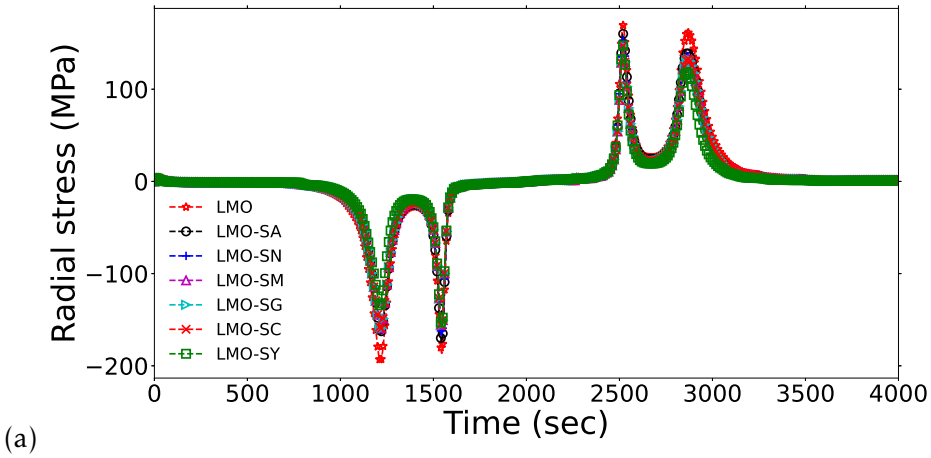

(a)

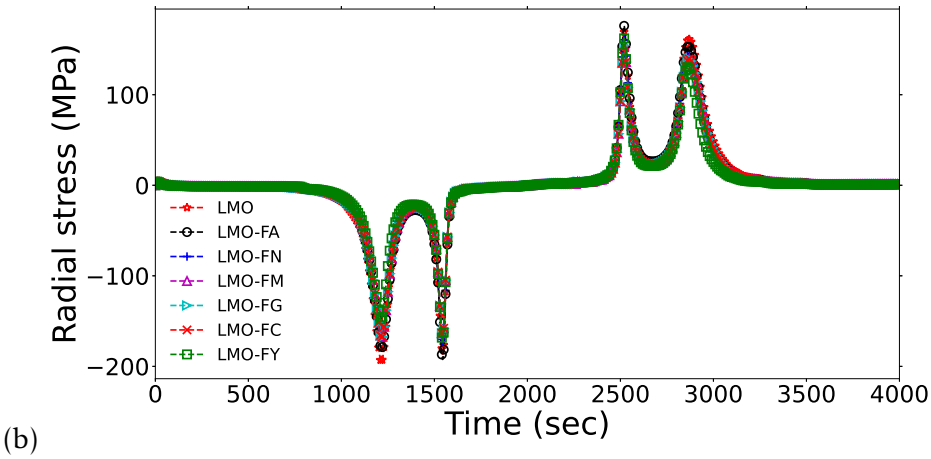

(b)

FIGURE 4.15: Radial stress generated during a charge-discharge cycle for structures co-doped with: (a) Sulfur, and (b) Fluorine.

Figure 4.15 presents the development of the radial stress inside the spherical

Table 4.11: Peak radial stress ranges for Sulfur and Fluorine co-doped structures

	Peak stresses (MPa)			
	Min	Max	Min	Max
Undoped	-195.08	169.43	-	-
Doped element	Sulfur co-doped		Fluorine co-doped	
Al	-174.86	+160.07	-192.34	+176.07
Ni	-167.98	+153.11	-176.38	+160.77
Mg	-160.44	+147.20	-168.46	+154.55
Ga	-144.40	+132.48	-158.84	+145.72
Cr	-173.76	+162.67	-191.14	+178.94
Y	-157.97	+147.88	-173.76	+162.67

particle of the novel cathode materials structure during normal charging and discharging processes. As expected, for trace amounts of co-doping with metal ions, the peaks in the radial stress generation are almost identical. However, as seen in Table 4.11, there is only a small variation in the peak stress value. In some cases, co-doped LMO spinels offer less internal stress as compared to LMO spinel without any doping. Some of the peaks with LMO-FA are slightly taller due to smaller crystal volume. LMO spinels doped with Yttrium or Chromium, and co-doped with either Sulfur or Fluorine, show a much smaller radial stress since these crystals' volume undergo a balanced expansion during the lithiation and de-lithiation processes.

Depending upon the SOC values, a diffusion induced radial stress could result in a variety of heat generation profiles within the crystal during intercalation process. As shown in the Figure 4.16, during cell charging cycle, there are a few peaks and most of them are at the same charging time or SOC. Peak values for both Sulfur and Fluorine co-doped structures are shown in the Table 4.12. It

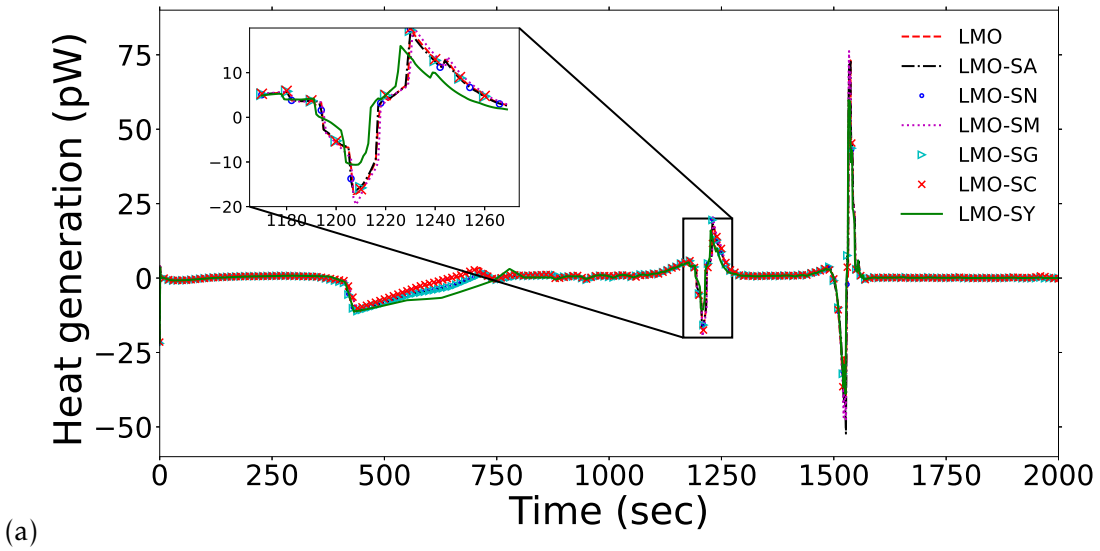

(a)

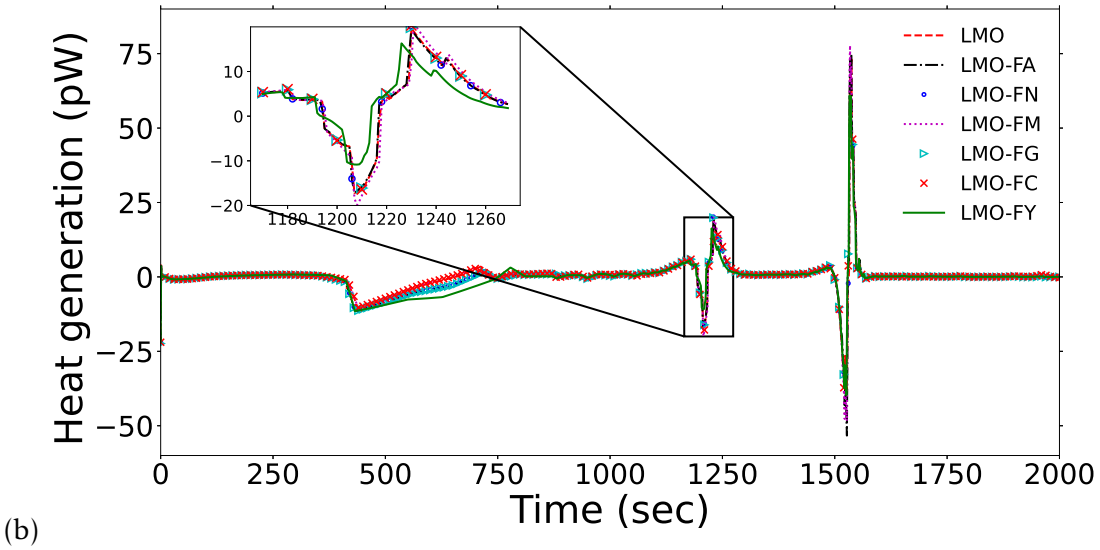

(b)

Figure 4.16: Heat generated during a charging cycle for structures co-doped with: (a) Sulfur, and (b) Fluorine.

can be seen that compared to other metal ions, crystals co-doped with Yttrium generate slightly less heat. Also, most of the Sulfur co-doped structures generate marginally less than Fluorine co-doped structures. Thus, the multi-scale modeling results show that co-doping with metals such as Yttrium will improve

Table 4.12: Peak heat generation ranges for Sulfur and Fluorine co-doped structures

	Peak heat generation (pW)	
Undoped	73.1	-
Doped element	Sulfur co-doped	Fluorine co-doped
Al	73.4	74.8
Ni	71.7	73.1
Mg	76.3	77.8
Ga	74.8	76.3
Cr	76.3	77.8
Y	59.8	61.0

the material's structural strength while keeping electrochemical properties unchanged. Additionally, co-doping with these metals helps in marginally reducing the chances of a thermal runway.

4.8 Summary and Conclusions

To address the issue of fast degradation of the $Li_xMn_2O_4$ (LMO) spinel cathode material and improve its performance, in this this research, we used multi-scale computational investigation coupled with neurocomputing techniques to explore several cations and anions to replace ~5% and 10% of the Mn^{3+} ions and ~1% of O^{2-} ions, respectively, in the LMO crystal. Cations or metal ions investigated in this research are Al, Ni, Mg, Ga, Cr, and Y, and anions were Sulfur and Fluorine.

Since performing QM simulations on all possible crystal configurations of the doped and co-doped structures is not computationally feasible, QM was mainly used to validate the crystal structure obtained from the MD simulations that were used to undertake co-doping investigations. Specifically, in establishing MD simulations as a feasible tool to undertake doping investigations, crystal lattice length obtained from the MD simulations were compared with the QM results, and we found them to be within ~1% of each other.

In investigating co-doped structures, MD simulations were performed to study the material properties such as Young's modulus, diffusion coefficient of lithium ions, and ionic interactions. To identify the optimal potential crystal configurations that will have the least potential energy, we used a combination of MD simulations and NN techniques. The need for NN techniques is due to the fact that with the addition of dopants, the number of potential configurations increases exponentially, and making an exhaustive MD evaluation of each possible crystal structure computationally infeasible. To overcome this, four

NN models were developed for the intermediate SOCs between 0.5 and 0.875, using a database of MD simulation results on a subset of possible configurations. The NN models were used to select the configurations with the least potential energy for MD simulations, and provided the initial lattice structure values for these simulations. With these NN models, the computational time to evaluate all possible crystal configurations was reduced by nearly 88%. Effect of co-doping on material properties were then investigated on these optimal crystals using MD simulations.

In the MD simulations, output parameters such as variation in the lattice constant, stress and strain generation, and the mobility of Li^+ ions within the cathode structure were studied in detail. Numerical simulation results on the lattice constant values from the MD simulations were validated with the experimental data from the literature as well as QM results. Additionally, diffusion coefficient at different temperatures were also in the good agreement with experimental results from literature for pristine LMO spinel.

A major issue with high energy density cathode materials is thermal runaway which is mainly caused by the heat generation due to intercalation induced stress. Therefore, to verify the improved performance predicted by the MD simulations, CFD simulations using a SPM model were undertaken to understand the impact of co-doping on internal stress and heat generation. The SPM model was equipped with input properties generated from the QM and MD simulations. CFD results suggest that engineered structure using co-doped strategy can help in minimizing the peak lithium ion intercalation induced stress and unwanted heat generation.

The main conclusions from this investigation are as follows:

1. Molecular dynamics is an excellent tool to investigate new and novel cathode materials, and can be ably supported using quantum mechanics simulations.

2. Combining neural computing techniques with MD and QM simulations, we can develop a computationally feasible and efficient tool that can be used to evaluate millions of cathode materials in a short time.

3. Finally, macroscopic properties on potentially feasible material could be easily investigated using CFD simulations to understand the macroscale behaviour of the material.

4. From the specific investigation undertaken in this study we conclude that with trace doping or co-doping, relative volume expansion of LMO spinel can be reduced anywhere between 1-20%. The corresponding stress and strain study show that the yield strength for the co-doped stress might not change much for fully discharged state. However, structures co-doped with Y and Cr tend to outperform LMO spinel.

5. CFD simulation results suggest that replacing mere ∼5% of the Mn^{3+} ions with metal ions such as Al, Mg, Ni, Ga, Cr or Y, and ∼1% of the O^{2-} either by S^{2-} or F^{-}, life of the batteries using LMO spinel as a cathode material can be enhanced by ∼600-7200 charge and discharge cycles without compromising on the energy storage capacity. For most of the selected elements, the maximum stress is below that of the LMO spinel. Yttrium

doped structures, co-doped with either Sulfur or Fluorine, generate less heat during discharge process.

References

[1] A. Manthiram. "Materials Challenges and Opportunities of Lithium Ion Batteries". In: *J. Phys. Chem. Lett.* 2,3.176-184 (2011).

[2] Y. Yang et al. "Graphene nanoribbon/V2O5 cathodes in lithium-ion batteries". In: *ACS Appl. Mater. Interfaces* 6 (2014), pp. 9590–9594.

[3] Y. Yang et al. "Investigations of lithium manganese oxide materials for lithium-ion batteries". In: *J. Power Sources* 65 (1997), pp. 227–230.

[4] J. Shu et al. "A new look at lithium cobalt oxide in a broad voltage range for lithium-ion batteries". In: *J. Phys. Chem. C* 114 (2010), pp. 3323–3328.

[5] L. H. Hu et al. "Graphene-modified LiFePO4 cathode for lithium ion battery beyond theoretical capacity". In: *Nat. Commun.* 4 (2013), p. 1687.

[6] K. C. Kam and M. M. Doeff. In: *Material Matters* 7.4 (2012), pp. 55–82.

[7] Y. Kim. "Lithium nickel cobalt manganese oxide synthesized using alkali chloride flux: Morphology and performance as a cathode material for lithium ion batteries". In: *ACS Appl. Mater. Interfaces* 4 (2012), pp. 2329–2333.

[8] B. V. Merinov et al. "Li-diffusion at the interface between Li-metal and [Pyr14][TFSI]-ionic liquid: Ab initio molecular dynamics simulations". In: *J. Chem. Phys.* 152 031101 (2020).

[9] M. N. Ates, S. Mukerjee, and K. M. Abraham. In: *RSC Adv.* 5 (2015), pp. 27375–27386.

[10] H. -J. Noh et al. In: *J. Power Sources* 233 (2013), pp. 121–130.

[11] X. Hui, L. Zhentao, and Jianping X. "Nanostructured LiMn2O4 and their composites as high-performance cathodes for lithium-ion batteries". In: *Progress in Natural Science: Materials International* 22.572-584 (2012).

[12] E. Iguchi et al. "Electrical transport properties in LiMn2O4, Li0.95Mn2O4, and LiMn1.95B0.05O4 (B=Al or Ga) around room temperature". In: *Journal of Applied Physics* 91.2149 (2002).

[13] S. Y. Luchkin et al. "Li transport in fresh and aged LiMn2O4 cathodes via electrochemical strain microscopy". In: *Journal of Applied Physics* 118.072016 (2015).

[14] R. Sharma, N. Sharma, and M. Sharma. "LiMn2O4 spinel structure as cathode material for Li-ion batteries". In: *AIP Conference Proceedings* 2142.040024 (2019).

[15] H. Y. Amanieu et al. "Mechanical properties of commercial LixMn2O4 cathode under different State of Charge". In: *Acta Materialia* 89 (2015), pp. 153–162.

[16] J.M. Tarascon and M. Armand. "Issues and challenges facing rechargeable lithium batteries". In: *Nature* (2001).

[17] J. Cabana et al. "Enhanced high rate performance of LiMn2O4 spinel nanoparticles synthesized by a hard-template route". In: *J. Power Sources* (2007).

[18] Y. Xia, Y. Zhou, and M. Yoshio. In: *J. Electrochemical Society* 144.8 (1997), p. 2593.

[19] G. G. Amatucci et al. In: *J. Power Sources* 81-82 (1999), pp. 39–43.

[20] C. Julien et al. *Lithium Batteries: Science and Technology*. Springer International Publishing, 2016.

[21] J.and Thomas K.E. Newman, H. Hafezi, and Wheeler D.R. "Modelling of Lithium-ion batteries". In: *J. Power Sources* 119 (2003), pp. 838–843.

[22] J. Christensen and J. Newman. "A Mathematical Model of Stress Generation and Fracture in Lithium Manganese Oxide". In: *J. Electrochem. Soc.* 153 (2006), A1019.

[23] W. H. Woodford, Y.-M. Chiang, and W. C. Carter. ""Electrochemical Shock" of Intercalation Electrodes: A Fracture Mechanics Analysis". In: *J. Electrochem. Soc.* (2010), A1052.

[24] Y. Hu, X. Zhao, and Z. Suo. ""Averting cracks caused by Insertion reaction In lithium-ion batteries". In: *J. Mater. Res., 2010* (2010).

[25] X. Zhang, W. Shyy, and A. M. Sastry. "Numerical Simulation of Intercalation-Induced Stress in Li-Ion Battery Electrode Particles". In: *J. Electrochem. Soc.* 154 (2007), A910.

[26] X. Zhang, A. M. Sastry, and W. Shyy. "Intercalation-Induced Stress and Heat Generation within Single Lithium-Ion Battery Cathode Particles". In: *J. Electrochem. Soc.* 155 (2008), A542.

[27] J. Christensen. "Modeling Diffusion-Induced Stress in Li-Ion Cells with Porous Electrodes". In: *J. Electrochem. Soc.* 157 (2010), A366.

[28] Y. Tesfamhret et al. "On the Manganese Dissolution Process from LiMn2O4 Cathode Materials". In: *ChemElectroChem* 8.8 (2021), pp. 1516–1523.

[29] S. W. Lee et al. In: *J. Power Sources* 126 (2004), p. 150.

[30] D. Arumugam and G. P. Kalaignan. In: *J. Electroanal. Chem.* 624 (2008), p. 197.

[31] K. Y. Chung, C. -W. Ryu, and K. -B. Kim. In: *J. Electrochem. Soc.* 152.4 (2005), A791.

[32] C. Sigala et al. In: *Solid State Ionics* 81 (1995), p. 167.

[33] P. Arora, B. N. Popov, and R. E. White. In: *J. Electrchem. Soc.* 145 (1998), p. 807.

[34] P. Angelopoulou et al. "Enhanced Performance of LiAl0.1Mn1.9O4 Cathode for Li-Ion Battery via TiN Coating". In: *Energies* 14.4 (2021), p. 825.

[35] Z. Yang et al. "Mg2+ and Ti4+ Co–Doped Spinel LiMn2O4 as Lithium-Ion Battery Cathode". In: *Chemistry SELECT* 4.33 (2019), pp. 9583–9589.

[36] Y. Deng et al. "Enhanced Electrochemical Performance in Ni-Doped LiMn2O4-Based Composite Cathodes for Lithium-Ion Batteries". In: *ChemElectroChem* 4.6 (2017), pp. 1362–1371.

[37] M. Michalska et al. "Improved electrochemical performance of LiMn2O4 cathode material by Ce doping". In: *Electrochimica Acta* 276 (2018), pp. 37–46.

[38] R. Thirunakaran et al. "Cerium and zinc: Dual-doped LiMn2O4 spinels as cathode material for use in lithium rechargeable batteries". In: *Journal of Power Sources* 187.2 (2009), pp. 565–574.

[39] D. Zhang, B.N. Popov, and R.E. White. "Electrochemical investigation of CrO2.65 doped LiMn2O4 as a cathode material for lithium-ion batteries". In: *Journal of Power Sources* 76.1 (2009), pp. 81–90.

[40] D.-L. Fang et al. "Synthesis of a Co–Ni doped LiMn2O4 spinel cathode material for high-power Li-ion batteries by a sol–gel mediated solid-state route". In: *Journal of Alloys and Compounds* 640 (2015), pp. 82–89.

[41] M. Nishijima et al. "Accelerated discovery of cathode materials with prolonged cycle life for lithium-ion battery". In: *Nature Communications* 5 (2014), p. 4553.

[42] G. G. Amatucci et al. In: *Solid State Ionics* 104.1-2 (1997), pp. 13–25.

[43] J. Park, W. Lu, and A. M. Sastry. "Numerical Simulation of Stress Evolution in Lithium Manganese Dioxide Particles due to coupled Phase Transition and Intercalation". In: *J. Electrochem. Soc.* 158.2 (2011), A201–A206.

[44] R. Tyagi and S. Srinivasan. "Molecular Dynamics modelling of lithium ion intercalation induced change in the mechanical properties of LixMn2O4". In: *J. Chem. Phys.* 153 (2020), p. 164712.

[45] R. Tyagi, A. Lanjan, and S. Srinivasan. "Co-doping strategies to improve the Electrochemical properties of LixMn2O4 cathodes for Li-ion Batteries". In: *ChemElectroChem* 24.9 (2021), pp. 101–125. DOI: https://doi.org/10.1002/celc.202101626.

[46] L. Zhang et al. "Sphere-Shaped Hierarchical Cathode with Enhanced Growth of Nanocrystal Planes for High-Rate and Cycling-Stable Li-Ion Batteries". In: *Nano Lett.* 15.1 (2015), pp. 656–661.

[47] Y. Z. Zheng et al. "Nickel-mediated polyol synthesis of hierarchical V2O5 hollow microspheres with enhanced lithium storage properties". In: *J. Mater. Chem. A* 3 (2015), pp. 1979–1985.

[48] M. Zhi et al. "Nanostructured carbon–metal oxide composite electrodes for supercapacitors: a review". In: *Nanoscale* 5 (2013), pp. 72–88.

[49] Z. Moradi, A. Lanjan, and S. Srinivasan. "Enhancement of Electrochemical Properties of Lithium Rich Li2RuO3 Cathode Material". In: *J Electrochemical Society* 167.11 (2020), p. 110537.

[50] Z. Moradi, A. Lanjan, and S. Srinivasan. "Multi-Scale Investigation into Co-Doping Strategy on The Electrochemical Properties of Li2RuO3 Cathode for Li-Ion Batteries". In: *ChemElectroChem* 8.1 (2021), pp. 112–124.

[51] L. Xiao et al. "Enhanced electrochemical stability of Al-doped LiMn2O4 synthesized by a polymer-pyrolysis method". In: *Electrochimica Acta* 54.2 (2008), pp. 545–550.

[52] H. Zhang et al. "Structure and Performance of Dual-doped LiMn2O4 Cathode Materials Prepared via Microwave Synthesis Method". In: *Electrochimica Acta* 125 (2014), pp. 225–231.

[53] M. Swietoslawski, M. Bakierska, and M. Molenda. In: *ECS Meet. Abstr.* MA2016-03 (2016), p. 582.

[54] M. Kubicka et al. "The Temperature Effect on the Electrochemical Performance of Sulfur-Doped LiMn2O4 in Li-Ion Cells". In: *Nanomaterials* 9 (2019), p. 1722.

[55] F. Qian et al. In: *Material & Design* 194 (2020), p. 108867.

[56] M. Molenda et al. "Synthesis and characterisation of sulphided lithium manganese spinels LiMn2O4-ySy prepared by sol-gel method". In: *Solid State Ionics* 176 (2005), pp. 1702–1709.

[57] M. Bakierska, M. Molenda, and R. Dziembaj. "Optimization of sulphur content in LiMn2O4-ySy spinels as cathode materials for lithium-ion batteries". In: *Procedia Eng* 98 (2014), pp. 20–27.

[58] M. Nakayama, M. Kanekoa, and M. Wakiharaa. "First-principles study of lithium ion migration in lithium transition metal oxides with spinel structure". In: *Phys. Chem. Chem. Phys.* 14 (2012), pp. 13963–13970.

[59] K. Okhotnikov, B. Stevensson, and M. Eden. "New interatomic potential parameters for molecular dynamics simulations of rare-earth (RE = La, Y, Lu, Sc) aluminosilicate glass structures: exploration of RE3+ field-strength effects". In: *Phys. Chem. Chem. Phys.* 15 (2013), pp. 15041–15055.

[60] P. Shukla et al. "Effect of inversion on thermoelastic and thermal transport properties of MgAl2O4 spinel by atomistic simulation". In: *J Mater Sci* 46 (2011), pp. 55–62.

[61] P. D. Battle, T. S. Bush, and C. A. Catlow. "Structures of Quaternary Ru and Sb Oxides by Computer Simulation". In: *J. Am. Chem. Soc.* 117.23 (1995), pp. 6292–6296.

[62] K. Wright and J. D. D. Gale. "Interatomic potentials for the simulation of the zinc-blende and wurtzite forms of ZnS and CdS: Bulk structure, properties, and phase stability". In: *Phys. Rev. B* 70 (2004), p. 035211.

[63] X. Xueli Wang et al. "Thermodynamic of intrinsic defects in β-Ga2O3". In: *Journal of Physics and Chemistry of Solids* 132 (2019), pp. 104–109. DOI: https://doi.org/10.1016/j.jpcs.2019.04.014.

[64] R.T. Cygan, H.R. Westrich, and D.H. Doughty. "Ionic modeling of lithium manganese spinel materials for use in rechargeable batteries". In: *Mater. Res. Soc. Proc* 393 (1995), p. 113.

[65] G. V. Lewis and C. R. A. Catlow. "Potential models for ionic oxides". In: *J. Phys. C: Solid State Phys* 18 (1985), p. 1149.

[66] P. P. Ewald. "The calculation of optical and electrostatic grid potential". In: *Ann. Phys. (Leipzig)* 64.253 (1921).

[67] S. Nose. "A unified formulation of the constant temperature molecular dynamics methods". In: *J. Chem. Phys.* 81 (1984), pp. 511–519.

[68] S. Sandhu et al. "Using neurocomputing techniques to determine microstructural properties in a Li-ion battery". In: *Neural Computing and Applications* 34 (2022), pp. 9983–9999. DOI: https://doi.org/10.1007/s00521-022-06985-0.

[69] T. Szandala. "Review and Comparison of Commonly Used Activation Functions for Deep Neural Networks". In: *Bio-inspired Neurocomputing. Studies in Computational Intelligence* 903 (2021), pp. 203–224. DOI: https://doi.org/10.1007/978-981-15-5495-7_11.

[70] C. Bircanoğlu and N. Arıca. "A comparison of activation functions in artificial neural networks". In: *2018 26th Signal Processing and Communications Applications Conf. (SIU)*. 2018, pp. 1–4.

[71] G. E. Dahl, T. N. Sainath, and G. E. Hinton. "Improving deep neural networks for LVCSR using rectified linear units and dropout". In: *IEEE Int. Conference on Acoustics, Speech and Signal Processing*. 2013, pp. 8609–8613.

[72] D. Kingma and J. Ba. "Adam: A Method for Stochastic Optimization". In: *International Conference on Learning Representations* (Dec. 2014).

[73] X. Glorot and Y. Bengio. "Understanding the difficulty of training deep feedforward neural networks". In: *Proc. of the Thirteenth Int. Conference on Artificial Intelligence and Statistics*. Vol. 9. Proc. of Machine Learning Res. Chia Laguna Resort, Sardinia, Italy: PMLR, May 2010, pp. 249–256.

[74] C.-L. Cheng, Shalabh, and G. Garg. "Coefficient of determination for multiple measurement error models". In: *J. of Multivariate Analysis* 126 (2014), pp. 137–152.

[75] P. Giannozzi et al. "QUANTUM ESPRESSO: a modular and open-source software project for quantum simulations of materials". In: *J. Phys.: Condens. Matter* 21.39 (2009), p. 5502.

[76] D. Vanderbilt. "Soft self-consistent pseudopotentials in a generalized eigenvalue formalism". In: *Phys. Rev. B* 41 (1990), p. 7892.

[77] A. D. Corso. "Pseudopotentials periodic table: From H to Pu". In: *Computational Materials Science* 95 (2014), pp. 337–350.

[78] R.O. Jones and O. Gunnarsson. "The density functional formalism, its applications and prospects". In: *Reviews of Modern Physics* 61.3 (1989), pp. 689–746.

[79] J. P. Perdew, K. Burke, and M. Ernzerhof. "Generalized Gradient Approximation Made Simple". In: *Phys. Rev. Lett.* 78 (1997), p. 1396.

[80] I. V. Tetko, D. J. Livingstone, and A. I. Luik. "Neural network studies. 1. Comparison of overfitting and overtraining". In: *Adv. Neural Inform*

Process Syst. 35 (Sept. 1995), pp. 826–833. DOI: https://doi.org/10.1021/ci00027a006.

[81] O Bousquet and A. Elisseeff. "Stability and Generalization". In: *J. of Machine Learning Res.* 2 (June 2002), pp. 499–526.

[82] N. Ishizawa et al. "Structural disorder along the lithium diffusion pathway in cubically stabilized lithium manganese spinel: I. Synchrotron X-ray studies". In: *Journal of Solid State Chemistry* 174.1 (2003), pp. 167–174.

[83] Y.Y. Xia and M. Yoshio. "An investigation of lithium ion insertion into spinel structure Li-Mn-O compounds". In: *Journal of The Electrochemical Society* 143.3 (1996), pp. 825–833.

[84] S. Takai et al. "Tracer diffusion coefficients of lithium ion in LiMn2O4 measured by neutron radiography". In: *Solid State Ionics* 256 (2014), p. 93.

[85] N. Kuwata et al. "Lithium diffusion coefficient in LiMn2O4 thin films measured by secondary ion mass spectrometry with ion-exchange method". In: *Solid State Ionics* 320 (2018), pp. 266–271.

[86] J. H. Lee et al. "Degradation mechanisms in doped spinels of LiM0.05Mn1.95O4 (M=Li, B, Al, Co, and Ni) for Li secondary batteries". In: *Journal of Power Sources* 89.1 (2000), pp. 7–14.

[87] A. Llusco, M. Grageda, and S. Ushak. "Kinetic and Thermodynamic Studies on Synthesis of Mg-Doped LiMn2O4 Nanoparticles". In: *nanomaterials* 10.7 (2020), p. 1409.

[88] Y. Yu et al. "Enhancing the durable performance of LiMn2O4 at high-rate and elevated temperature by nickelmagnesium dual doping". In: *Nature* 9 (2019), p. 16864.

[89] E. V. Vakarin, G. G. Belmonte, and J. P. Badiali. "Interplay of host volume variations and internal distortions in the course of intercalation into disordered matrices". In: *J. Chem. Phys.* 126.234709 (2007).

[90] S. Lee et al. "Molecular Dynamics Simulations of SOC-Dependent Elasticity of LixMn2O4 Spinels in Li-Ion Batteries". In: *J. Electrochem. Soc.* 160.6 (2013), A968–A972.

[91] A. Asadi, S. Aghamiri, and M. Talaie. "Molecular dynamics simulation of a LixMn2O4 spinel cathode material in Li-ion batteries". In: *RSC Advances* (2016).

[92] M.D. Chung et al. "Implementing Realistic Geometry and Measured Diffusion Coefficients into Single Particle Electrode Modeling Based on Experiments with Single LiMn2O4 Spinel Particles". In: *J. Electrochem. Soc.* 158.4 (2011).

Chapter 5

Conclusions and Future Work

The main objective of this dissertation was to address the issue of the quick degradation of $Li_xMn_2O_4$ (LMO) spinel as a cathode material and develop a molecular dynamics model to improve its performance. This was accomplished in three stages:

Stage 1: Development and Validation of the Computational Tools:
This research began with the preparation of the MD simulation setups for different charge/discharge (strain) rates at various SOC values. In order to setup MD simulations, a unique approach of calculating the potential energy of all possible configurations and picking four lowest potential energy cases after running it for 1 time step, was employed. On these four cases, system equilibration and production simulations were performed. This strategy saved a lot of computational time and ensured that the approach is computationally feasible to investigate numerous possible crystal configurations.

The results obtained from MD simulations were in very good agreement with the experimental values available from literature. One of the major conclusions from these MD simulations at various SOCs was that LMO spinel material behaves differently at different SOC values and is governed by the material strength and/or the diffusivity of the lithium-ions within the material. For example, diffusion coefficient for the lower SOC values were much higher compared to the case wherein most of the lithium-ions are already intercalated in a higher SOC. On the other hand, structural strength for partial charged states were found to be lower as lithium vacant sites seems to effect the structural integrity. The MD simulation results also helped capture the vacancy diffusion mechanism well, where activation energy for an ion to move can be divided into two parts, vacancy formation and migration energy.

Stage 2: Designing Novel Materials Using Doping and Co-doping Strategies: In order to design novel cathode material using non-toxic, less expensive and environmental friendly elements, trace doping and co-doping of LMO spinel could be used. Therefore, potential doping elements those can replace Mn^{3+} partially, without changing overall structure too much, were explored. Specific dopants considered were Al, Ni, Mg, Ga, Cr and Y. Initially 5% of the Mn^{3+} ions were replaced by each dopant. To study the effect of doping, parameters like lattice expansion, stress-strain curve for fully and partially charged states, and diffusivity of the lithium ions at various temperature and SOC values were compared. The conclusions from the investigations were:

1. Dopants with smaller ionic radius such as Al and Mg tend to reduce the overall lattice dimensions, marginally elevating the stress in the material and negatively impacting the diffusion of Lithium-ions.

2. However, this can be addressed by co-doping in which approximately 1% of O^{2-} is replaced by S^{2-} which has comparatively larger ionic radius. Another co-dopant that is useful in this approach is Fluorine that has a higher electronegativity.

3. High amount of dopants is not beneficial because this results in a rapid decline in the overall discharge capacity of the cathode material.

In the absence of experimental data to validate the performance of these newly engineered cathode materials, QM simulations were performed for the

final structure. It was found that the results from MD and QM simulations were in good agreement with each other.

Furthermore, to study the material behaviour at macro scale, several Computational Fluid Dynamics (CFD) simulations, which uses the material properties such as Young's modulus and diffusion coefficient obtained from the MD simulations, were performed. For CFD simulations, the Single Particle Model (SPM) based algorithm was used. Main objective behind running CFD simulations was to study the intercalation induced stress and heat generation at macro scale. It was established that the new cathode materials with dopants experienced lower stresses and heat generation, and demonstrate an improved life cycle, reaffirming the applicability of these materials as the next generation cathode materials.

Stage 3: Adoption of Machine Learning Techniques to Propose an Enhanced Computational Tool:

It must be noted that with co-doping strategies, there are innumerable crystal configurations that need to be evaluated to determine the optimal configuration with the least potential energy. Thus, even a 1-timestep simulation to evaluate all combinations and identify the most feasible configuration becomes computationally impossible. To overcome this, principles of Artificial Neural Networks was employed to rapidly evaluate the combinations to determine the optimal configurations that are likely to have the least potential energy.

A total four NN models were developed for the intermediate SOCs between

0.5 and 0.875, using a database of MD simulation results on a subset of possible configurations. With these NN models, the computational time to evaluate all possible crystal configurations was reduced by nearly 88%. Effect of co-doping on material properties were then investigated on these optimal crystals using MD simulations.

QM simulations were used to validate the crystal structure obtained from the MD simulations of co-doped crystal structures. Specifically, in establishing MD simulations as a feasible tool to undertake doping investigations, crystal lattice length obtained from the MD simulations were compared with the QM results, and we found them to be within ~1% of each other.

The main conclusions/outcomes from this research are:

1. Establishment of a Molecular dynamics framework to get accurate input properties for macro scale models. Further, it also allows to investigate new and novel cathode materials.

2. Enhancement of the framework with a combination of QM and MD simulations to advance the research on novel multi-dopant electrode materials for which experimental data is not available.

3. Combination of the ANN with with MD and QM simulations makes the investigation of multi-dopant cathode materials computationally feasible.

4. Finally, macro scale simulations can be performed on the convincing materials before performing experimental tests.

5. In demonstrating the multi-scale computational framework developed in this research, it was found that with trace amounts of cations and anions in the LMO spinel as dopants, the relative volume expansion can be reduced anywhere between 1-20%. The corresponding stress and strain study show that the yield strength for the co-doped stress might not change much for fully discharged state. However, structures co-doped with Y and Cr tend to outperform LMO spinel.

6. CFD simulation results suggest that by replacing ~5% of the Mn^{3+} ions with metal ions such as Al, Mg, Ni, Ga, Cr or Y, and ~1% of the O^{2-} with either S^{2-} or F^{-}, life of the batteries using LMO spinel as a cathode material can be enhanced by ~600-7200 charge and discharge cycles without compromising the energy storage capacity. For most of the selected elements, the maximum stress is below that of the LMO spinel. Yttrium doped structures, co-doped with either Sulfur or Fluorine, generate less heat during discharge process.

Future work:

1. The objective of this research was limited to improving the material properties of LMO spinel while using non-toxic, less expensive and environmental friendly elements. However, modeling techniques explored in this research can be used to research other doping strategies with other cathode materials. For example, it will also be interesting to study how co-doping with S and Y effect other commercial cathode materials especially $LiFePO_4$.

2. The computational framework developed in this thesis can be used to study anode, electrolyte or other materials used in the lithium-ion batteries.

3. Future work can also be focused on performing the experiments for recommended engineered structures, especially on LMO-SY which shows very promising material properties.

References

[1] T Nguyen and R Savinell. "Flow Batteries in: The Electrochimal Society Interface". In: *Electrochem. Soc. Interface* (2010), 54–56, New Jersey, USA.

[2] D. R. Rolison et al. "Multifunctional 3D nanoarchitectures for energy storage and conversion". In: *Chem. Soc. Rev.* 38 (2009), pp. 226–252.

[3] M. K. Shobana. "Metal oxide coated cathode materials for Li ion batteries – A review". In: *Journal of Alloys and Compounds* 802 (2019), pp. 477–487.

[4] K. Mizushima et al. "Lixcoo2 (0<x≤1): a New Cathode Material for Batteries of High-Energy Density". In: *Materials Research Bulletin* 15.6 (1980), pp. 783–789.

[5] T. Ohzuku et al. "Comparative study of $LiCOO_2$, $LiNi_{0}.5CO_{0}.5O_2$ and $LiNiO_2$ for 4-volt secondary Lithium cells". In: *Electrochimica Acta* 38.9 (1993), pp. 1159–1167.

[6] Y.Y. Xia and M. Yoshio. "An investigation of lithium ion insertion into spinel structure Li-Mn-O compounds". In: *Journal of The Electrochemical Society* 143.3 (1996), pp. 825–833.

[7] G. Ceder et al. "Identification of cathode materials for lithium batteries guided by first-principles calculations". In: *Nature* 392.6677 (1998), pp. 694–696.

[8] J.M. Tarascon and M. Armand. "Issues and challenges facing rechargeable lithium batteries". In: *Nature* (2001).

[9] F. Croce et al. "A novel concept for the synthesis of an improved LiFePO4 lithium battery cathode". In: *Electrochemical and Solid State Letters* 5.5 (2002), A47–A50.

[10] F. Croce et al. "Lithium batteries and cathode materials". In: *Chemical Reviews* 104.10 (2004), pp. 4271–4301.

[11] M.M. Thackeray et al. "Lithium insertion into manganese spinels". In: *Mater. Res. Bull.* (1983).

[12] J.B Goodenough et al. "Lithium Insertion Extraction Reactions with Manganese Oxides". In: *Revue de Chimie Minerale* 21.4 (1984), pp. 435–455.

[13] W.I.F. David et al. "Lithium Insertion into Beta-Mno2 and the Rutile-Spinel Transformation". In: *Revue de Chimie Minerale* 19.1 (1984), pp. 99–106.

[14] R.J. Gummow, A. Dekock, and M.M. Thackeray. "IMPROVED CAPACITY RETENTION IN RECHARGEABLE 4V LITHIUM LITHIUM MANGANESE OXIDE (SPINEL) CELLS". In: *Solid State Ionics* 69.1 (1994), pp. 59–67.

[15] K.S. Lee et al. "Co-precipitation synthesis of spherical $Li_1.05M_0.05Mn_1.9O_4$ (M = Ni, Mg, Al) spinel and its application for lithium secondary battery cathode". In: *Electrochimica Acta* 52.16 (2007), pp. 5201–5206.

[16] L. Hernan et al. "Use of Li-M-Mn-O [M = Co, Cr, Ti] spinels prepared by a sol-gel method as cathodes in high-voltage lithium batteries". In: *Solid State Ionics* 118.3-4 (1999), pp. 179–185.

[17] G.H. Li et al. "The spinel phases $LiM_yMn_2 - yO_4$ (M=Co,Cr,Ni) as the cathode for rechargeable lithium batteries". In: *Journal of The Electrochemical Society* 143.1 (1996), pp. 178–182.

[18] T. Ohzuku, S. Takeda, and M. Iwanaga. "Solid-state redox potentials for $Li[Me_0.5Mn_1.5]O_4$ (Me: 3d-transition metal) having spinel-framework structures: a series of 5 volt materials for advanced lithium-ion batteries". In: *Journal of Power Sources* 81-82 (1999), pp. 90–94.

[19] R. Singhal et al. "Synthesis and characterization of Nd doped LiMn2O4 cathode for Li-ion rechargeable batteries". In: *Journal of Power Sources* 164.2 (2007), pp. 857–861.

[20] J. Tu et al. "Studies of cycleability of LiMn2O4 and $LiLa_0.01Mn_1.99O_4$ as cathode materials for Li-ion battery". In: *Physica B-Condensed Matter* 382.1-2 (2006), pp. 129–134.

[21] J.and Thomas K.E. Newman, H. Hafezi, and Wheeler D.R. "Modelling of Lithium-ion batteries". In: *J. Power Sources* 119 (2003), pp. 838–843.

[22] D. Aurbach et al. "Design of electrolyte solutions for Li and Li-ion batteries: a review". In: *Electrochim. Acta* 50 (2004), p. 247.

[23] S. S. Zhang. "A review on electrolyte additives for lithium-ion batteries". In: *J. Power Sources* 162 (2006), p. 1379.

[24] P. Arora, R. E. White, and M. Doyle. "Capacity Fade Mechanisms and Side Reactions in Lithium-Ion Batteries". In: *J. Electrochem. Soc.* 145 (1998), pp. 3647–3667.

[25] J. Christensen and J. Newman. "A Mathematical Model of Stress Generation and Fracture in Lithium Manganese Oxide". In: *J. Electrochem. Soc.* 153 (2006), A1019.

[26] X. Zhang, W. Shyy, and A. M. Sastry. "Numerical Simulation of Intercalation-Induced Stress in Li-Ion Battery Electrode Particles". In: *J. Electrochem. Soc.* 154 (2007), A910.

[27] X. Zhang, A. M. Sastry, and W. Shyy. "Intercalation-Induced Stress and Heat Generation within Single Lithium-Ion Battery Cathode Particles". In: *J. Electrochem. Soc.* 155 (2008), A542.

[28] W. H. Woodford, Y.-M. Chiang, and W. C. Carter. ""Electrochemical Shock" of Intercalation Electrodes: A Fracture Mechanics Analysis". In: *J. Electrochem. Soc.* (2010), A1052.

[29] J. Christensen. "Modeling Diffusion-Induced Stress in Li-Ion Cells with Porous Electrodes". In: *J. Electrochem. Soc.* 157 (2010), A366.

[30] M. T. Lawder et al. "Battery Energy Storage System (BESS) and Battery Management System (BMS) for Grid-Scale Applications". In: *Proceedings of the IEEE* 102.6 (2014), pp. 1014–1030.

[31] D. Zhang, B.N. Popov, and R.E. White. "Modeling Lithium Intercalation of a Single Spinel Particle under Potentiodynamic Control". In: *J. Electrochem. Soc.* 147 (2000), pp. 831–838.

[32] M. Doyle and J. Newman. "The use of mathematical modeling in the design of lithium/polymer battery systems". In: *Electrochim. Acta* 40 (1995), pp. 2191–2196.

[33] M. Doyle and J. Newman. "Modeling the performance of rechargeable lithium-based cells: design correlations for limiting cases". In: *J. Power Sources* 54 (1995), pp. 46–51.

[34] J. Newman. "Optimization of Porosity and Thickness of a Battery Electrode by Means of a Reaction-Zone Model". In: *J. Electrochem. Soc.* 142 (1995), pp. 97–101.

[35] V. Ramadesigan et al. "Optimal Porosity Distribution for Minimized Ohmic Drop across a Porous Electrode". In: *J. Electrochem. Soc.* 157 (2010), A1328–A1334.

[36] M. Doyle, T.F. Fuller, and J. Newman. "Modeling of Galvanostatic Charge and Discharge of the Lithium/Polymer/Insertion Cell". In: *J. Electrochem. Soc.* 140 (1993), A1526–1533.

[37] S. Al Hallaj et al. "Thermal modeling and design considerations of lithium-ion batteries". In: *J. Power Sources* 83 (1999), pp. 1–8.

[38] D. Bernardi, E. Pawlikowski, and J. Newman. "A General Energy Balance for Battery Systems". In: *J. Electrochem. Soc.* 132 (1985), pp. 5–12.

[39] Y. Chen and J.W. Evans. "Heat Transfer Phenomen in Lithium/Polymer-Electrolyte Batteries for Electric Vehicle Application". In: *J. Electrochem. Soc.* 140 (1993), pp. 1833–1838.

[40] Y. Chen and J.W. Evans. "Three-Dimensional Thermal Modeling of Lithium-Polymer Batteries under Galvanostatic Discharge and Dynamic Power Profile". In: *J. Electrochem. Soc.* 141 (1994), pp. 2947–2955.

[41] T.I. Evans and R.E. White. "A Thermal Analysis of a Spirally Wound Battery Using a Simple Mathematical Model". In: *J. Electrochem. Soc.* 136 (1989), pp. 2145–2152.

[42] W.B. Gu et al. "Thermal-electrochemical coupled modeling of a lithium-ion cell". In: *The Electrochemical Society Proceedings Series, Pennington, NJ* (2000), p. 748.

[43] V. Srinivasan and C.Y. Wang. "Analysis of Electrochemical and Thermal Behavior of Li-Ion Cells". In: *J. Electrochem. Soc.* 150 (2003), A98–A106.

[44] J. Newman and W. Tiedemann. "Temperature Rise in a Battery Module with Constant Heat Generation". In: *J. Electrochem. Soc.* 142 (1995), pp. 1054–1057.

[45] S. Chen, C. Wan, and Y. Wang. "Thermal analysis of lithium-ion batteries". In: *J. Power Sources* 140 (2005), pp. 111–124.

[46] J. Lee et al. "Three-Dimensional Thermal Modeling of Electric Vehicle Batteries". In: *J. Electrochem. Soc.* 133 (1986), pp. 1286–1291.

[47] G.H. Kim and K. Smith. "Multi-Scale Multi-Dimensional Lithium-Ion Battery Model". In: *ECS Meeting Abstracts* 802 (2008), p. 1295.

[48] J.P. Meyers et al. "The Impedance Response of a Porous Electrode Composed of Intercalation Particles". In: *J. Electrochem. Soc.* 147 (2000), pp. 2930–2940.

[49] D.E. Stephenson et al. "Modeling of Particle-Particle Interactions in Porous Cathodes for Lithium-Ion Batteries". In: *J. Electrochem. Soc.* 154 (2007), A1146–A1155.

[50] T.O. Drews et al. "Coupled Mesoscale Continuum Simulations of Copper Electrodeposition in a Trenchs". In: *AIChE J.* 50 (2004), pp. 226–240.

[51] A. Van der Ven and G. Ceder. "Lithium Diffusion in Layered LixCoO2". In: *Electrochem. Solid St.* 3 (2010), pp. 301–304.

[52] J. Bhattacharya and A. Van der Ven. "Phase stability and nondilute Li diffusion in spinel Li1+xTi2O4". In: *Phys. Rev. B* 81 (2010), p. 104304.

[53] R.N. Methekar et al. "Kinetic Monte Carlo simulation of surface homogeneity in graphite anodes of Lithium-ion batteries: Passive layer formation". In: *J. Electrochem. Soc.* 158 (2011), A363–A370.

[54] K. Leung and J.L. Budzien. "Ab initio molecular dynamics simulations of the initial stages of solid–electrolyte interphase formation on lithium ion battery graphitic anodes". In: *Phys. Chem. Chem. Phys.* 12 (2010), pp. 6583–6586.

[55] W.Q. Li and S.H. Garofalini. "Molecular dynamics simulation of lithium diffusion in Li 2O-Al2O3-SiO2 glasses". In: *Solid State Ionics* 166 (2004), pp. 365–373.

[56] Y. Qi et al. "Threefold increase in the young's modulus of graphite negative electrode during lithium intercalation". In: *J. Electrochem. Soc.* 157 (2010), A558–A566.

[57] Y.-T. Cheng and M. W. Verbrugge. "The influence of surface mechanics on diffusion induced stresses within spherical nanoparticles". In: *J. Appl. Phys.* 104 (2008), p. 083521.

[58] R. Deshpande, Y.-T. Cheng, and M. W. Verbrugge. "Modelling diffusion-induces stress in nanowire electrode structures". In: *J. Power Sources* 195 (2010), p. 5081.

[59] M. W. Verbrugge and Y.-T. Cheng. "Stress and Strain-Energy Distributions within Diffusion-Controlled Insertion-Electrode Particles Subjected to Periodic Potential Excitations". In: *J. Electrochem. Soc.* 156 (2009), A927.

[60] Y.-T. Cheng and M. W. Verbrugge. "Evolution of stress within a spherical insertion electrode particle under potentiostatic and galvanostatic operation". In: *J. Power Sources* 190 (2009), p. 453.

[61] C. Y. Ouyang et al. "Ab initio molecular-dynamics studies on LiMn2O4 as cathode material for lithium secondary batteries". In: *Europhys.,Lett.* 67 (2004), p. 28.

[62] K. Tateishi, D. d. Boulay, and N. Ishizawa. "The effect of mixed Mn valences on Li migration in LiMn2O4 spinel: A molecular dynamics study". In: *Appl. Phys. Lett.* 84 (2004), p. 529.

[63] K. Tateishi et al. "Structural disorder along the lithium diffusion pathway in cubically stabilized lithium manganese spinel II. Molecular dynamics calculation". In: *J. Solid State Chem.* 174 (2003), p. 175.

[64] I. Y. Gotlib, I. V. Murin, and E. M. Piotrovskaya. "Molecular Dynamics Simulations of LixMn2O4 Spinel Solid Solutions with Simple Potential Models". In: *Inorg. Mater.* 39 (2003), p. 404.

[65] S Plimpton. "Fast Parallel Algorithms for Short-Range Molecular Dynamics". In: *J. Comp. Phys.* 117 (1995), p. 1.